

AD-A264 102

IDENTIFICATION PAGE

Form Approved
OMB No. 0704-0188

Estimated to average 1 hour per response, including the time for reviewing instructions, searching existing data sources, gathering the necessary data, reviewing the collection of information, Send comments regarding this burden estimate or any other aspect of this collection of information, including suggestions for reducing this burden, to Washington Headquarters Services, Directorate for Information Operations and Reports, 1215 Jefferson Davis Highway, Suite 1204, Arlington, VA 22202-4302, and to the Office of Management and Budget, Paperwork Reduction Project (0704-0188), Washington, DC 20503

1. AGENCY USE ONLY (Leave blank)		2. REPORT DATE 4-16-93		3. REPORT TYPE AND DATES COVERED Final Nov 88 - 31 Oct 89	
4. TITLE AND SUBTITLE Microwave Emission From Relativistic Electron Beams				5. FUNDING NUMBERS AFOSR 89-0082 C 2301/ES	
6. AUTHOR(S) Prof. George Bekefi				8. PERFORMING ORGANIZATION REPORT NUMBER AFOSR-TR-83-0509	
7. PERFORMING ORGANIZATION NAME(S) AND ADDRESS(ES) Research Laboratory of Electronics Massachusetts Institute of Technology 77 Massachusetts Avenue Cambridge, MA 02139				10. SPONSORING / MONITORING AGENCY REPORT NUMBER 2301/ES	
9. SPONSORING / MONITORING AGENCY NAME(S) AND ADDRESS(ES) A.F. Office of Scientific Research Building 410 Bolling Air Force Base, DC 20332				11. SUPPLEMENTARY NOTES The view, opinions and/or findings contained in this report are those of the author(s) and should not be construed as an official Department of the Army position, policy, or decision, unless so designated by other documentation.	
12a. DISTRIBUTION / AVAILABILITY STATEMENT Approved for public release; distribution unlimited.				12b. DISTRIBUTION CODE DTIC ELECTE MAY 13 1993 S C D	
13. ABSTRACT (Maximum 200 words) Work by Prof. Bekefi and his collaborators is summarized here 93 5 11 044 93-10278					
14. SUBJECT TERMS				15. NUMBER OF PAGES	
				16. PRICE CODE	
17. SECURITY CLASSIFICATION OF REPORT UNCLASSIFIED		18. SECURITY CLASSIFICATION OF THIS PAGE UNCLASSIFIED		19. SECURITY CLASSIFICATION OF ABSTRACT UNCLASSIFIED	
				20. LIMITATION OF ABSTRACT UL	

FINAL REPORT

United States Air Force Office of Scientific Research

MICROWAVE EMISSION FROM RELATIVISTIC ELECTRON BEAMS

Project Period
November 1, 1988 - December 31, 1992

Research Grant Number: AFOSR-89-0082

Attention: Dr. Robert Barker
AFOSR/NE
110 Duncan Avenue (Bldg 410) Suite B115
Bolling AFB, DC 20332-0001

Submitted by

George Bekefi
Research Laboratory of Electronics
Massachusetts Institute of Technology
77 Massachusetts Avenue
Cambridge, Massachusetts 02139

April 12, 1993

Accession For	
NTIS CRA&I	<input checked="" type="checkbox"/>
DTIC TAB	<input type="checkbox"/>
Unannounced	<input type="checkbox"/>
Justification	
By	
Distribution /	
Availability Codes	
Dist	Avail and/or Special
A-1	

Table of Contents

Research in Project Period November 1, 1988 - October 31, 1989.....	1
Research in Project Period November 1, 1989 - October 31, 1990.....	17
Research in Project Period November 1, 1990 - October 31, 1991.....	89
Research in Project Period November 1, 1991 - December 31, 1992.....	129

PROJECT PERIOD
November 1, 1988 - October 31, 1989

Table of Contents

Short period wiggler for free electron lasers.....	3
Studies of optical guiding and profile modification in a Raman FEL	9
Study of FEL mode competition	9
Effect of electron prebunching on the radiation growth rate in a collective (Raman) free electron laser amplifier.....	13
Experiments with a 35 GHz cyclotron auto resonance maser (CARM).....	13

This is a continuation proposal on Microwave Emission from Relativistic Electron Beams for the grant period of November 1, 1988 to October 31, 1989.

Below we summarize the various research activities supported wholly or in part under the aegis of the Air Force Office of Scientific Research.

All of the experimental studies described below will be performed using our Physics International 615MR Pulserad Accelerator with a maximum voltage of 500 kV and peak currents of 4 kA and the 1.5MV, 30kA Pulserad 110A.

The electron beam is presently generated by a thermionically emitting, electrostatically focused, Pierce-type electron gun (250 kV, 250 A) removed from a SLAC klystron (model 343). An assembly of six focusing coils is designed so that their magnetic field lines lie along the zero-magnetic field electron trajectories (see Fig. 1). This field configuration gives the least scalloping of the electron beam (low transverse temperature) and allows the magnetic field amplitude to be varied over a wide range without greatly affecting the electron beam temperature. Only the inner portion of the beam is used; an aperture limits the beam radius to $r_b = 0.254$ cm. Consequently, the net current available for the different experiments is in the range of 1-8 A.

In addition to the above gun, we have recently procured from SLAC a brand-new, state of the art, electron gun that can operate at 450 kV and a peak current of approximately 500 A. The advantage of this system over the previous one is our ability to operate at higher voltages and thus study the various coherent radiation mechanisms at considerably shorter wavelengths. Moreover, this gun is provided with an impregnated cathode which is much less prone to poisoning.

a) Short Period Wiggler for Free Electron Lasers.

Short period (1-5 mm) wigglers for free-electron laser (FEL) applications has been a subject of considerable interest.^{1,2} Besides its compactness, such a

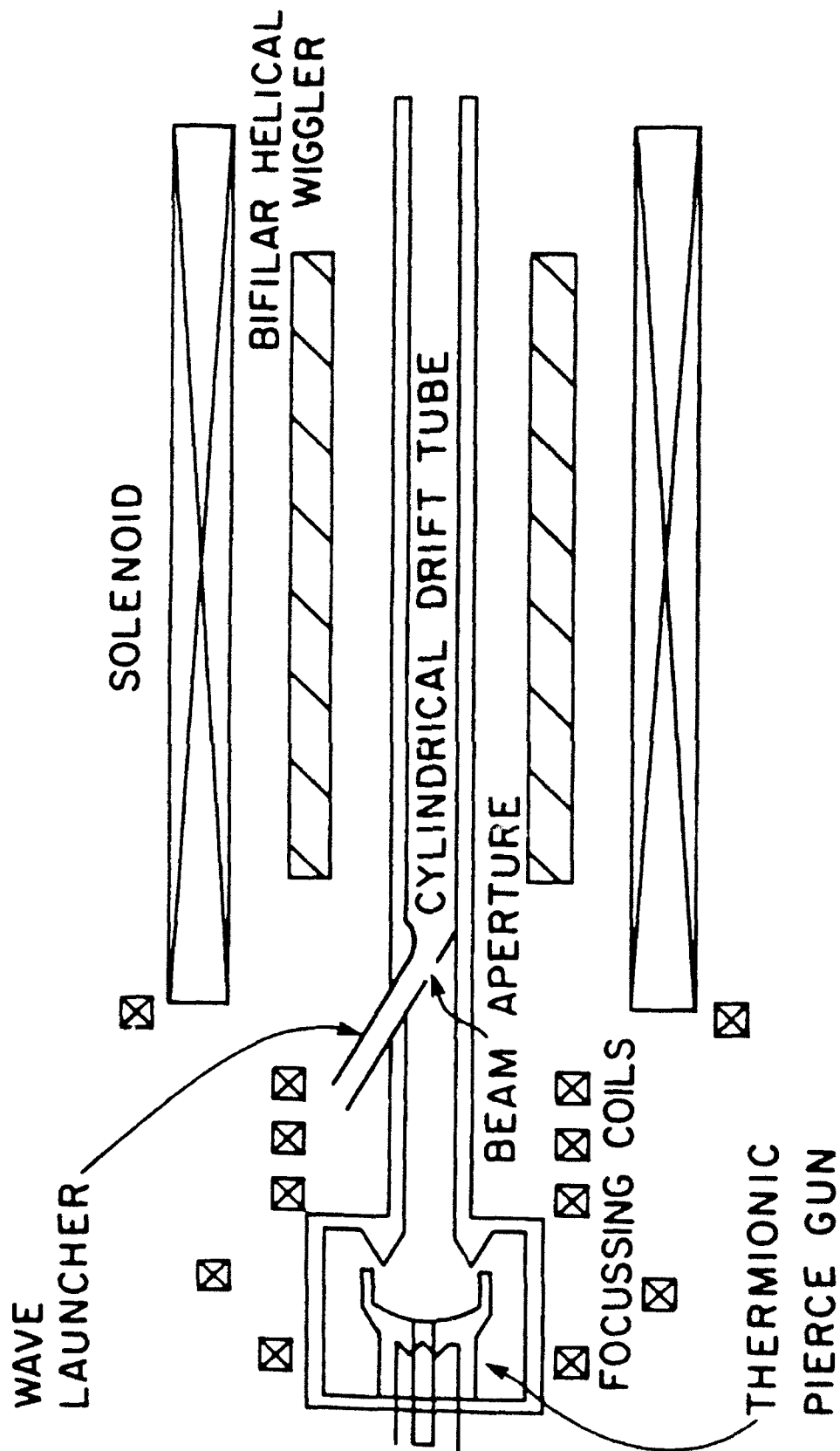


Fig. 1. Schematic of Raman FEL

system has the advantage of producing higher frequency radiation with a given electron energy, or conversely, it reduces the electron energy required to access a given wavelength. Here we describe a new scheme of fabricating micro-undulators with 2.4 mm period, 2 kG peak field on axis. In this magnetic structure, each period consists of two channels (electro-magnets) energized by current with opposite polarities, hence the magnetic field in each half period is independently controllable. The unique flexibility of this configuration, in principle, allows one to tune out some random errors associated with field variations in individual channels, and also permits field tapering for efficiency enhancement studies.

The construction of the micro-undulator is similar to that of the magnetic recording heads³ manufactured for precision applications. It is assembled in two half brackets, each with 60 precision-cut slots, held together with epoxy and bolts (see Figs. 2 and 3). Ferrite cores, wound with 160 turns of 40 gauge wire, are loaded into the slots in the half-brackets and potted. Terminal boards (electrical interfaces) are connected to the core windings and inserted into the half-brackets. The whole assembly is then lapped and gapped to the final configuration. All mechanical tolerances are held to within 0.3 mil. such that an undulator period error of less than 1% is achieved.

Preliminary field measurements of a 30 period prototype undulator and the design parameters of a submillimeter experiment driven by 450 keV electron beam will be performed. Using our short period wiggler, wavelengths of $\sim 400 \mu\text{m}$ can be achieved with good gain (see Table 1). We expect this experiment to continue for a period of 1-2 years.



Fig. 2. Microwiggler

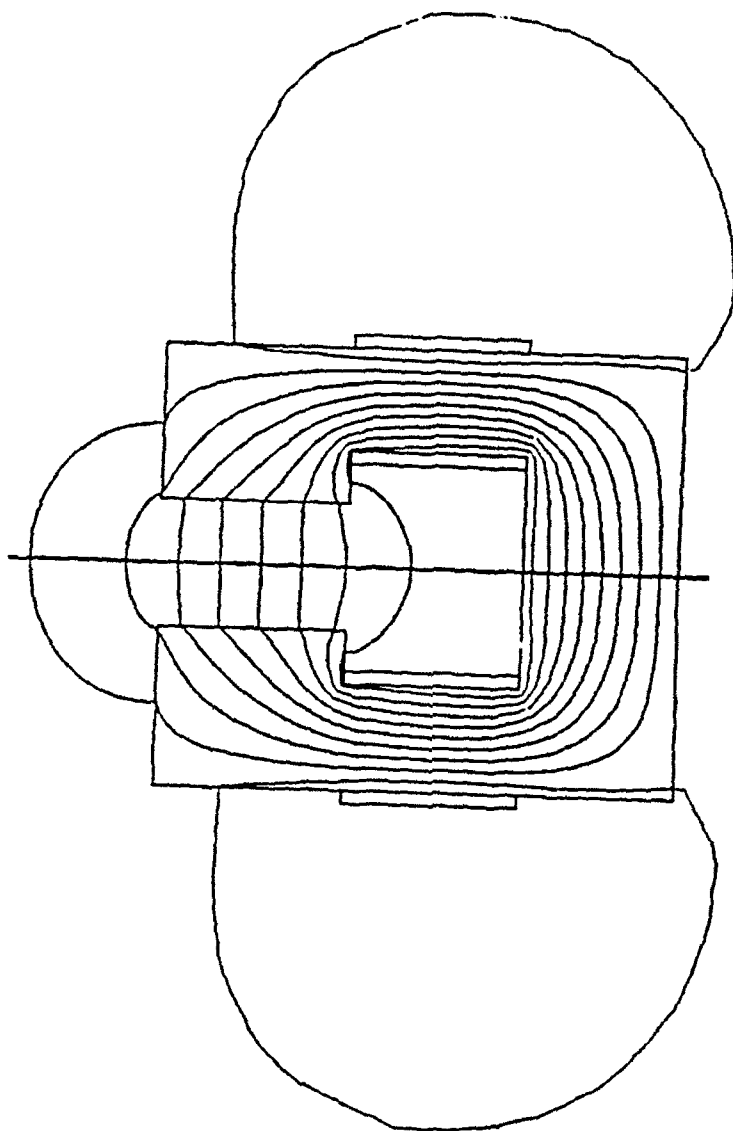


Fig. 3. 2D Magnetic Field Profile of a Microwiggler Ferrite Core

References

1. W.W. Destler, V.L. Granatstein, I.D. Mayergoyz, and Z. Segalov, J. Appl. Phys. 60, 521 (1986).
2. R.M. White, Appl. Phys. Lett., 46, 194 (1985).
3. J.L. Dimmers, J. British Kinematography Sound and Television Soc., 54, 234 (1982).

Table 1

FEL characteristics for radiation at a wavelength of $400\mu\text{m}$ using the microwiggler shown in Fig. 2. [Wiggler calibration measurements yield 160 Gauss per Ampere of input current.]

Electron Energy	450 keV
Peak Electron Energy	20 A
Beam Radius	0.5 mm
Wiggler Period	2.4 mm
Number of Periods	80
Wiggler Length	19.2 cm
Wiggler Field (1 μs pulse length)	2 kG
Single Pass Gain	15 dB

b) Studies of Optical Guiding and Profile Modification in a Raman FEL.

In our previous experiments (see Appendix 1) we have observed profile modifications caused by the free electron laser interaction. The modifications are a combination of two effects: a change in shape of the electromagnetic waveguide mode which the system supports, and the RF fields generated by the bunched electron beam. The net electric field as measured by our small dipole antennas represents the vector sum of these two contributions. The problem that needs to be addressed is the unfolding of these two fields. This can be done by noting that the electromagnetic wave component is purely linearly polarized, whereas the electric fields of the bunched beam have a roughly radial distribution near the beam center. Thus, by constructing dipole antennas sensitive to different polarizations should allow us to separate the electromagnetic and space charge components.

We have constructed such antennas as is illustrated in the schematic shown in Fig. 4. Figure 5 is a photograph of one of these antennas.

Initial measurements show that we can indeed measure the space-charge wave alone. The results give us some confidence that we shall therefore be able to separate out the electromagnetic components. We expect this experiment to continue for a period of 6-12 months. It is complementary to the studies being carried out at Columbia University¹ where multimode effects are investigated.

Reference

1. A. Bhattacharjee, S.Y. Cai, S.P. Chang, J.W. Dodd, and T.C. Marshall, Phys. Rev. Lett. 60, 1254 (1988).

c) Study of FEL Mode Competition.

The operation of free electron lasers at millimeter and submillimeter wavelengths requires a waveguide to confine the emitted radiation. Due to the finite transverse dimensions of the electron beam and of the electron or-

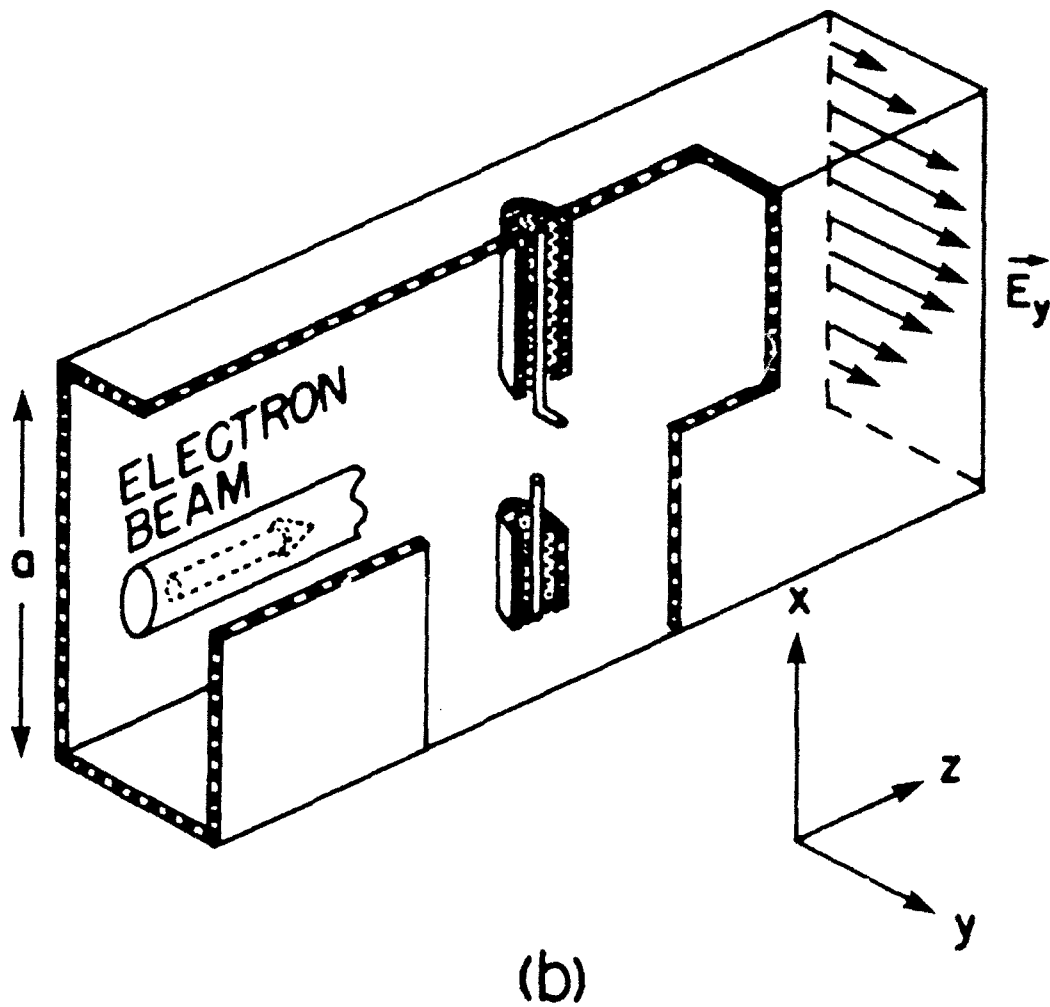
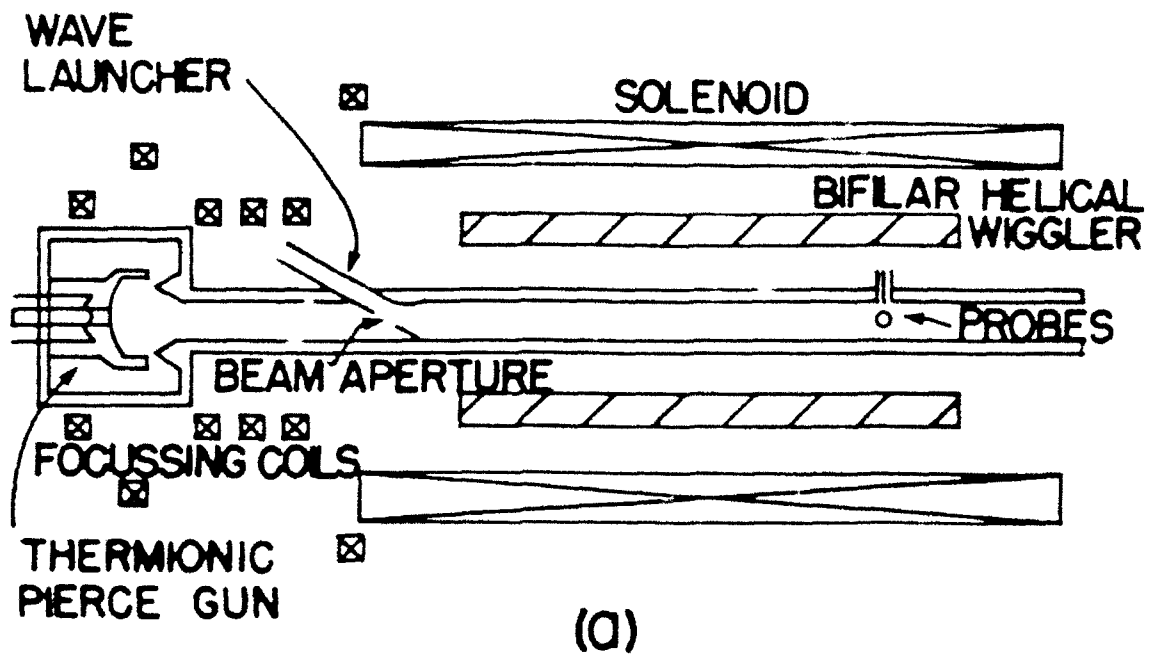


Fig. 4. Experimental setup used in studies of wave profile modification



Fig. 5. Photograph of movable dipole antenna for probing of waveguide fields

bits in the wiggler, the waveguide must usually be overmoded. In such circumstances more than one waveguide mode may, in fact, interact with the electron beam. Such coupling has been observed in the free electron experiments at the Lawrence Livermore National Laboratory¹ and nonlinear theory has also been developed.²

The above studies were carried out in the high gain, single particle regime. We plan to undertake an experimental and theoretical study of these phenomena in the collective Raman regime using our existing free electron laser facility.

We note that some interesting physics occurs even if the waveguide can support just one mode, and when two frequencies are injected simultaneously into the free electron laser interaction region. In a recent Bachelor Thesis experiment by Tamar More of our laboratory, two microwave signals of somewhat different frequencies were injected into the free electron laser interaction region. One of these frequencies corresponded to the free electron laser resonant condition, whereas, the other was slightly removed. The two waves were found to interact very strongly, causing quite dramatic changes in the free electron laser gain. The changes in gain became smaller and smaller, the larger the difference between the two frequencies. Since the perturbing wave was of very large amplitude, the phenomenon is clearly nonlinear in nature. We plan to undertake more detailed experimental studies of the phenomenon and use our nonlinear FEL codes to model the experiment.

References

1. T.J. Orzechowski, B. Anderson, W.M. Fawley, D. Prosnitz, E.T. Scharlemann, S. Yarema, D.B. Hopkins, A.C. Paul, A.M. Sessler and J.S. Wurtele, these Proceedings (7th Int. FEL Conf.) Nucl. Instr. and Meth. A250, 144 (1986).
2. J.S. Wurtele, E.T. Scharlemann, and A.M. Sessler, Nucl. Instr. and Meth. A250, 176 (1986).

(d) Effect of Electron Prebunching on the Radiation Growth Rate in a Collective (Raman) Free Electron Laser Amplifier

Experiments are being carried out on the effects of electron prebunching in a mildly relativistic (~ 200 keV) free electron laser amplifier operating¹ in the collective (Raman) regime at a frequency of ~ 10 GHz. Prebunching is established by injecting a monochromatic wave into a bifilar helical wiggler interaction region as is done in conventional free electron laser amplifiers, and then transporting the bunched beam into a second magnetic wiggler region. The growth rates are deduced from observations of the radiation intensity as a function of interaction length. Results are presented both in the small signal (linear) and saturated (nonlinear) regimes. Measurements show that such a "transverse optical klystron"² exhibits a manyfold increase in the radiation growth rate as compared with a system without prebunching (see Figs. 6 and 7 and Appendix 2).

We plan to continue with these studies during the forthcoming year.

References

1. J. Fajans and G. Bekefi, Phys. Fluids 29, 3461 (1986).
2. R. Coisson, in "Particle Accelerators" Gordon and Breach Science Publishers (1981) p. 245.

(e) Experiments with a 35 GHz Cyclotron Auto Resonance Maser (CARM)

Initial studies of a cyclotron auto resonance maser (CARM) have begun. The measurements are carried out at a frequency of ~ 35 GHz using a mildly relativistic electron beam of ~ 1.5 MeV energy and ~ 250 A current. The beam is generated by a field emission electron gun (~ 1.5 MeV, ~ 20 kA) followed by an emittance selector that removes $\sim 99\%$ of the outer, hot electrons. The en-

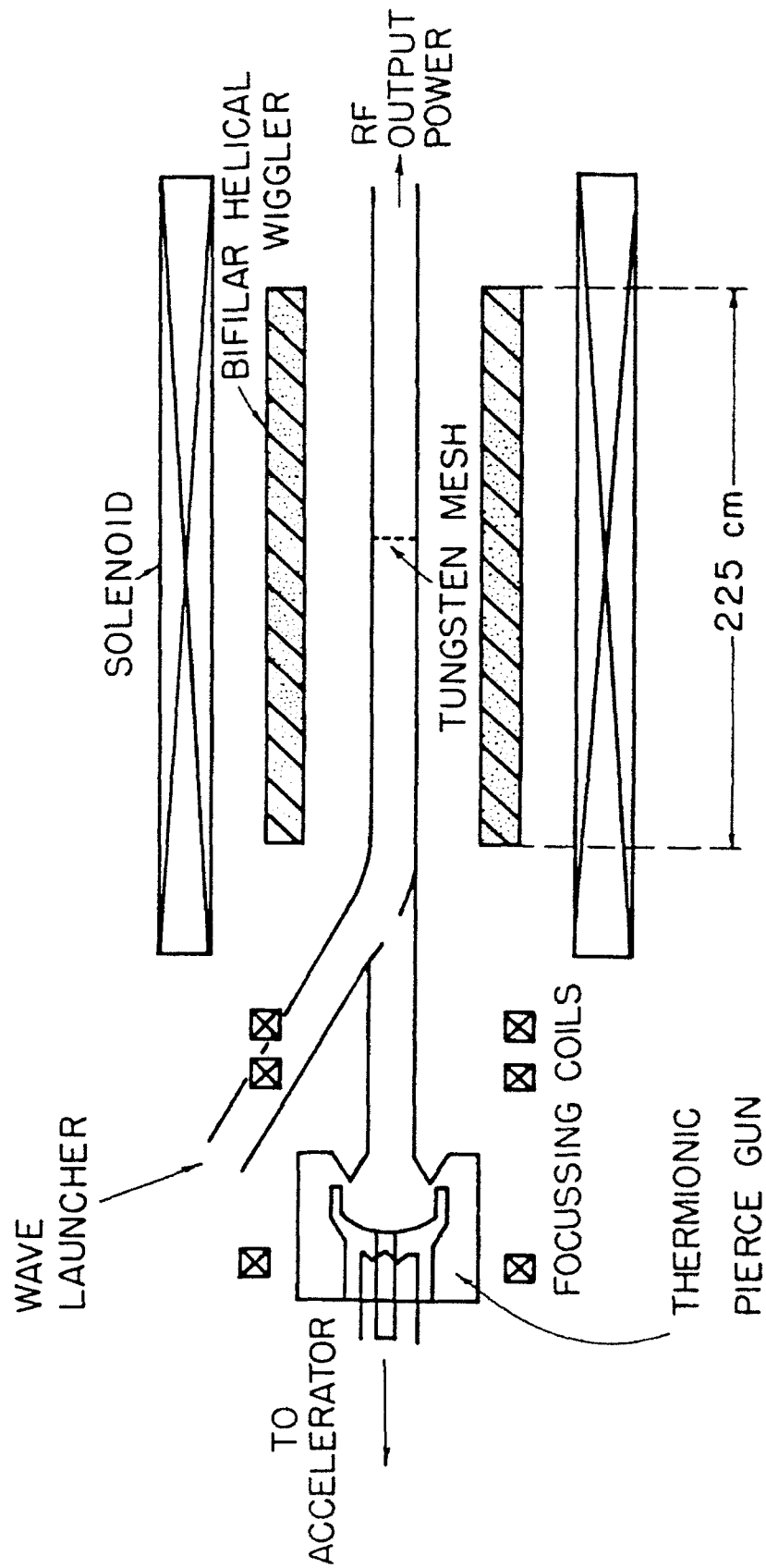


Fig. 6

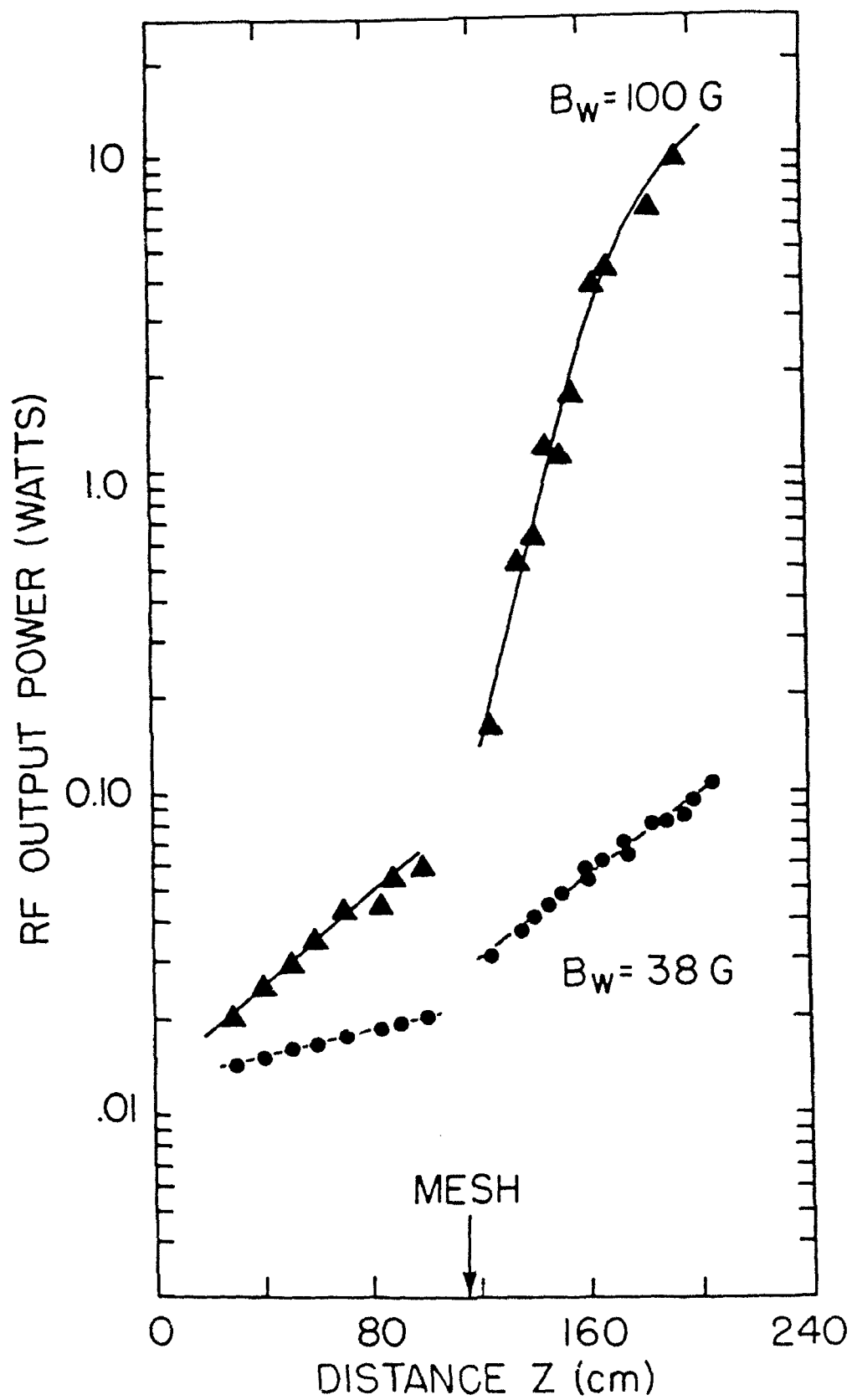


Fig. 7

tire system (length $\sim 1.7\text{m}$), including the field emission gun, is immersed in a uniform solenoidal guide field that can be varied from zero to $\sim 15\text{ kG}$. Perpendicular energy ($v_{\perp}/c \approx 0.3$) is imparted to the electrons by means of a bifilar helical wiggler having a period of 7 cm and a length of $\sim 70\text{ cm}$. The cyclotron radiation is generated in a 1m long wiggler free region.

This work, which is in its very initial stages, is expected to continue for approximately 2-3 years. A.C. Dirienzo, a new graduate student, is in charge of this work. This project is funded entirely by AFOSR.

PROJECT PERIOD
November 1, 1989 - October 31, 1990

Table of Contents

Project summary	19
A 35 GHz cyclotron autoresonance maser (CARM) amplifier	20
A high efficiency 35 GHz UBITRON amplifier	28
Prebunching in a collective Raman free electron laser amplifier (Appendix 1)	32
Observation of field profile modifications in a Raman free electron laser amplifier (Appendix 2)	64

Project Summary

This is a continuation proposal on Microwave Emission from Relativistic Beams for the grant period of November 1, 1989 to October 31, 1990. Below we summarize the major research activities supported entirely or in part by the Air Force Office of Scientific Research.

The primary objective of the group is to develop a basic experimental and theoretical understanding of coherent generation by free electrons for wavelengths in the $1\mu\text{m}$ to 10 cm range. Particular emphasis is placed on free electron lasers, Čerenkov sources, relativistic magnetrons and other novel radiation sources.

The experiments are carried out on four high-voltage pulsed accelerators available in our laboratory. Their characteristics are summarized as follows:

Accelerator	Voltage	Current	Pulse Length	Repetition Range
Physics International Pulserad 110A	1.5 MV	20 kA	30 nsec	n/a
Nereus Accelerator	600 kV	150 kA	30 nsec	n/a
Physics International 615MR Pulserad	500 kV	4 kA	1 μ sec	n/a
High Voltage Modulator	700 kV	600 A	1 μ sec	1 pps

(a) A 35 GHz CYCLOTRON AUTORESONANCE MASER (CARM) AMPLIFIER

The cyclotron autoresonance maser (CARM) has been subjected to extensive theoretical [1],[2] studies and numerical simulations [3]-[5]. However, unlike the gyrotron and the free electron laser, its capabilities as a source of coherent millimeter wavelength radiation remain virtually untested in the laboratory. To the best of our knowledge, only CARM oscillator experiments [6],[7] have been reported in the literature. We present here what we believe to be the first, albeit preliminary, studies of a CARM amplifier.

The emission from a CARM results through an interaction between the Doppler upshifted cyclotron wave on the electron beam

$$\omega = \Omega_0/\gamma + k_{\parallel}v_{\parallel} \quad (1)$$

and an electromagnetic waveguide mode

$$\omega^2 = k_{\parallel}^2 c^2 + \omega_c^2; \quad (2)$$

ω and k_{\parallel} are the frequency and axial wavenumber respectively; $\Omega_0 = eB_{\parallel}/m$ is the non-relativistic electron cyclotron frequency associated with an axial guide magnetic field B_{\parallel} ; $\gamma = [1 - (v_{\parallel}/c)^2 - (v_{\perp}/c)^2]^{-1/2}$ is the relativistic energy factor; and ω_c is the cutoff frequency of the waveguide mode in question. Maximum gain of the CARM instability occurs near phase velocity synchronism of the two waves. This yields the radiation frequency:

$$\omega \simeq \Omega_0 \frac{\gamma_{\parallel}^2}{\gamma} \left\{ 1 \pm \beta_{\parallel} \left[1 - \left(\frac{\omega_c \gamma}{\Omega_0 \gamma_{\parallel}} \right)^2 \right]^{1/2} \right\} \quad (3)$$

Here $\beta_{\parallel} = v_{\parallel}/c$, $\gamma_{\parallel} = (1 - \beta_{\parallel}^2)^{-1/2}$, and the positive sign refers to the sought after Doppler upshifted CARM mode of operation.

A schematic of the CARM amplifier is shown in Fig. 1. The accelerator potential is supplied by a Marx generator (Physics International Pulserad 110 A) with a maximum capability of 1.5 MV and 20 kA. The electron beam is generated by a field emission gun composed of a hemispherical graphite cathode and conical anode, which also acts as an emittance selector. The entire two meter long system is immersed in a uniform solenoidal magnetic field of 7 kG.

The 260 A, 1.5 MV beam that issues from the emittance selector has a radius of 0.254 cm and a measured [8] normalized beam brightness equal to $2.4 \times 10^4 \text{ A cm}^{-2} \text{ rad}^{-2}$. This corresponds to a normalized RMS emittance of $4.9 \times 10^{-2} \text{ cm-rad}$ and an RMS energy

spread $\Delta\gamma_{||}/\gamma_{||} \simeq 0.019$. We note that considerably higher beam brightness is achieved by sacrificing current. When the radius of the emittance selector is reduced to 0.076 cm, the current drops to 8.4 A, but the brightness increases to $9.5 \times 10^4 \text{ A cm}^{-2}\text{rad}^{-2}$. The corresponding emittance is now 4.5×10^{-3} and the energy spread $\Delta\gamma_{||}/\gamma_{||} \simeq 0.0017$.

The aforementioned 260 A electron beam is injected into the bifilar helical wiggler which imparts perpendicular energy to the electrons. The wiggler has a periodicity of 7 cm and is six periods long. Within the first four periods, the wiggler magnetic field increases slowly and thereby provides an adiabatic input for the electron beam; the last two periods provide a uniform wiggler field with an amplitude on axis equal to 460 G. The resulting transverse electron velocity ($v_{\perp} \simeq 0.3v_{||}$) is estimated from witness plate observations of the beam dimensions.

The downstream end of the wiggler is terminated abruptly by means of a metal shorting ring and the spinning electrons are allowed to drift into the 100 cm-long CARM interaction region where they are subjected to the uniform axial magnetic field only. We note that as a result of the wiggler excitation and the abrupt wiggler termination, the energy spread $\Delta\gamma_{||}/\gamma_{||}$ of the electrons entering the CARM region can be considerably worse than the energy spreads quoted above in reference to electrons leaving the emittance selector.

The $\sim 2\text{m}$ long, 0.787 cm radius evacuated drift tube acts as a cylindrical waveguide whose fundamental TE_{11} mode has a cutoff frequency $\omega_c/2\pi = 11.16 \text{ GHz}$. Substituting this value of ω_c in Eq. 3, together with the remaining experimental parameters, yields the desired 35 GHz radiation frequency.

Fig. 2 illustrates the time history of the voltage, current and radiation characteristics of the device. The CARM has been operated in the superradiant mode, in which the signal is allowed to grow out of background RF noise.

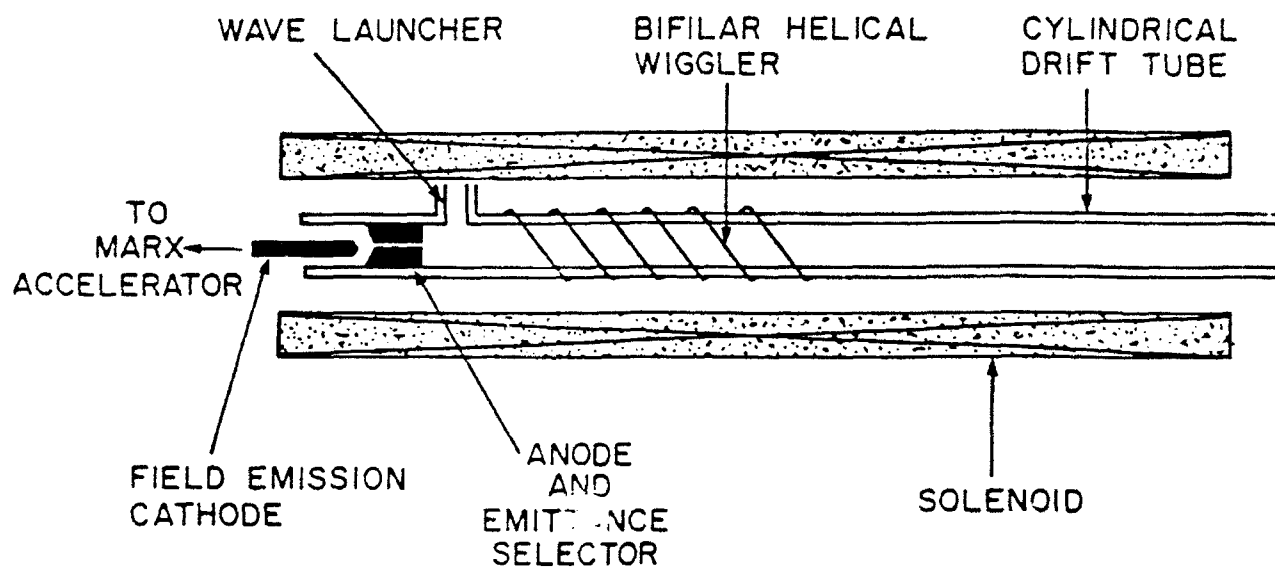
At the output end of the CARM, a mica window transmits the circularly polarized radiation generated in the drift tube, where it is measured by means of standard calibrated crystal detectors, and its spectrum is analyzed by means of a 98m-long dispersive line. In order to determine the growth rate of the wave, the output intensity is measured as a function of the length of the interaction region. This is accomplished by means of an axially movable horse-shoe "kicker" magnet that deflects the electron beam into the waveguide wall at any desired position z , thereby terminating the interaction at that point. Fig. 3 shows how the RF power output measured at the far downstream end varies with the "kicker" magnet position z . The slope of the curve yields a single pass gain of 0.9 dB/cm, a value that is consistent with computer simulations presented in Fig. 4.

Under the aegis of this contract we propose to inject a 35 GHz monochromatic signal from a high power magnetron driver and study various aspects of the CARM amplifier. The work will include the following:

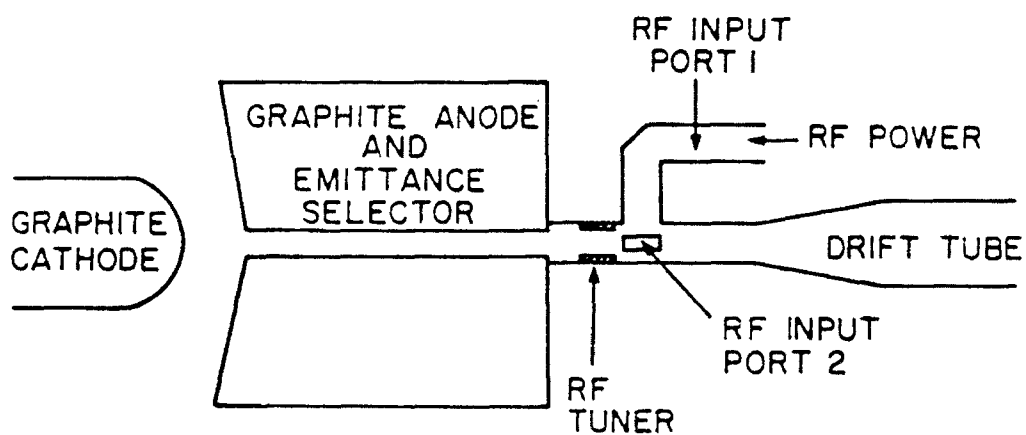
1. Linear growth rate measurements.
2. Nonlinear saturation effects.
3. Phase characteristics in both the high gain and low gain regimes.

4. Efficiency optimization by improving wiggler characteristics and by magnetic field tapering.

We expect these studies to take approximately two years.



(a)



(b)

Figure 1

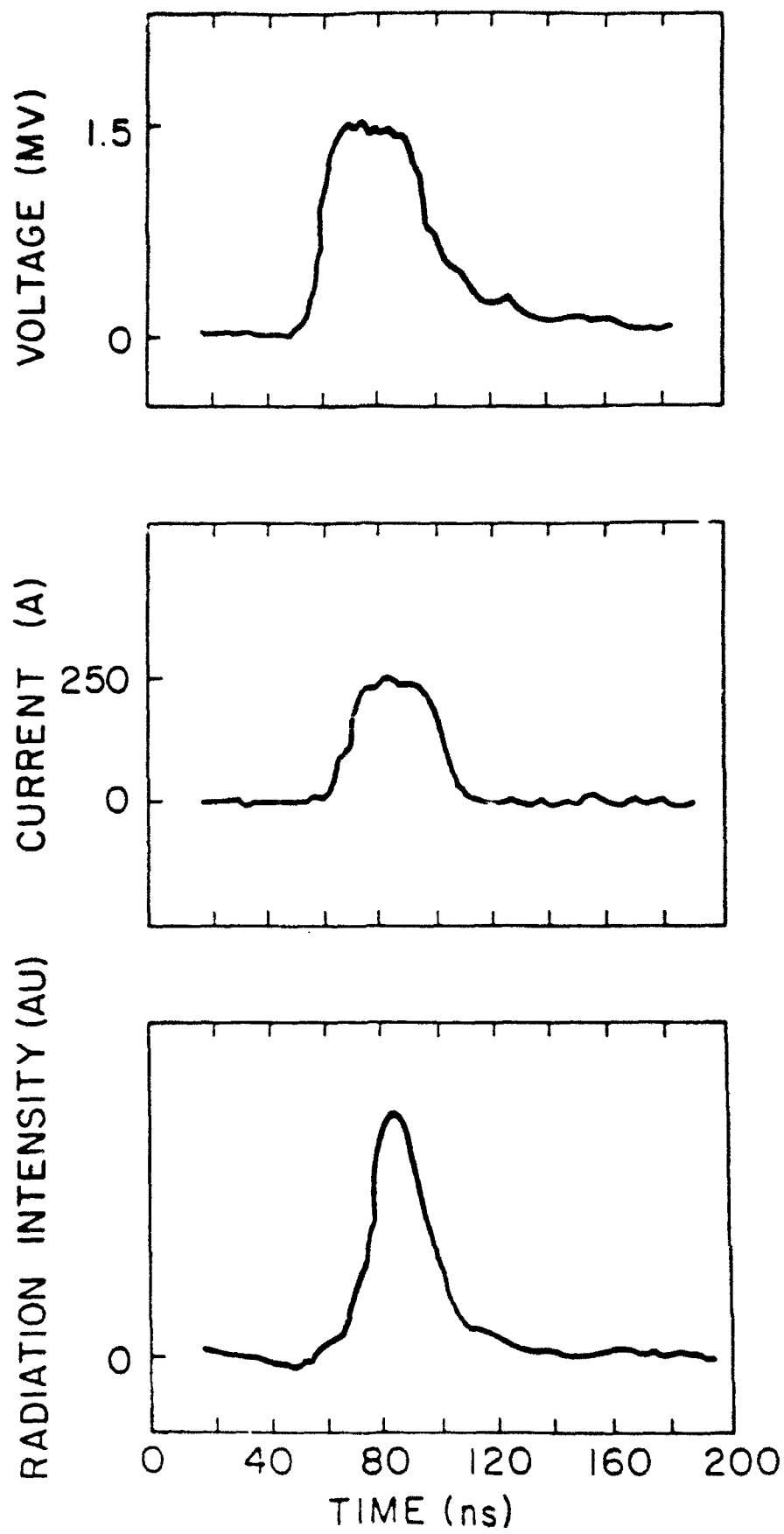


Figure 2

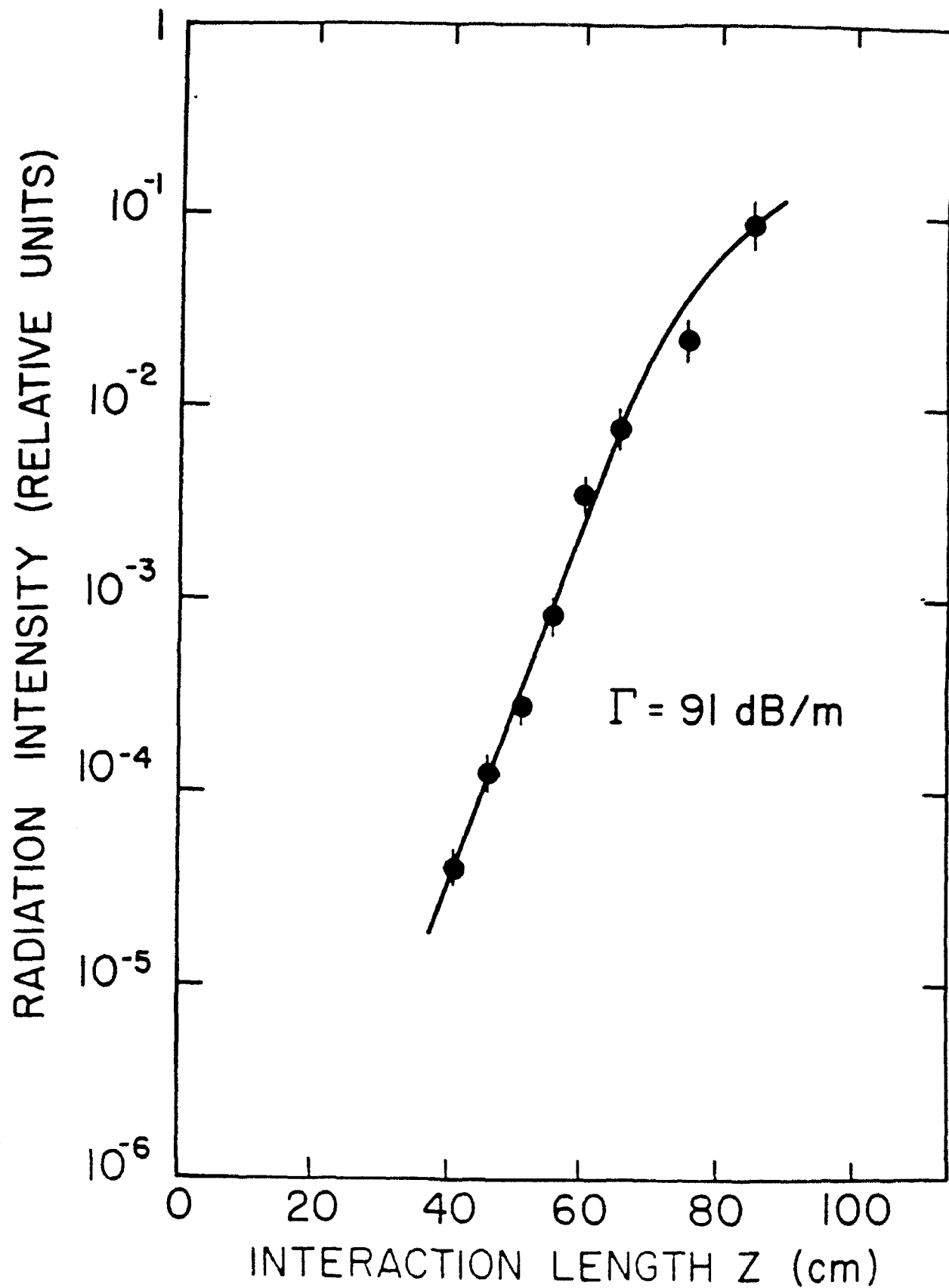


Figure 3

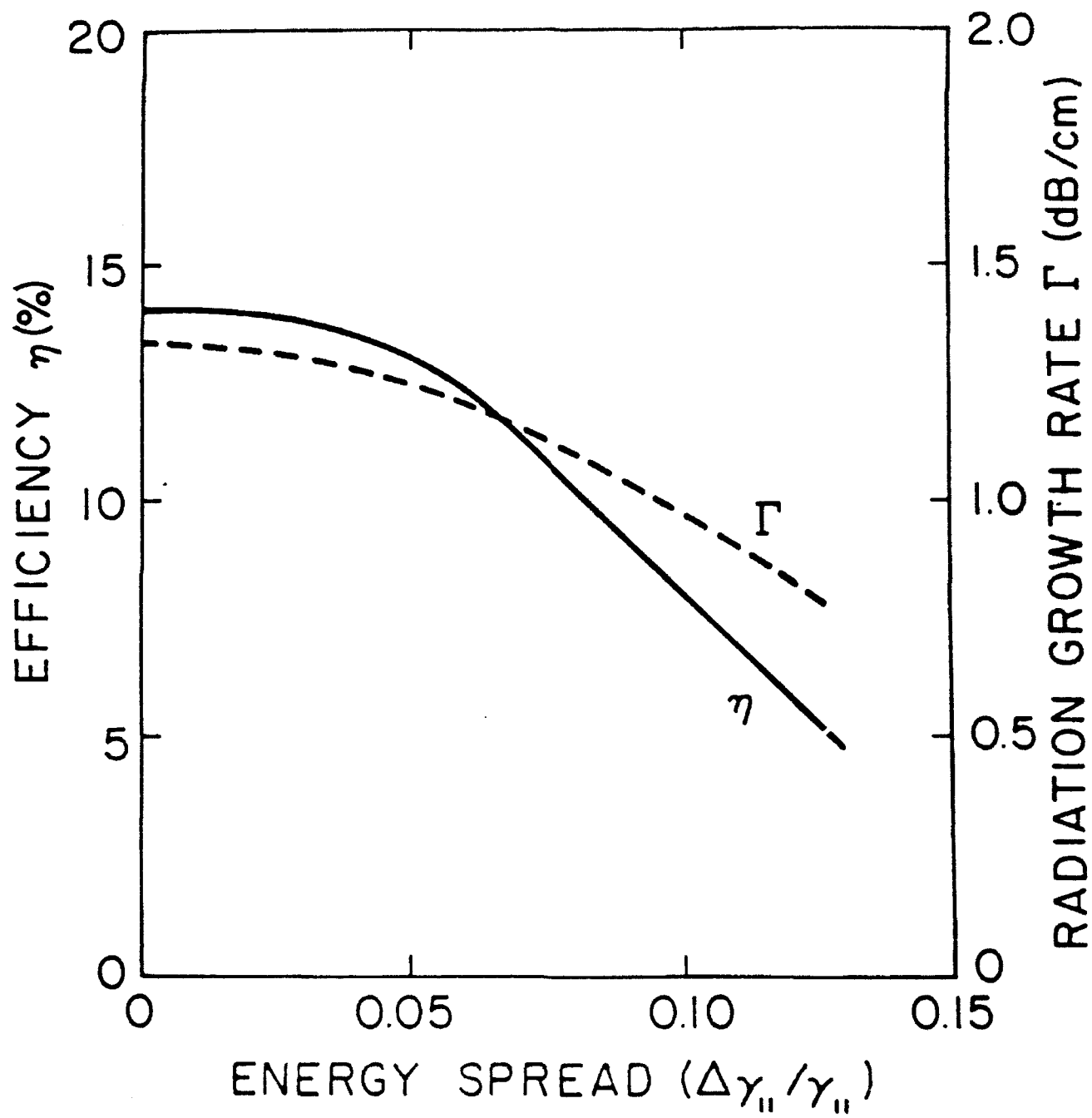


Figure 4

References

1. A.W. Fliflet, *Int. J. Electron.*, **61**, 1049-1080 (1986).
2. V.L. Bratman, N.S. Ginzburg, G.S. Nusinovich, M.I. Petelin and P.S. Strelkov, *Int. J. Electron.*, **51**, 541-567 (1981).
3. K.D. Pendergast, B.G. Danly, R.J. Temkin, and J.S. Wurtele, submitted to *IEEE Trans. Plasma Sci.*, April (1988).
4. A.T. Lin, *Int. J. Electron.*, **57**, 1097-1108 (1984).
5. B.G. Danly, K.D. Pendergast, R.J. Temkin, and J.A. Davies, *Proc. SPIE* **873**, (1988).
6. I.E. Botvinnik, V.L. Bratman, A.B. Volkov, N.S. Ginzburg, C.G. Denisov, B.D. Kol'chugin, M.M. Ofitserov, and M.I. Petelin, *Pis'ma Zh. Eksp. Teor. Fiz.*, **35**, 418-420 (1982).
7. I.E. Botvinnik, V.L. Bratman, A.B. Volkov, G. Denisov, B.D. Kol'chugin, and M.M. Ofitserov, *Pis'ma Zh. Eksp. Teor. Fiz.*, **8**, 1376-1378 (1982).
8. The technique is described by D. Prosnitz and E.T. Scharlemann, Lawrence Livermore National Laboratory, ATA Note No. 229, Feb. 22 (1984).

(b) A HIGH EFFICIENCY 35 GHz UBITRON AMPLIFIER

Low frequency FELs (generally called UBITRONS) often operate in combined wiggler and axial magnetic fields [1,2]. The axial magnetic field B_z provides focussing of the mildly relativistic electron beam. At low magnetic fields the FEL gain and efficiency characteristics are by and large very similar to conventional FELs without axial field focussing. However, at large fields such that

$$\Omega_c \gtrsim k_w v_b, \quad (1)$$

Ganguli and Freund [3,4] have shown that important changes occur (Ω_c is the relativistic electron cyclotron frequency associated with B_z , k_w is the wiggler wave number, and v_b is the axial electron velocity).

In the regime defined by inequality 1 above, the FEL interaction is strongly coupled to the intrinsically unstable space charge wave on the beam. This leads to a dramatic increase in the FEL efficiency.

We have carried out numerical simulations for a 35 GHz frequency system with parameters given in the table below.

Beam voltage	1.8 MV
Beam current	300 A
Axial magnetic field	10.8 kG
Wiggler magnetic field	1.7 kG
Wiggler period	7 cm
Calculated efficiency	57%

Fig. 1 illustrates a typical energy versus phase diagram (at an axial distance of 60 cm), showing strong bunching. Fig. 2 shows a plot of output power versus axial position. Computations yield an electronic efficiency of 57% for an electron beam with an initial energy spread of 4%.

We propose to carry out this experiment using our PI 110 A accelerator. We have a high power 35 GHz magnetron driver, as well as the wiggler and all other auxiliary equipment. The experimental program will be well integrated with theoretical and numerical studies. The project is expected to last 2-3 years and will include both linear and nonlinear studies.

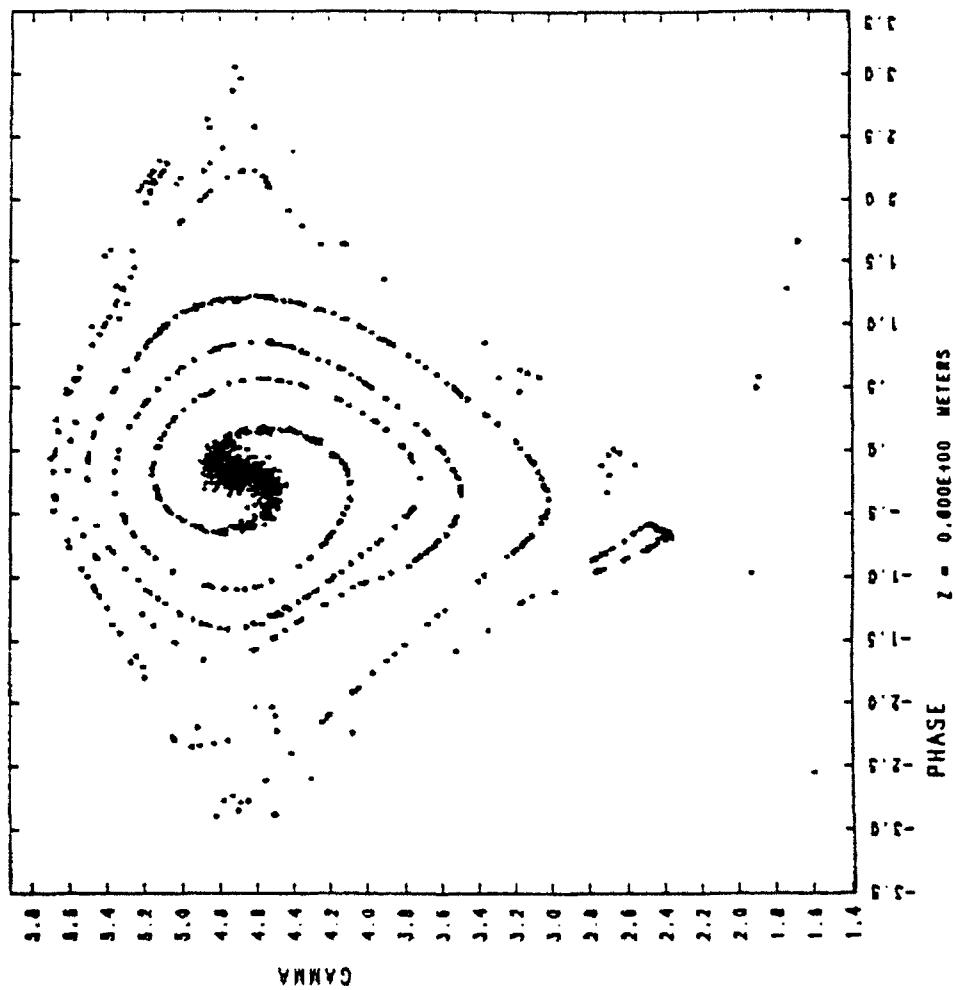


Figure 1

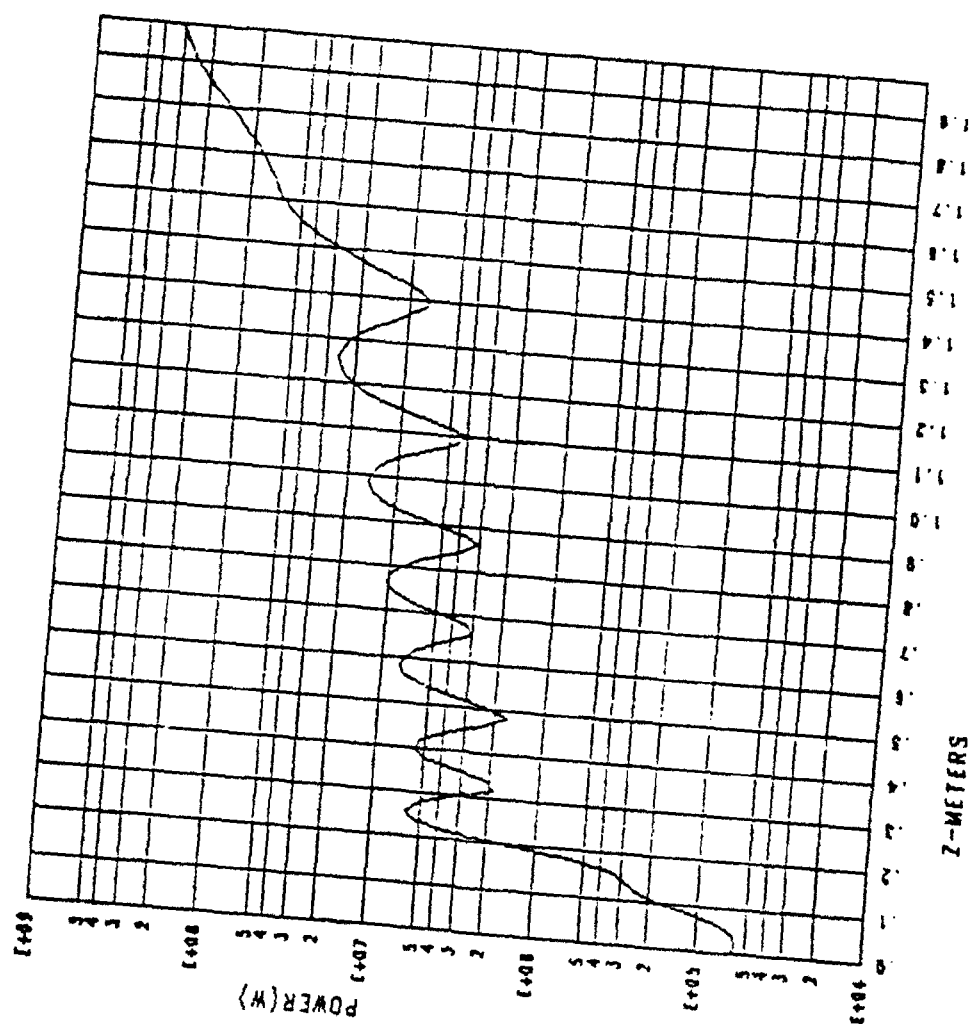


Figure 2

References

1. J. Fajans and G. Bekefi, Phys. Fluids **29**, 3461 (1986).
2. J. Fajans, J.S. Wurtele, G. Bekefi, D.S. Knowles and K. Xu, Phys. Rev. Letters **57**, 579 (1986).
3. A. K. Ganguli and H. P. Freund, Phys. Rev. **A32**, 2275 (1985).
4. A. K. Ganguly and H. P. Freund, IEEE Trans. Plasma Science **16**, 167 (1988).

APPENDIX 1

Prebunching in a Collective Raman Free Electron Laser Amplifier

J. S. Wurtele, G. Bekefi, R. Chu, and K. Xu

Department of Physics,

Research Laboratory of Electronics,

and

Plasma Fusion Center,

Massachusetts Institute of Technology,

Cambridge, MA 02139

April 5, 1989

Abstract

Experiments, theory, and simulations are reported on the effects of electron prebunching in a mildly relativistic, low current (200 kV, 1A) free-electron laser amplifier operating in the collective (Raman) regime at a frequency of ~ 10 GHz. Prebunching is established by injecting an electromagnetic wave into a bifilar helical wiggler and then transporting the bunched beam into a second magnetic wiggler region. The wave growth rate is deduced from measurements of the radiation intensity as a function of interaction length. Observations show that prebunching can increase the radiation growth rate manyfold as compared with a system without prebunching.

1 INTRODUCTION

Experimental and theoretical studies [1] of prebunching in free electron lasers (FELs) are normally carried out in the low gain, single particle (Compton) regime applicable to very short radiation wavelengths (visible and ultraviolet) where electron beam energies in excess of several hundred MeV are used. In contrast, our experiments [2] are made at microwave frequencies using mildly relativistic electrons (~ 200 keV). In this collective (Raman) regime, the gains are high and the effects of space charge cannot be neglected. We find that prebunching increases the growth rate of the radiation dramatically as compared with the case where prebunching has not been incorporated. In this paper the experiments are compared with computer simulations and good agreement is obtained. In addition, a simple analytic theory is given.

2 EXPERIMENTAL ARRANGEMENT

Fig. 1 shows a schematic of our experiment. The accelerating potential is supplied by a Marx generator (Physics International Pulserad 615 MR, which has a maximum capability of 500 kV and 4 kA). The electron beam is generated by a thermionically emitting, electrostatically focused, Pierce-type

electron gun (250 kV, 250 A) from a SLAC klystron (model 343). An assembly of focusing coils transports the electron beam into the drift tube. To ensure good electron orbits, an aperture is inserted which limits the electron beam radius to $r_b = 0.245$ cm so that only the inner portion of the beam is used. With this precaution, the energy spread of the beam entering the magnetic wiggler is $\Delta\gamma_{||}/\gamma_{||} \leq 0.003$ ($\gamma_{||} = [1 - v_{||}^2/c^2]^{-1/2}$).

The gun focusing coils guide the electron beam into a rectangular (0.40" x 0.90") stainless steel evacuated drift tube which is also the waveguide for the electromagnetic radiation. The beam is contained by a uniform axial magnetic field $B_{||}$ that has a power supply limited maximum of 7 kG.

The 65 period circularly polarized magnetic wiggler has a period $l_w = 3.5$ cm, a maximum amplitude $B_w = 1.0$ kG, and is generated by bifilar conductors. Since the beam aperture limits the size of the beam to $r_b/l_w \approx 0.07$, the wiggler field is close to that of an ideal wiggler. At the wiggler entrance a slowly increasing field amplitude is produced by resistively loading the first six periods of the wiggler magnet.

The 2.7 m long drift tube acts as a rectangular waveguide whose fundamental TE_{10} mode has a cutoff frequency of $\omega_c/2\pi = 6.6$ GHz. Microwaves are launched onto the electron beam by a waveguide coupler (see Fig. 1).

All our measurements are carried out at frequencies between 9 and 11 GHz. At these frequencies the empty waveguide can support only the fundamental (TE_{10}) mode, all higher modes being evanescent.

Monochromatic radiation as high as 20 kW is injected into the interaction region via the directional coupler. At low power levels (≤ 10 W) we use a CW traveling wave tube as the input source. At higher power levels we use a pulsed ($\sim 1\mu s$) magnetron driver. Because of the low conductivity of the stainless steel waveguide, there is an RF power loss of ~ 0.9 dB/m, or a 3 dB loss over the entire system length.

3 MEASUREMENTS

The interaction space is divided into two roughly equal lengths by means of a tungsten mesh stretched across the waveguide (see Fig. 1) and placed at an axial distance $z = z^* \simeq 115$ cm from the wiggler entrance. The mesh is almost totally transparent (~ 94 percent) to the electron beam generated to the left of the mesh, but highly reflecting to the electromagnetic radiation incident upon it. Thus, the left-hand side can be viewed as the prebunching region where spatially growing bunches are induced by the conventional FEL

mechanism. The bunched beam then traverses the mesh almost unhindered and immediately interacts with the weak electromagnetic wave that has been allowed to pass through the mesh. (The mesh attenuation of the wave incident from the left equals 20.0 dB.) Beyond the mesh the electromagnetic wave grows spatially, and additional bunching also occurs. In this region, an enhanced wave growth rate is expected, because the electrons enter pre-bunched. The use of the mesh rather than an RF attenuator of finite axial extent, as is common in TWT's [3], minimizes the possibility of debunching with distance, as may well occur as a result of space charge repulsion and/or Landau damping of the pondermotive wave.

At the output end of the wiggler, a mica window transmits the linearly polarized radiation generated in the drift tube, where it is measured by means of standard calibrated crystal detectors. In order to determine the growth rate of the wave, the output intensity must be measured as a function of the length of the interaction region. This is accomplished by means of an axially movable horseshoe "kicker" magnet that deflects the electron beam into the waveguide wall at any desired position z , thereby terminating the interaction at that point. The position z can be chosen to be to the left or to the right of the tungsten mesh (situated at $z = z^* \simeq 115$ cm).

Fig. 2 shows how the RF power output P measured at the far downstream end varies with the "kicker" magnet position z , for two different values of the wiggler strength B_w . As a result of prebunching, we see that to the right of the mesh the power rises much more rapidly with z than to the left of the mesh. The phenomenon is quite dramatic. For example, in the case of the $B_w = 188$ G wiggler field, the radiation growth rate $\Gamma(z < z^*) \equiv (1/P)dP/dz$ equals 6.9 dB/m, whereas to the right of the mesh, $\Gamma(z > z^*) = 32$ dB/m. Note, however, that for our parameters the gain G , namely the ratio of total output power to the total injected power (at $z = 0$), is somewhat less relative to what G would have been in the absence of the mesh. The reason is the 20 dB loss due to the mesh which has not been made up by the increased growth rate Γ at $z > z^*$.

Fig. 3 shows how the power $P(z)$ varies with z for three different values of the input power P_{in} ranging from 0.3 to 40 W. The wiggler strength B_w is the same for all three values of P_{in} . It is seen that the growth rate Γ (given by the slopes of the curves) are virtually independent of the input power.

Fig. 4 illustrates the time history of our FEL as observed on an oscilloscope screen. Since our Marx accelerator has an RC droop, the electron beam energy sweeps through a range of values as seen in Fig. 4a. Thus, in

a single shot one observes the entire range of FEL interactions as a function of electron beam energy. Fig. 4b shows how the power output varies with beam energy at $z < z^*$ when a monochromatic, CW signal is injected into the interaction region via the wave launcher (see Fig. 1). Amplification occurs at a time during the voltage pulse corresponding to the resonant interaction between the injected electromagnetic wave and the slow (negative energy) space charge wave on the beam. At a later time wave damping is seen to occur corresponding to the interaction between the electromagnetic and fast (positive energy) space charge wave. Fig. 4c shows the behavior to the right of the mesh $z > z^*$. We see that the absorption dip in Fig. 4b now appears as a gain peak in 4c.

4 THEORY AND SIMULATIONS

A simulation code which will be described in an upcoming paper [4] is used to simulate the experiments. The computer code utilizes an extended one dimensional model to track the nonlinear electron motions in the (γ, ψ) space. Instead of assuming a helical wiggler field with constant amplitude, the code includes Bessel functions in the wiggler field to generate more realistic elec-

tron orbits. The presence of an axial magnetic field and RF space charge are also included. The signal power is then given by the self-consistent coupling between the electron beam and the fundamental TE_{10} mode.

Figs. 5 and 6 show the computer simulations of the experimental results shown in Figs. 2 and 3a. The simulations and the experiments can be seen to be in good agreement. Fig. 7 shows the simulations of the experimental results shown in Figs. 4b and 4c. The simulations show that the absorption dip in the prebunching section turns into a gain peak in the section to the right of the mesh, just as observed in the experiments.

The dramatic increase in the radiation growth rate Γ is a direct result of prebunching. But in order to understand the phenomenon quantitatively, a simple analytic theory is derived. This theory will then be shown to give results that are in excellent agreement with simulations.

Before the equations of motion are stated, it is convenient to introduce the dimensionless field variable

$$a = \frac{\sqrt{PZ_0}}{mc^2/e} e^{i\phi}, \quad (1)$$

where $\phi(z)$ is the phase shift due to the FEL interaction. P is the RF power and $Z_0 = \sqrt{\mu_0/\epsilon_0}$ is the characteristic impedance of vacuum. An appropriate

length scale is defined as

$$C = \sqrt{\frac{\omega}{ck_z ab}}, \quad (2)$$

where a and b are the linear dimensions of the rectangular waveguide, ω the radiation frequency and k_z the axial wave number.

The general equations of motion [4] hold in both sections to the left and to the right of the mesh. For simplicity and clarity these equations are written in complex forms in terms of the relativistic energy factor γ_j and the normalized axial $\beta_{\parallel j}$ and transverse $\beta_{\perp j}$ velocities of the j th particle as,

$$\frac{d\gamma_j}{dz} = \frac{iC\beta_{\perp j}}{2\beta_{\parallel j}} a e^{i\theta} - \frac{i\omega_{p0}^2 f_{sc}^2}{c^2(k_z + k_w)} e^{i\theta} \langle e^{-i\theta} \rangle + \text{c.c.}, \quad (3)$$

$$\frac{d\theta_j}{dz} = k_w + k_z - \frac{\omega}{c\beta_{\parallel j}}, \quad (4)$$

$$\frac{da}{dz} = \frac{iCI}{2I_A} \left\langle \frac{\beta_{\perp}}{\beta_{\parallel}} e^{-i\theta} \right\rangle. \quad (5)$$

ω_{p0} is the nonrelativistic plasma frequency,

$$\omega_{p0} = \sqrt{\frac{Z_0 e I}{m \pi r_e^2 \beta_{\parallel 0}}}. \quad (6)$$

with I as the beam current, r_e the beam radius and $I_A = 17kA$ the Alfen current; the space charge reduction factor $f_{sc} \sim 0.5$ [4] for the parameters of our experiments.

First we consider the section to the left of the mesh ($z < z^*$) where normal

FEL interactions with no prebunching take place. For simplicity a cold beam is assumed. The linearization proceeds by defining

$$\Delta k = k_w + k_z - \frac{\omega}{c\beta_{||0}}, \quad (7)$$

$$\gamma_j = \gamma_0 + \delta\gamma_j, \quad (8)$$

$$\theta_j = \theta_{j0} + \Delta kz + \delta\theta_j, \quad (9)$$

$$\eta = \frac{CI}{2I_A}, \quad (10)$$

$$\eta_{||} = \frac{\omega_{p0}^2 f_{sc}^2}{c^2(k_w + k_z)}. \quad (11)$$

Δk is the detuning parameter; $c\beta_{||0}$ is the initial axial velocity; γ_0 is the initial energy and θ_{j0} is the initial phase of the j th electron. It follows that, at $z = 0$, $\delta\gamma_j = \delta\theta_j = 0$.

With the injected beam unbunched, the zero'th average vanishes,

$$\langle e^{-i(\theta_0 + \Delta kz)} \rangle = 0, \quad (12)$$

and the linearized equations are

$$\frac{d\delta\gamma_j}{dz} = \frac{iC\beta_{\perp 0}}{2\beta_{||0}} a e^{i(\theta_{j0} + \Delta kz)} - \eta_{||} \langle \delta\theta e^{-i(\theta_0 + \Delta kz)} \rangle e^{i(\theta_{j0} + \Delta kz)} + c.c., \quad (13)$$

$$\frac{d\delta\theta_j}{dz} = \frac{\omega}{c\beta_{||0}^2} \frac{\partial\beta_{||0}}{\partial\gamma} \delta\gamma_j, \quad (14)$$

$$\frac{da}{dz} = \frac{\eta\beta_{\perp 0}}{\beta_{||0}} \langle \delta\theta e^{-i(\theta_0 + \Delta kz)} \rangle. \quad (15)$$

Exponential forms for the perturbations are then assumed.

$$\delta\gamma_j = \sum_j \bar{\delta\gamma}_j e^{i(\theta_{j0} + \Delta k z + \alpha_j z)} + c.c., \quad (16)$$

$$\delta\theta_j = \sum_j \bar{\delta\theta}_j e^{i(\theta_{j0} + \Delta k z + \alpha_j z)} + c.c., \quad (17)$$

$$a = \sum_j \bar{a}_j e^{i\alpha_j z}, \quad (18)$$

Substituting the perturbations in Eqs. (16)-(18) into Eqs. (13)-(15) yields the dispersion relation

$$\alpha_j^3 + 2\Delta k \alpha_j^2 + (\Delta k^2 - \frac{\omega}{c\beta_{||0}^2} \frac{\partial \beta_{||0}}{\partial \gamma} \eta_{||}) \alpha_j + \frac{C^2 \beta_{\perp 0}^2 \omega I}{4c\beta_{||0}^4 I_A} \frac{\partial \beta_{||0}}{\partial \gamma} = 0 \quad (19)$$

For peak gain in the Raman regime, $\Delta k \gg \alpha_j$; therefore the α^3 term in the dispersion relation can be ignored.

We now turn our attention to the section to the right of the mesh ($z > z^*$), the section that starts with a prebunched beam. The co-ordinate system is redefined as $z' = z - z^*$, z^* being the location of the mesh. As before the linearization proceeds by defining

$$\gamma'_j = \gamma_0 + \delta\gamma'_j, \quad (20)$$

$$\theta'_j = \theta'_{j0} + \Delta k z' + \delta\theta'_j, \quad (21)$$

where $\theta'_{j0} = \theta_{j0} + \Delta k z^*$. Δk , γ_0 , and θ_{j0} are defined to be the same quantities used earlier when the prebunching section is considered. γ_0 and θ'_{j0} here are

not the energy and phase of the j th electron at $z' = 0$. Instead they are the energy and phase of the j th electron there if no FEL interaction (i. e. prebunching) has taken place in the section to the left of the mesh. Therefore γ_0 and θ'_{j0} do not contain any information about prebunching. Instead the crucial information is contained in the $\delta\gamma'_j$ and $\delta\theta'_j$ terms at $z' = 0$. Here, $\delta\gamma'_j \neq 0$ and $\delta\theta'_j \neq 0$ at $z' = 0$, in contrast to $\delta\gamma_j = \delta\theta_j = 0$ at $z = 0$.

The perturbations are defined to have exactly the same forms as those in Eqs. (16)-(18),

$$\delta\gamma'_j = \sum_s \overline{\delta\gamma'_s} e^{i(\theta'_{j0} + \Delta k z' + \alpha'_s z')} + \text{c.c.}, \quad (22)$$

$$\delta\theta'_j = \sum_s \overline{\delta\theta'_s} e^{i(\theta'_{j0} + \Delta k z' + \alpha'_s z')} + \text{c.c.}, \quad (23)$$

$$a' = \sum_s \overline{a'_s} e^{i\alpha'_s z'}. \quad (24)$$

Since θ'_{j0} does not contain any information about prebunching, the zero'th average again vanishes,

$$\langle e^{-i(\theta'_0 + \Delta k z')} \rangle = \langle e^{-i[(\theta_0 + \Delta k z^*) + \Delta k(z - z^*)]} \rangle = \langle e^{-i(\theta_0 + \Delta k z)} \rangle = 0. \quad (25)$$

As a result, the linearized equations of motion are the same as those in Eqs. (13)-(15) with the unprimed variables turned into primed variables. The constants, Δk , $\beta_{\perp 0}$, and $\beta_{\parallel 0}$, are the same in both sets of equations. With

the further assumption that the mesh is totally transparent to the electron beam, parameters $\eta_{||}$ and η also remain unchanged. Having the same set of equations of motion with identical perturbation forms assumed as before leads one to conclude that the dispersion relation in Eq. (19) also holds in this section. In another words $\alpha_s = \alpha'_s$. The field growth rates α_s of the individual modes are the same in both sections independent of whether the beam is prebunched or not. What does change are the initial relative amplitudes associated with each of the modes. It will be shown later in the paper how this statement is consistent with the overall increase in the radiation growth rate.

The tungsten mesh attenuates the field by a factor of A and leaves γ_j and θ_j unchanged. In the experiments $A = 10$. By equaling the field and particle variables just to the left and to the right of the mesh, one finds

$$\sum_j \bar{a}'_s = \frac{\sum_s \bar{a}_s e^{i\alpha_s z^*}}{A}, \quad (26)$$

$$\sum_j \bar{\delta\gamma}'_s = \sum_j \bar{\delta\gamma}_s e^{i\alpha_s z^*}, \quad (27)$$

$$\sum_j \bar{\delta\theta}'_s = \sum_j \bar{\delta\theta}_s e^{i\alpha_s z^*}. \quad (28)$$

$\bar{\delta\gamma}_s$ and $\bar{\delta\theta}_s$ can be expressed in terms of \bar{a}_s , likewise $\bar{\delta\gamma}'_s$ and $\bar{\delta\theta}'_s$ can be expressed in terms of \bar{a}'_s . \bar{a}'_s can then be solved in terms of \bar{a}_s .

For an free-electron laser operating at peak gain in the Raman regime, s runs from 1 to 2, corresponding to the two complex conjugate waves. Eqs. (26)-(28) reduce to

$$\sum_{s=1}^2 \bar{a}'_s = \frac{\sum_{s=1}^2 \bar{a}_s e^{i\alpha_s z^*}}{A}, \quad (29)$$

$$\sum_{s=1}^2 \frac{\bar{a}'_s}{\alpha_s} = \sum_{s=1}^2 \frac{\bar{a}_s e^{i\alpha_s z^*}}{\alpha_s}, \quad (30)$$

with $\alpha_1 = iQ$ and $\alpha_2 = -iQ$ where Q is real and positive.

In the section to the left of the mesh ($z < z^*$), the field can be written as

$$a = a_0 \cosh Qz, \quad (31)$$

or in another form,

$$a = \frac{a_0}{2} (e^{Qz} + e^{-Qz}). \quad (32)$$

Solving Eq. (29) and Eq. (30) for \bar{a}'_s gives the field to the right of the mesh ($z > z^*$),

$$a' = a_0 \left(\frac{\cosh Qz^* \cosh Qz'}{A} + \sinh Qz^* \sinh Qz' \right), \quad (33)$$

or in another form,

$$a' = \frac{a_0}{2} \left\{ \left[\frac{1}{2} \left(\frac{1}{A} + 1 \right) + \frac{1}{2} \left(\frac{1}{A} - 1 \right) e^{-2Qz^*} \right] e^{Qz} + \left[\frac{1}{2} \left(\frac{1}{A} - 1 \right) e^{2Qz^*} + \frac{1}{2} \left(\frac{1}{A} + 1 \right) \right] e^{-Qz} \right\}. \quad (34)$$

As illustrated in Eq. (32), the field starts out with equal amplitudes in both the growing and decaying modes in the prebunching section. After the radiation passes through the mesh, the relative amplitudes between the two modes shift as illustrated in Eq. (34) while the growth rates in respective modes remain unchanged. It can easily be proved that the overall field amplitude growth rate

$$\frac{1}{a'} \frac{da'}{dz} > \frac{1}{a} \frac{da}{dz} \quad \text{for all } z \quad (35)$$

as long as $A > 1$. This increase in the overall field growth rate is therefore accounted for not by the increase in the growth rates in individual modes but by the shifting of the relative amplitudes between them. On the other hand it can also be shown that $a' < a$. In fact

$$\frac{a'}{a} \leq \frac{1}{2} \left(\frac{1}{A} + 1 \right) \quad \text{for all } z. \quad (36)$$

In conclusion even the dramatic increase in the overall radiation growth rate cannot compensate for the mesh attenuation, and there is always an reduction in overall gain G when this prebunching scheme is employed. Fig. 8 shows the excellent match between analytic results and simulations.

The case for an free-electron laser operating at peak gain in the collective Raman regime is considered above, but the theory can also be applied

to parameter regions besides peak gain and to the single particle Compton regime. Phase shift caused by the mesh or introduced externally can also be taken into account by letting A be complex,

$$A = |A|e^{i\Delta\theta}, \quad \text{where } \Delta\theta \text{ is the phase shift.} \quad (37)$$

5 DISCUSSION

We have reported on the effects of prebunching in a Raman free-electron laser amplifier, and observed large enhancements in the single pass growth rates Γ . Most of the observations were made using RF drivers that operate either CW or with microsecond long pulses. To verify that the measurements of Γ indeed represent single pass gain and are not marred by reflections (due to the presence of the mesh, for example) we also carried out a series of measurements in which the pulse length (~ 5 ns) of the RF input was shorter than the round-trip pass through the system.

To the left of the mesh ($z < z^*$), the system behaves as one would expect from a conventional FEL operating in the Raman regime. Thus, when the wiggler field strength B_w is increased from 66 to 188 G (Fig. 2), the growth rate $\Gamma(z < z^*)$ increased from 2.4 to ~ 6.9 dB/m, which shows that $\Gamma(z <$

$z^*) \propto B_w$, in agreement with expectations. Also $\Gamma(z < z^*)$ is found to be independent of the input power P_{in} (Fig. 4) for sufficiently low input powers, such that nonlinear phenomena are unimportant. This is in agreement with conventional FEL theory.

To the right of the mesh ($z > z^*$) the situation is different. When B_w is increased from 66 to 188 G (a factor of 2.9), $\Gamma(z > z^*)$ increases from 6.3 to 32 dB/m (a factor of 5.1). However, it is noteworthy that the overall gain G of the system is less than what it would have been in the absence of the mesh (i. e. prebunching). Thus, our experimental configuration is useful primarily not to increase gain, but to suppress parasitic oscillations as is common practice in traveling wave tube (TWT) amplifiers [3].

The experimental observations reported in this paper are fully substantiated by computer simulations and analytic studies. Although we have treated only the cold electron beam case analytically, it can be extended to warm beams and the single particle (Compton) regime.

6 ACKNOWLEDGMENTS

This work was supported by the National Science Foundation, the U. S. Air Force Office of Scientific Research, and the U. S. Department of Energy, Division of Nuclear and High Energy Physics.

References

- [1] R. Coisson, "Optical klystrons," in *Particle Accelerators*. New York, NY: Gordon and Breach, 1981, vol. II, pp. 245-253, and references therein.
- M. Billardon, P. Elleaume, Y. Lapierre, J.M. Ortega, C. Bazin, M. Bergher, J. Marilleau, and Y. Petrov, "The Orsay storage ring free electron laser: New results," in *Proc. 7th Int. Conf. Free Electron Lasers*, E.T. Scharlemann and D. Prosnitz, Eds. Amsterdam, The Netherlands: North Holland, 1986, pp. 26-34.
- G. Vignola, R.R. Freeman, B.M. Kincaid, C. Pellegrini, A. Luccio, J. Murphy, J. Galayda, and A. Van Steenbergen, "A new method for pumping an optical klystron," *Nucl. Instrument. Methods Phys. Res.*, vol. A239, pp. 43-46, 1985.
- [2] C. Leibovitch, K. Xu, and G. Bekefi, *IEEE J. Quantum Electr.* 24, 1825 (1988).
- [3] J.R. Pierce, *Traveling Wave Tubes*. Princeton, NJ: Van Nostrand, 1950, ch. IX, pp. 131-144; S.Y. Liao, *Microwave Devices and Circuits*. Englewood Cliffs, NJ: Prentice-Hall, 1985, pp. 220-224.

J. Fajans and J.S. Wurtele, IEEE J. Quantum Electr. 24, 1805 (1988).

- [4] J.S. Wurtele, J. Fajans, and R. Chu, "Theory and Experiment of Collective Free Electron Lasers," paper in preparation.

FIGURE CAPTIONS

Fig. 1. Schematic of the experimental setup.

Fig. 2. RF power output as a function of interaction length, for two different wiggler field amplitudes B_w ; RF power input 3 W; RF frequency 10.5 GHz; electron beam energy 170 keV; electron beam current ~ 1 A; axial guide magnetic field $B_{||} = 1.63$ kG.

Fig. 3. RF power output as a function of interaction length for three different values of RF input power. RF frequency 9.3 GHz; electron beam energy 130 keV; electron beam current ~ 1 A; wiggler field strength 188 G; axial guide field $B_{||} = 1.63$ kG.

Fig. 4. Typical oscilloscope traces showing (a) the beam voltage, (b) the output microwave power when the electron beam is terminated before the mesh ($z < z^*$) and (c) when it is terminated after the mesh ($z > z^*$).

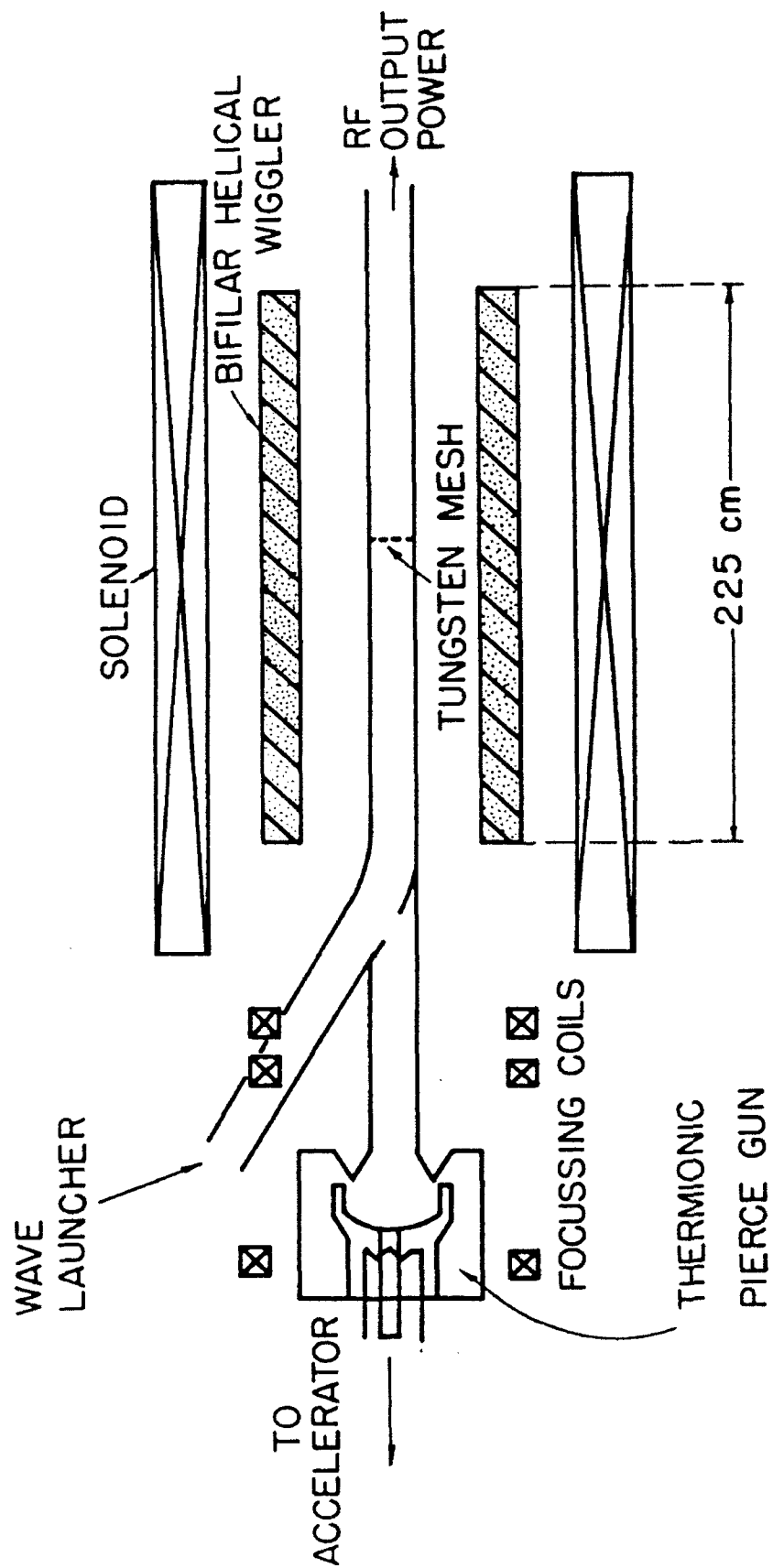
Fig. 5. Computer simulations of the experimental results shown in Fig. 2.

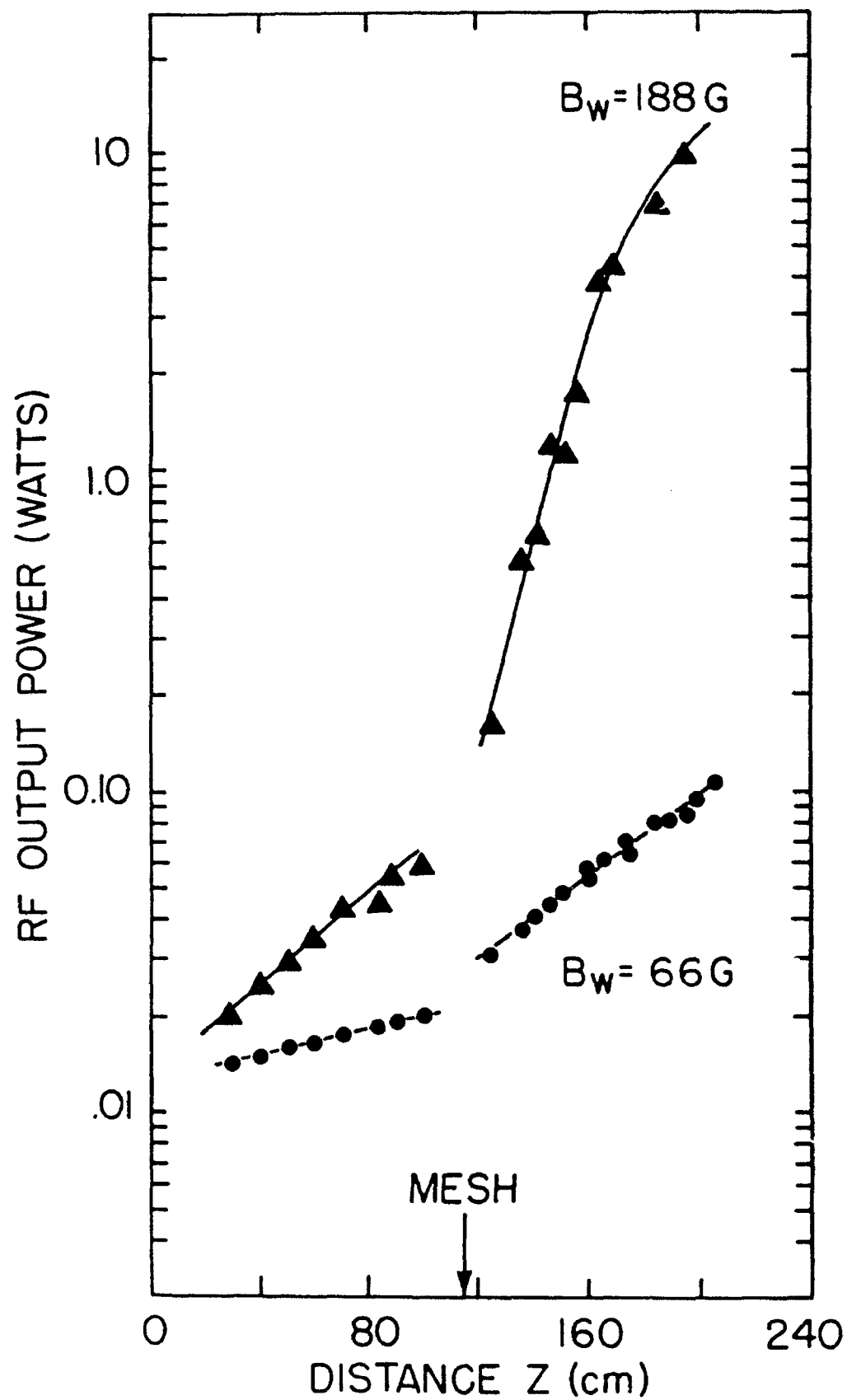
Fig. 6. Computer simulations of the experimental results shown in Fig. 3a.

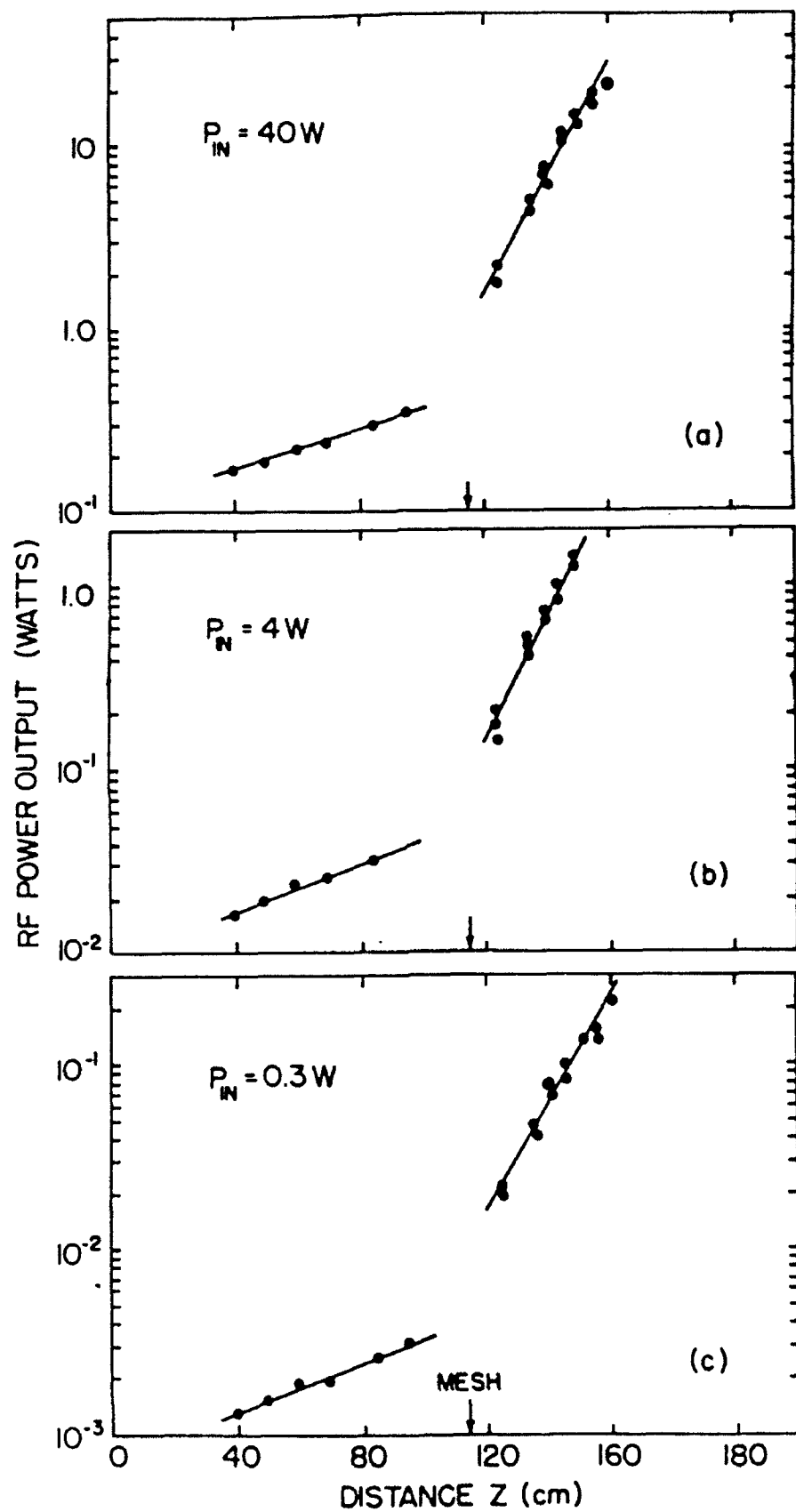
Fig. 7. Computer simulations of the experimental results shown in Figs. 4b,c. Note that in making the comparison, the electron beam energy

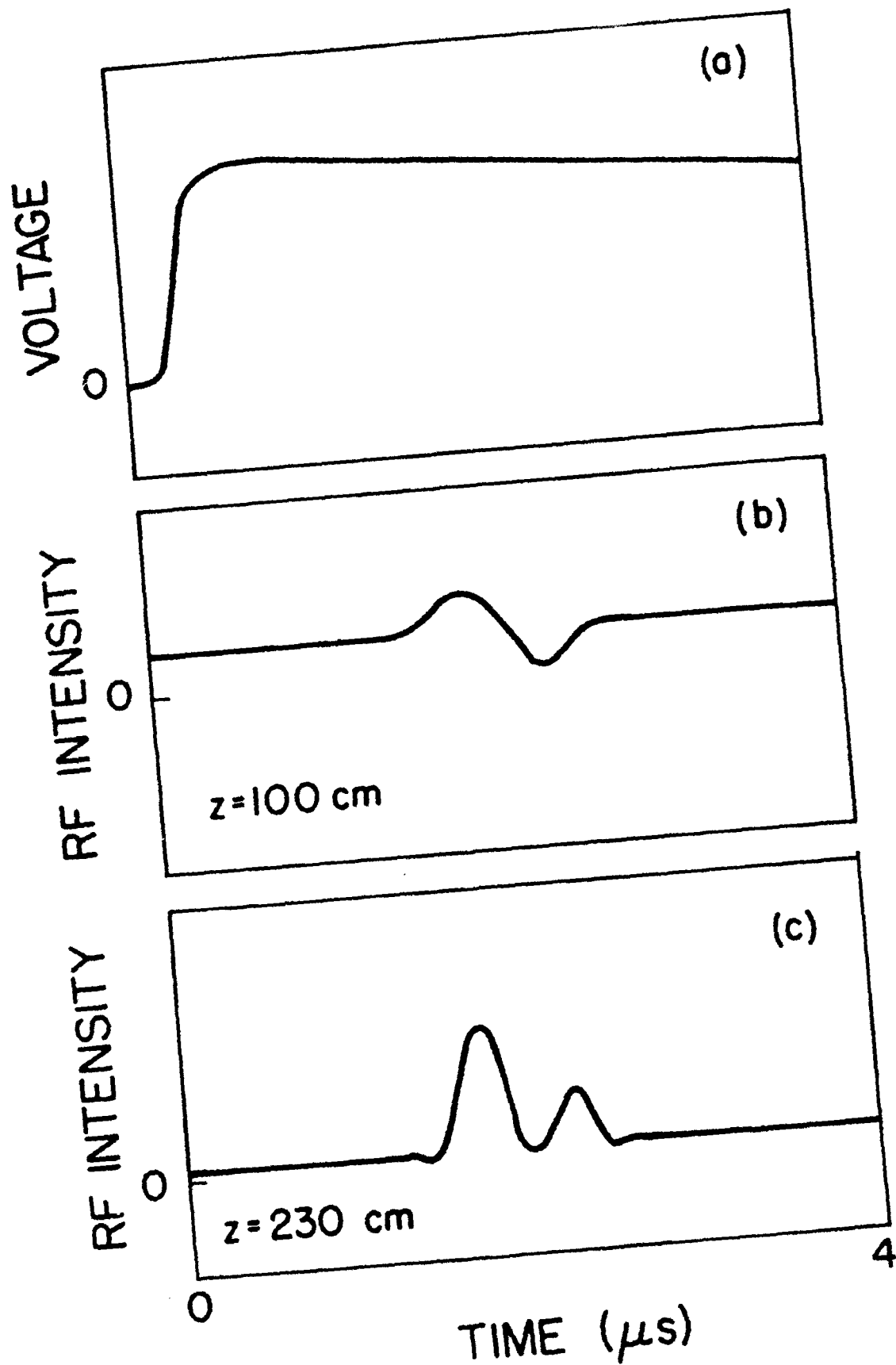
in Fig. 4 decreases from left to right, which is opposite to the plot shown here.

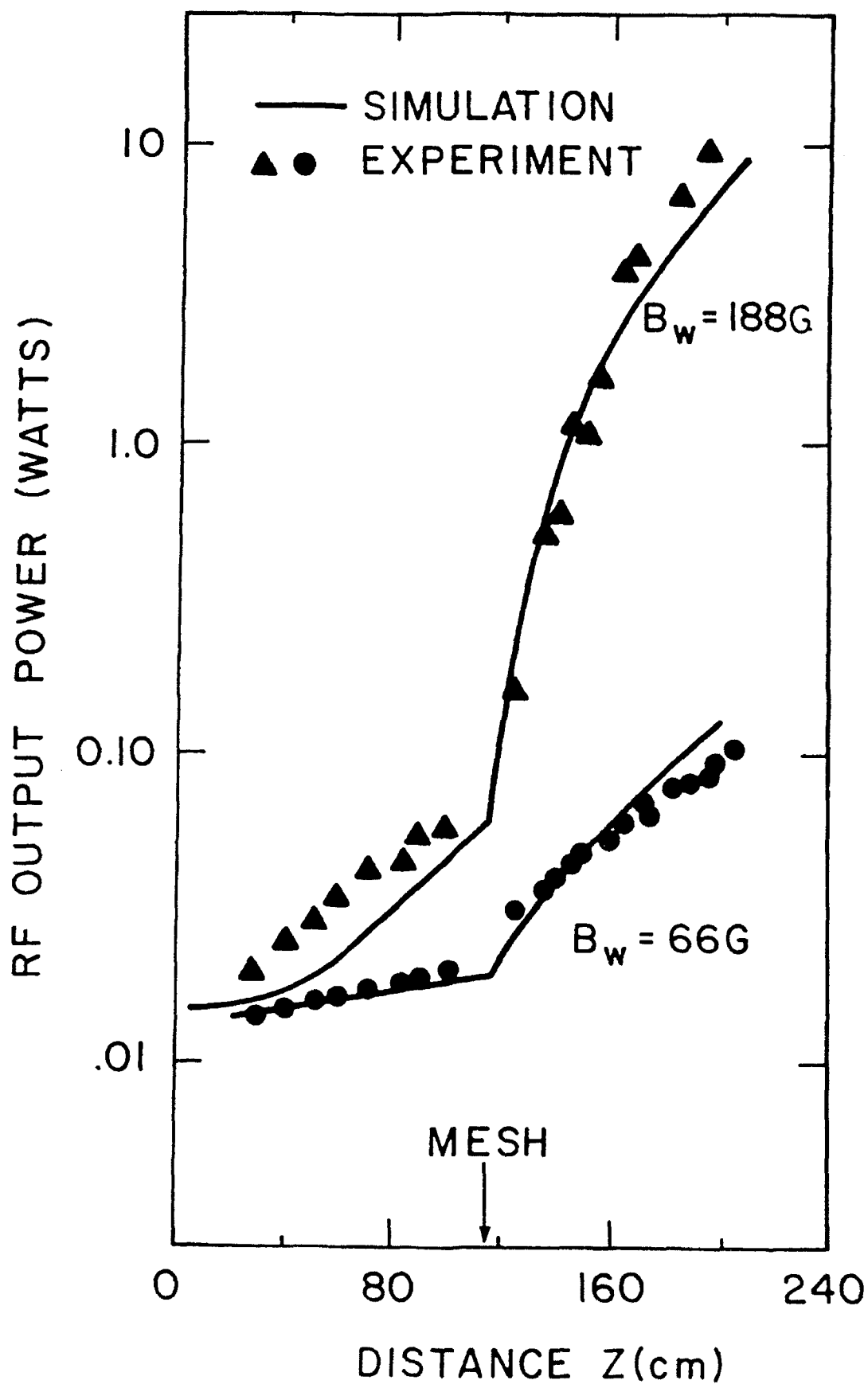
Fig. 8. Comparsion between simulations and analytic results.











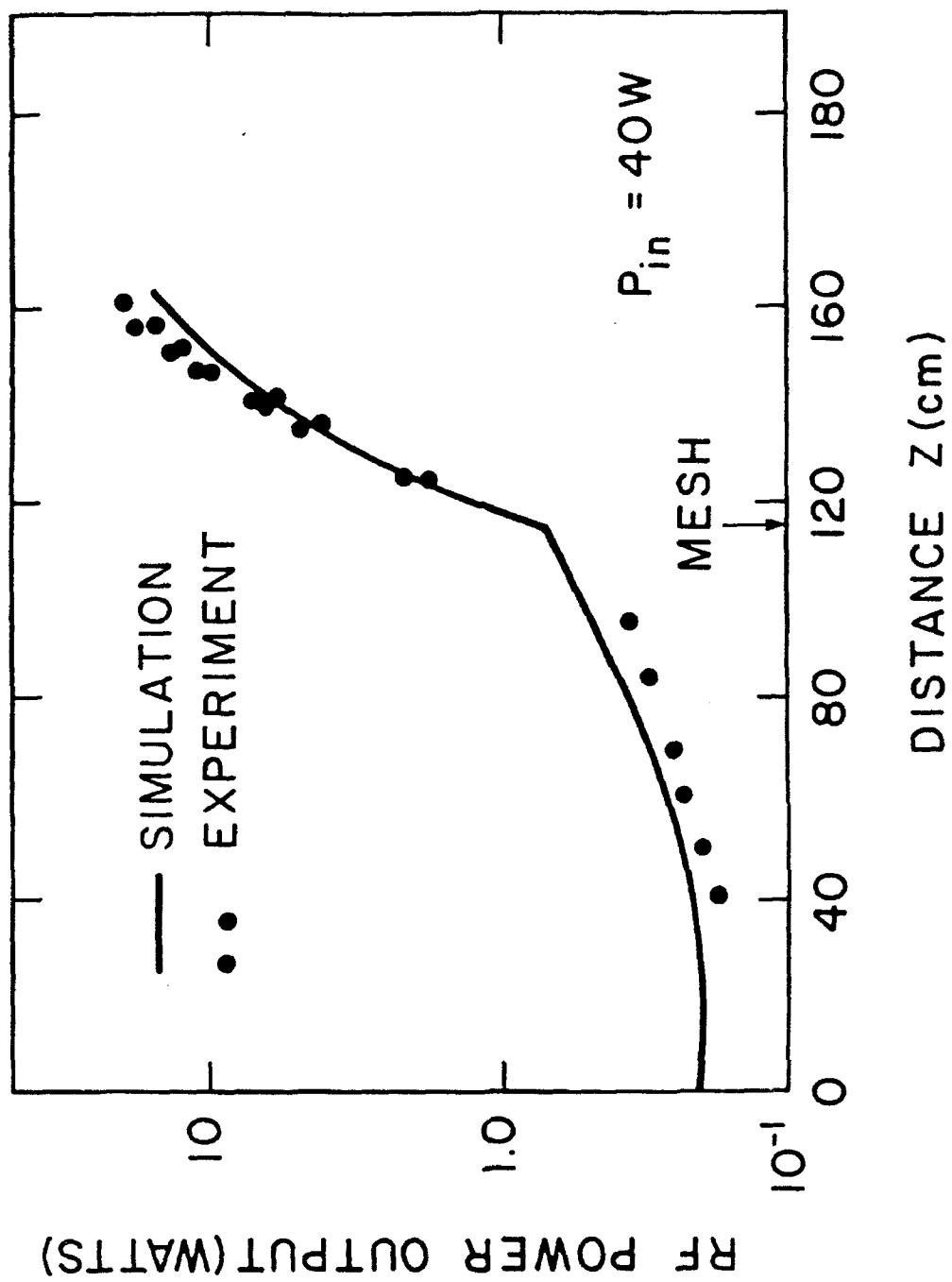
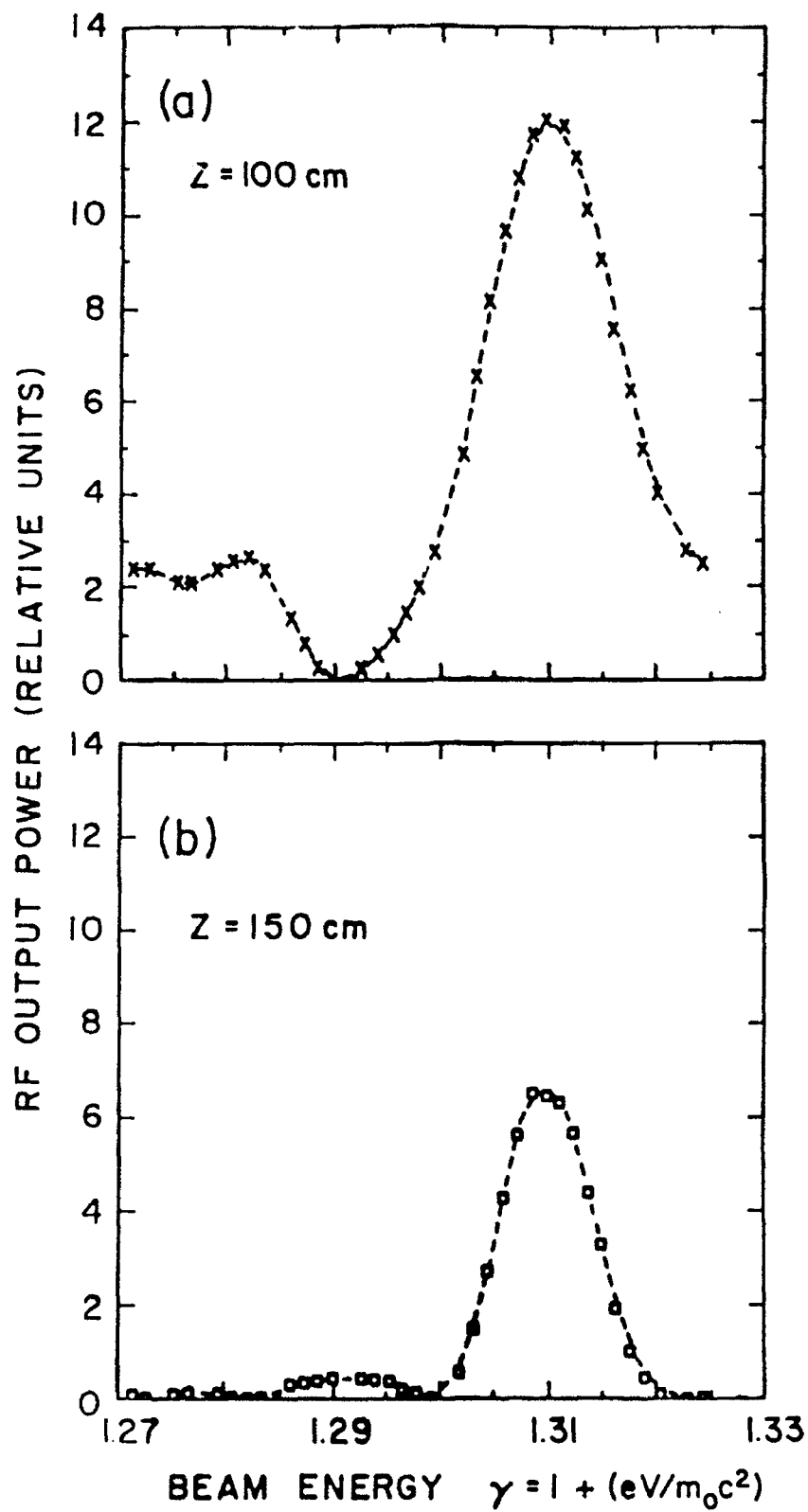


Fig.6 Wurtele,Bekefi,Chu,Xu



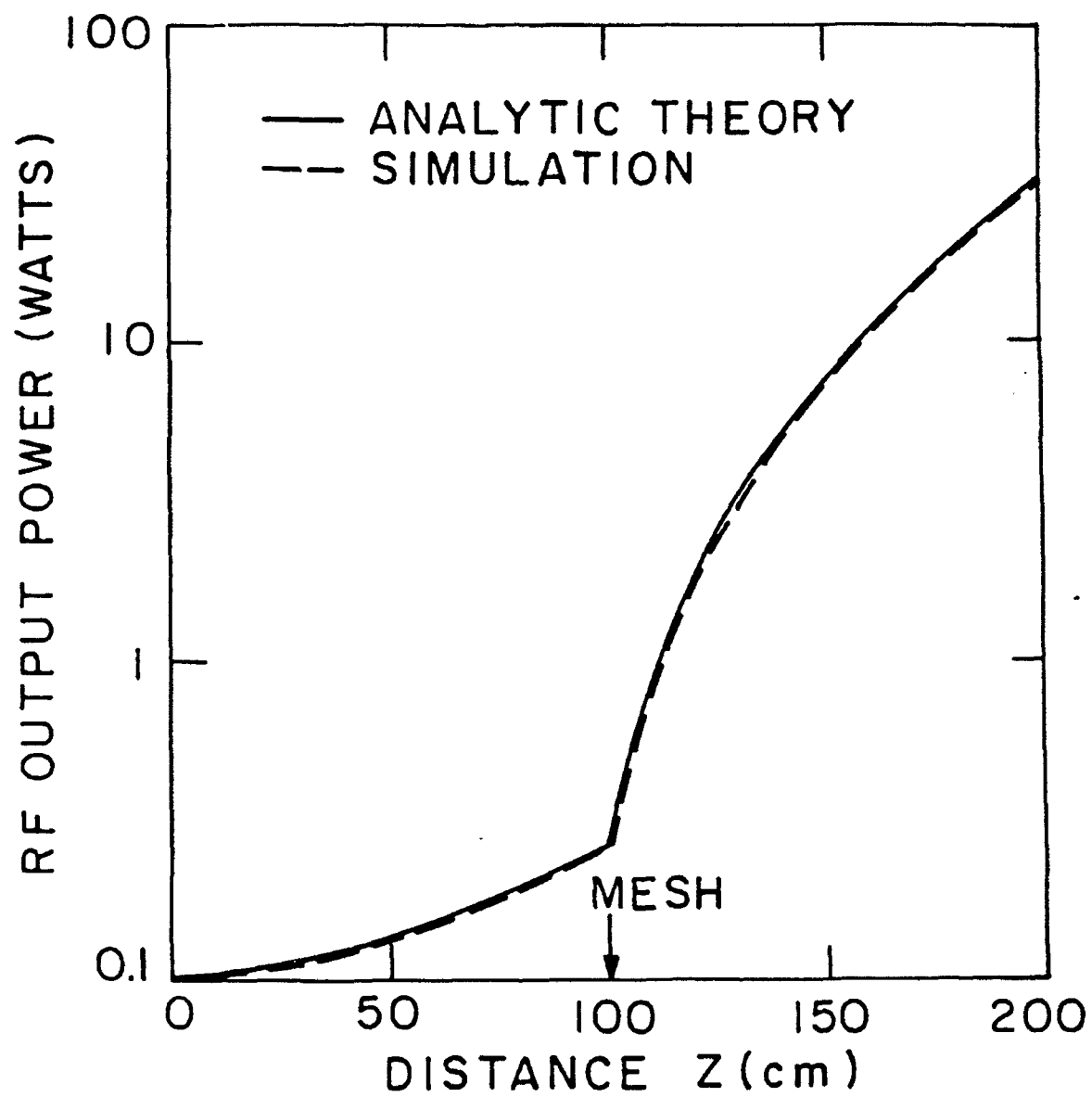


Fig.8 Wurtele, Bekefi, Chu, Xu

APPENDIX 2

OBSERVATIONS OF FIELD PROFILE MODIFICATIONS IN A RAMAN FREE ELECTRON LASER AMPLIFIER

K. Xu[†], G. Bekefi, and C. Leibovitch[‡]

Department of Physics and Research Laboratory of Electronics
Massachusetts Institute of Technology
Cambridge, Massachusetts 02139

ABSTRACT

We report measurements of the spatial distribution of the RF electric field intensities and phases induced in a free electron laser (FEL) amplifier operating in the collective (Raman) regime. The studies are carried out at a microwave frequency of ~ 10 GHz in a FEL using a mildly relativistic electron beam of ~ 200 keV energy and 1 - 4 A current. The probing of the ponderomotive (space charge) and the electromagnetic waves is accomplished by means of small movable electric dipole antennas inserted into the interaction region.

[†] permanent address: University of Electronic Science and Technology of China, Chengdu, China.

[‡] permanent address: Applied Physics Department, Scientific Division, Rafael Laboratory, Haifa 31021, Israel.

1. INTRODUCTION

Free electron laser (FEL) amplification is the consequence of a resonant interaction [1] between an incident electromagnetic wave and a co-propagating electron beam that has been injected into a periodic "wiggler" magnetic field. This can lead to high output gain, and high efficiency of converting electron beam kinetic energy into radiation. Remarkably, it also leads to large phase shifts [2]-[4] in the amplified electromagnetic wave. Under proper circumstances this phase shift can have a sign such that the electromagnetic wave is refracted towards the axis of the electron beam in a manner somewhat akin to the guiding properties of an optical fiber. Such "optical guiding" [5]-[10] would mitigate the effects of diffraction, and thereby allow the length of FEL wigglers to exceed the Rayleigh range. Long wigglers are needed if free electron lasers are to operate either in the vacuum-ultraviolet or at high efficiencies in the infrared wavelength regime.

It comes as no surprise that strong FEL activity as described above should be accompanied by significant modification of the spatial distribution of the RF fields within and in the immediate vicinity of the electron beam. To be sure, one way of confirming optical guiding is by observation of the changes in the transverse spatial profile of the copropagating amplified wave. Such field probing can be quite difficult at short wavelengths (infrared and visible). However, the microwave regime, in which our experiments are conducted, offers a relatively simple and direct way. We allow small, movable electric dipole antennas to traverse the waveguide in which the interaction takes place. Using antennas sensitive to different polarizations, we are then able to distinguish between wave types.

There are two major wave types in the vicinity of the bunched electron beam to which our electric dipoles respond. First, there are the electromagnetic (solenoidal) fields associated with the growing electromagnetic wave of frequency ω and axial wavenumber $k_{||}$, propagating with a velocity $v_n = (\omega/k_{||}) \geq c$. And then there are the irrotational, quasi-electrostatic fields of the bunched electron beam propagating with a phase velocity $\omega/(k_{||} + k_w)$ approximately equal to the electron beam velocity $v_b < c$ ($k_w = 2\pi/l_w$ is the wiggler wave number). In the case of tenuous, highly relativistic beams used in short wavelength FELs, the contribution of the space charge electric field to the overall field

profile is usually very small. However, in the microwave regime where often high current, mildly relativistic beams are employed, the contribution from the space charge electric field may no longer be negligible, as will be demonstrated in the experiments described below.

In section 2 of this paper we describe the experimental arrangement. In section 3 we present field profile measurements (in amplitude and phase) associated with the space charge wave. In section 4 we give profiles associated primarily (but not entirely) with the electromagnetic wave. The observations will be discussed in section 5.

2. EXPERIMENTAL SET UP

Figure 1 shows a schematic of our experiment. The accelerating potential is supplied by a Marx generator (Physics International Pulserad 615MR) which has a maximum capability of 500kV and 4kA. Since this accelerator does not use a pulse-forming network, the output voltage pulse is essentially that of a discharging capacitor bank with a shunt adjusted RC time constant of 10 – 100 μ sec. The electron beam is generated by a thermionically emitting, electrostatically focused, Pierce-type electron gun (250 kV, 250 A) from a SLAC klystron (model 343). An assembly of focusing coils transports the electron beam into the drift tube. To insure good electron orbits, an aperture acting as an emittance selector is inserted which limits the electron beam radius to $r_b = 0.245$ cm so that only the inner portion of the beam is used. With this precaution, the energy spread of the beam entering the magnetic wiggler is $\Delta\gamma_{||}/\gamma_{||} \leq 0.003$ ($\gamma_{||} = [1 - v_{||}^2/c^2]^{-1/2}$).

The gun focusing coils guide the electron beam into a rectangular (1.01 cm \times 2.29 cm) stainless steel evacuated drift tube which is also the waveguide for the electromagnetic radiation. The beam is contained by an uniform axial magnetic field $B_{||}$ that has a power supply limited maximum of 7 kG and a minimum of approximately 800 G. Below this value, beam defocusing and deterioration occur. The net beam current entering the magnetic wiggler is in the range of 1-5 A. The 65 period wiggler magnet has a period $l_w = 3.5$ cm, a maximum amplitude $B_w = 1.0$ kG, and is generated by bifilar conductors. Since the beam aperture limits the size of the beam to $r_b/l_w \approx 0.07$, the wiggler field is close to that of an ideal wiggler. That is, the effects of the radial variation of the wiggler field

and the presence of the off-axis components are usually small. At the wiggler entrance a slowly increasing field amplitude is produced by resistively loading the first six periods of the wiggler magnet [11].

The 2.7 m long drift tube acts as a rectangular waveguide whose fundamental TE_{10} mode has a cutoff frequency of $\omega_c/2\pi = 6.6$ GHz. Microwaves are launched onto the electron beam by a waveguide coupler (see Fig. 1). All our measurements are carried out at frequencies between 9 and 11 GHz. At these frequencies the empty waveguide can support only the fundamental (TE_{10}) mode, all higher modes being evanescent. The monochromatic radiation injected into the system is provided by a low power variable frequency source and amplified by means of a traveling wave tube amplifier. Typical power inputs into the FEL are in the 1 - 10 W range. At the output end of the wiggler, a mica window transmits the linearly polarized radiation generated in the drift tube, where it is measured by means of standard calibrated crystal detectors.

The transverse profile of the RF fields is studied by means of three small electric dipole antennas inserted into the waveguide as is illustrated in Figs. 1(b), (c). Two of the antennas, inserted through stainless steel bellows, are movable along the x axis, and their positions are precision controlled by micrometer screws. The third, reference antenna is fixed and protrudes slightly into the waveguide wall as is seen in Figs. 1(b), (c). Each probe has a length of 0.1 cm; cold tests show that the probes can detect RF intensity variations as small as 1% over distances of ≈ 0.05 cm. The signal from each probe is attenuated by a variable attenuator, then measured by a calibrated crystal detector. The outputs from the crystal rectifiers are then displayed on fast oscilloscopes. We note that all three antennas are roughly in the middle of the wiggler region and in exactly the same transverse plane, $z \approx 115$ cm from the upstream end of the wiggler.

The left hand movable antenna designated in Figs. 1(b), (c) by $I_y(EM)$ probes the y component of the RF electric field intensity, as does the reference probe $I_y(REF)$. Cold test carried out in the absence of the FEL interaction show that the $I_y(EM)$ probe accurately maps out the TE_{10} waveguide mode whose electric field amplitude is shown schematically in Fig. 1(b), and is given by the familiar expression, $E_y(x, t) = E_{0y} \cos(\pi x/a) \cos(\omega t - k_{||} z)$, $-a/2 \leq x \leq a/2$ where $a = 2.29$ cm equals the length of the wide dimension of the

waveguide. Therefore the probe designated $I_y(\text{EM})$ maps out primarily the RF profile associated with the electromagnetic wave launched into the interaction region. The fixed reference probe $I_y(\text{REF})$ likewise measures primarily the electromagnetic field intensity of the launched, amplified wave.

The right hand movable antenna, designated $I_x(\text{SC})$, is sensitive to the x component of any RF electric field. Cold tests indicate that because of slight misalignment, a small signal due to E_y is nonetheless present on this probe. However, this intensity is more than 25 dB below the intensity of the y component and thus causes no problems in the measurements described below.

During FEL activity, the presence of x -directed electric fields is due mainly to the quasi-electrostatic, irrotational fields of the bunched electrons, whose spatial distribution is illustrated schematically in Fig. 1(c). Higher order waveguide modes with electric field components in the x direction could also be present during FEL activity, but calculations show [12] that their expected amplitudes are very small compared with the space charge fields.

In addition to intensity profiles, we have also measured the profiles of the RF phase. This is accomplished by standard interferometric techniques [2]-[4] in which the antenna signal is mixed in a "magic tee" with a reference signal from the TWT launcher.

Typical oscilloscope traces of the intensity and phase are illustrated in Fig. 2. The FEL is fired by the discharging of the Marx accelerator. Because of an RC droop, the beam energy falls gradually as is illustrated in Fig. 2(a). Amplification [Fig. 2(b)], as measured by the y -oriented reference probe $I_y(\text{REF})$ occurs at a beam energy for which the slow (negative energy) space-charge wave on the beam is near phase synchronism with the electromagnetic wave. This results in the gain peak. The gain is ~ 3 dB. Later in time, at a lower beam energy, one observes a dip corresponding to wave absorption. Here the wave energy is converted to electron kinetic energy, as is known to occur when the fast (positive energy) space-charge wave is in synchronism with the electromagnetic wave.

The resonance relationship between the guided electromagnetic wave and the wave on the beam is given by the well known expressions

$$\omega^2 = c^2 k_{\parallel}^2 + \omega_c^2 \quad (1)$$

and

$$\omega = (k_{||} + k_w)\beta_{||}c \pm p_1\omega_p\phi^{1/2}/\gamma_{||}\gamma^{1/2}, \quad (2)$$

where the plus sign corresponds to the fast, positive energy, "passive" space charge wave, and the minus sign corresponds to the slow, negative energy, "active" space charge wave; $\omega_c^2 = \omega_{c0}^2 + p_2\omega_p^2/\gamma$ is the effective waveguide cutoff frequency adjusted for the presence of the electron beam; ω_{c0} is the empty waveguide cutoff frequency [(in our case the lowest mode of a rectangular waveguide (TE₁₀))]; $k_w = 2\pi/l_w$ is the wiggler wavenumber; $\beta_{||} = v_{||}/c$ is the normalized axial velocity of the electron beam, and $\omega_p = (Ne^2/m_0\epsilon_0)^{1/2}$ is the nonrelativistic plasma frequency. The relativistic mass increase $\gamma = 1 + eV/m_0c^2$ measures the beam energy; ϕ is the adjustment [13] to the plasma frequency due to the combined wiggler and axial magnetic fields; p_1 is the reduction in the plasma frequency that results from finite radial effects, and p_2 is the electromagnetic wave energy weighted ratio of the electron beam cross-section and the waveguide area. In normal operation of our FEL, $p_2 \approx 0.06$ so that $\omega_c \approx \omega_{c0}$, $p_1 \approx 0.5$, and $\phi \approx 1$.

Fig. 2(c) shows the corresponding oscilloscope trace as observed with the space charge probe $I_x(\text{SC})$. As expected, it shows maximum activity at times when the electromagnetic wave interacts either with the slow or fast space charge waves.

Fig. 2(d) shows the temporal behavior of the RF phase of the electromagnetic wave. It is noteworthy that maximum phase change occurs at a time when the gain is close to zero, as is characteristic of FELs operating in the collective (Raman) regime [2].

In order to check the validity of these results, we dump the electron beam into the waveguide walls by means of a magnetic kicker placed 18 cm upstream of the probes. This allows the FEL-induced profile modification of the RF field to convert down to the fundamental TE₁₀ mode, and null signals result (the higher modes excited by the FEL interaction are evanescent and die out exponentially within 1 or 2 waveguide wavelengths from the kicker position).

The experiments described below are carried out on electron beams with energy ranging from 150-170 keV and a current of ~ 1 A. The axial guide magnetic field is held constant

at 1580 G. The wiggler field amplitude is set at one of two values, 130 G and 200 G. The RF input signal has a frequency of 9.7 GHz and a power level of 3 W. With these parameters, the FEL operates in the linear regime and has a single pass gain of ~ 3 dB at the axial position $z \approx 115$ cm from the beginning of the wiggler, where the antennas are located.

3. SPACE-CHARGE FIELD PROFILES

The spatial distribution of the DC current density $J_z(x, y)$ of the electron beam is determined by using the space charge dipole antenna (designated $I_x(SC)$ in Fig. 1) as a current monitor. This is accomplished by terminating the coaxial cable from the antenna with a 50 Ohm load and measuring the voltage across it. Figure 3(a) illustrates the current density profile $J_z(x, 0)$ as a function of displacement of the antenna in the x direction. We see that the full width of the distribution at half maximum is ~ 5 mm, and equals the diameter of the emittance selector placed upstream from the wiggler. Figure 3(b) shows the current density distribution $J_z(0, y)$ as a function of displacement in the y direction. This measurement is carried out by holding the antenna position fixed at $x = 0, y = 0$ and moving the entire waveguide in the y direction relative to the stationary electron beam. This determination is of course less accurate because of the considerable loss of symmetry caused by the waveguide displacement relative to the beam. The above measurements of the beam size and beam center are needed in understanding the subsequent RF intensity profiles.

To use the space-charge probe $I_x(SC)$ for the measurement of the RF fields, the DC beam current is shunted to ground, the RF field is rectified by a crystal diode and then displayed on a fast oscilloscope. Figure 4(a) illustrates how the electric field intensity $I_x(x, 0)$ of the space charge wave varies as a function of the probe displacement in the x direction. We see that $I_x(x, 0)$ is zero at the center of the electron beam, is maximum near the beam edge $x = r_b$ and falls off rapidly when $|x| > r_b$, in agreement with the expected behavior of the irrotational fields produced by the bunched electron beam. Figure 4(b) shows the variation in $I_x(0, y)$ as the antenna traverses the beam center in the y direction; and $I_x(r_b, y)$ gives the intensity variation as it traverses the beam edge. The small cartoons in the upper right hand corner illustrate schematically the motions of the space charge

probe. We note that these fields exist only during FEL activity, and become immeasurably small when, for example, the wiggler field is turned off or when the resonance conditions (1) and (2) are not fulfilled.

Combining data like that illustrated in Figure 4, one can generate a two-dimensional plot of the space charge field intensity profile. This is shown in Figure 5.

Since the space charge electric field points radially outwards from the electron beam center, it must undergo a 180° phase change in traversing the center. This effect is illustrated in Figure 6. Figure 6(a) shows a plot of the phase of the space charge wave as a function of time during the falling voltage pulse for two discrete positions of the antenna on opposite sides of the centre $x = \pm 4$ mm. Figure 6(b) gives the phase as a function of the antenna displacement in the x direction at a time during the pulse when the phase change is maximum (and the gain is near zero). It shows clearly the abrupt phase change when the beam center is crossed. This correct phase behavior also lends strong support to the validity of the observations of Figs. 2, 4 and 5, when the antennas are used in intensity measurements.

4. ELECTROMAGNETIC WAVE PROFILES

In this section we describe intensity and phase measurements using the movable antenna $I_y(EM)$ of Fig. 1. This antenna is oriented orthogonally to the space charge antenna $I_x(SC)$ of section 3, and is sensitive to electric fields E_y parallel to the direction y of the launched TE_{10} electromagnetic wave. In the absence of FEL activity measurements show that $I_y(EM)$ varies as $\cos^2(\pi x/a)$ in accordance with expectations. This has been found to be so both in the absence of the electron beam (cold tests), and also in its presence, provided that the relevant FEL parameters were far removed from the resonance conditions (1) and (2).

In the presence of FEL activity the electric field intensity profile measured with antenna $I_y(EM)$ can be modified by one of two effects: optical guiding and contribution from the ambient space charge field $E_y(SC)$ of the bunched beam. Figure 7 illustrates the extent to which the RF profile is altered. In plotting the percentage change as a function of displacement, we subtract the underlying $\cos^2(\pi x/a)$ variation.

The very substantial changes shown in Fig. 7 are in agreement with earlier measurements [14]. There, the observations were attributed to optical guiding. However, in view of the now available space charge field measurements of section 3 and recent theoretical input [12], [15] the earlier interpretation needs closer scrutiny. The point is, that the $I_y(EM)$ probe measures a signal that is proportional to $|E_y(EM)\cos(\omega t - k_{||}z) + E_y(SC)\cos(\omega t - (k_{||} + k_w)z)|^2$ which, after time averaging, consists of a sum of intensities $E_y^2(EM) + E_y^2(SC)$, and an interference term $2E_y(EM)E_y(SC)\cos(k_w z)$. And, even if $E_y^2(SC) \ll E_y^2(EM)$, the interference term can produce significant profile modifications.

To be sure, the space charge electric fields are zero at the electron beam center and are large only near the beam edge $x = \pm r_b, y = \pm r_b$ (see Figs. 1, 4 and 5). Also, $E_y(SC)$ is by symmetry exactly zero along the x axis. Along the x axis, $E_y(SC)$ should not contribute to the overall intensity, were it not for the fact that the antenna has a finite length in the y direction (~ 1 mm) and it can therefore pick up a small amount of y component of the space charge electric field. As a result, some contribution from $E_y(SC)$ occurs even along the x axis.

We have also carried out a series of measurements with the purpose of determining the relative amplitudes of the space charge and electromagnetic fields. We find that at spatial positions where each are at their maximum, the ratio $E_{SC}(r = r_b)/E_{EM}(r = 0) \approx 0.2$. This yields a value for the interference term whose magnitude is not inconsistent with the profile modifications shown in Fig. 7. To confirm this, we displaced the antennas axially by exactly half a wiggler period [such that $z' = z + l_w/2$] and performed a profile scan. The result is illustrated in Fig. 8. Comparing Figs. 7 and 8 we see that the profile "flipped over", an effect which must be attributed to a sign change in the interference term $2E_y(EM)E_y(SC)\cos(k_w z)$. A scan of the phase shown in Fig. 9 exhibits a similar effect.

5. DISCUSSION

This paper is an experimental study of the quasi-electrostatic and electromagnetic fields, and their relative importance, generated during FEL activity. The experiments were performed in a Raman free electron laser under conditions where the collective effects due to the RF space charge cannot be neglected.

Section 3 is devoted to the study of the RF intensity and phase of the space charge fields. The spatial distribution of the transverse field component $E_x(SC)$ represents essentially the fringe fields of the space charge bunches generated during FEL activity. These fields vanish on the z axis and are antisymmetric, as is clearly demonstrated by Figs. 4, 5 and 6.

In section 4 we examine the transverse spatial profiles of the electromagnetic wave. The observed modification (Fig. 7), though originally believed to be due to optical guiding [14], is now ascribed to the presence of a small but not insignificant contribution from the space charge fields of the bunches. The space charge wave travels at a somewhat slower speed than the electromagnetic wave and the two waves are phase-locked to one another. This gives rise to wave interference, and to profiles like those shown in Fig. 7. A dramatic example of this interference effect is illustrated by comparing these profiles with those of Fig. 8, which were measured at a second axial position Z' displaced one half a wiggler period downstream. Phase measurements of Fig. 9 provide additional confirmation of the interference phenomenon. Any true optical guiding of the electromagnetic wave that may be present is masked by interference effects with the space charge wave.

Interference among the several [15] waves generated in an FEL interaction is also believed to be the cause of the following interesting effect that we have observed in the course of our measurements. Oscilloscope traces like those illustrated in Fig. 2(b) exhibit an overall temporal shift as a function of the transverse position x of the antenna used on making the measurement. This is shown in Fig. 10(a) in which the $I_y(EM)$ probe, positioned at different transverse positions, is used in the measurement of the RF output. We see that as $|x|$ increases, the gain peak as well as the absorption dip move to later times, that is, to lower electron beam energies γ . We ascribe this to wave interference among the several interacting waves [15] each characterized by slightly different detuning parameters $\delta(x) = \omega/v_{||} - k_{||}(x) - k_w$ and different transverse wave profiles. When the gain is low (~ 3 dB), as it is in our experiments, all interacting waves carry roughly the same weight. The observed temporal changes can be translated into corresponding changes in the beam energy parameter γ . This is illustrated in Fig. 10(b), where we plot the beam energy for maximum FEL gain, $\gamma_{max}(x)$, as a function of the transverse antenna position

x .

In conclusion, then, the experimental observations presented in this paper can serve as a basis for a detailed theoretical study of profile modifications in a Ramam FEL. To date, the theoretical analyses are in qualitative agreement with our measurements. However, there are large numerical differences. For example, theory predicts [12] that the ratio of the space charge to the electromagnetic field amplitude is ~ 0.02 which is about an order of magnitude smaller than the measured ratio. Similarly, the predicted change [15] in the temporal pattern as a function of transverse position x is much smaller than that obtained from the measurements like those shown in Fig. 10.

ACKNOWLEDGEMENTS

This work was supported in part by the Air Force Office of Scientific Research and in part by the National Science Foundation.

REFERENCES

- [1] P. Sprangle, R. A. Smith, and V. L. Granatstein, *Infrared and Millimeter Waves*, edited by K. J. Button (Academic, New York, 1979), Vol. 1, p. 279, and references therein. also N. M. Kroll, and W. A. McMullin, *Phys. Rev. A* **17**, 300 (1978).
- [2] J. Fajans and G. Bekefi, *Phys. Fluids* **29**, 3461 (1986).
- [3] J. Fajans, J. S. Wurtele, G. Bekefi, D. S. Knowles, and K. Xu, *Phys. Rev. Lett.* **57**, 579 (1986).
- [4] T. J. Orzechowski, E. T. Scharlemann, and B. D. Hopkins, *Phys. Rev. A* **35**, 2184 (1987).
- [5] P. Sprangle and C. M. Tang, *Appl. Phys. Lett.* **39**, 677 (1981).
- [6] W. M. Kroll, P. L. Morton, and M. W. Rosenbluth, *IEEE J. Quantum Electron.* **17**, 1436 (1981).
- [7] J. M. Slater and D. D. Lowenthal, *J. Appl. Phys.* **52**, 44 (1981).
- [8] D. Prosnitz, A. Szoke, and V. K. Neil, *Phys. Rev. A* **24**, 1436 (1981); also D: Prosnitz, R. A. Haas, S. Doss, and R. J. Gelinas, in *Free Electron Generators of Coherent Radiation*, Physics of Quantum Electronics Vol. 9, edited by Stephen F. Jacobs, Murray Sargent, III, and Marlan O. Scully (Addison-Wesley, Reading, MA, 1982), p. 1047.
- [9] E. T. Scharlemann, A. M. Sessler, and J. S. Wurtele, *Phys. Rev. Lett.* **54**, 1925 (1985).
- [10] G. T. Moore, *Opt. Commun.* **52**, 46 (1984), and *Nucl. Instrum. Methods Phys. Res. Sect. A* **239**, 19 (1985).
- [11] J. Fajans, *J. Appl. Phys.* **55**, 43 (1984).
- [12] E. Jerby and A. Gover (to be published in *Phys. Rev. Letters*).
- [13] H. P. Freund and P. Sprangle, *Phys. Rev. A* **28**, 1835 (1983).
- [14] F. Hartemann, K. Xu, G. Bekefi, J. S. Wurtele and J. Fajans, *Phys. Rev. Lett.* **59**, 1177 (1987).
- [15] J. Fajans and J. S. Wurtele (to be published in *Phys. Fluids*).

FIGURE CAPTIONS

- Figure 1 Schematic diagram of the experimental arrangement showing the placement of the probing antennas.
- Figure 2 Oscilloscope traces of (a) the beam voltage; (b) RF field intensity of the electromagnetic wave; (c) intensity of the space charge wave; and (d) RF phase of the electromagnetic wave (see text). The straight lines in (b), (c) and (d) are traces when the beam is kicked out of the system 18 cm upstream from the antennas, thereby terminating FEL activity at that point. The experimental parameters are: $B_{||} = 1580$ G; $B_w = 130$ G; $\omega/2\pi = 9.7$ GHz; $I \simeq 1$ A; RF power input = 3 W.
- Figure 3 DC current density profile $J_z(x, y)$ of the electron beam, measured at the position of the dipole antennas.
- Figure 4 Transverse field intensity profiles of the space charge (ponderomotive) wave of the bunched electron beam at a time of maximum FEL gain. The cartoons in the upper right hand corner illustrate the directions of scan. The experimental parameters are the same as in the caption to Fig. 1 except that $B_w = 200$ G, $I \simeq 4$ A.
- Figure 5 Two dimensional presentation of the transverse field intensity profile of the space charge wave at a time of maximum FEL gain. The experimental parameters are the same as in Fig. 4.
- Figure 6 Transverse phase profile of the space charge wave at a time of maximum phase change (a) as a function of time during the voltage pulse; (b) as a function of antenna position at a time near zero gain (see text). The experimental parameters are the same as in Fig. 4.
- Figure 7 Two dimensional distribution of $I_y(EM)$ (the normalized electromagnetic wave intensity) at an axial position $z \simeq 115$ cm and at a time of maximum gain. The experimental parameters are the same as in Fig. 2.
- Figure 8 Two dimensional distribution of $I_y(EM)$ (the normalized electromagnetic wave intensity) at an axial position $z' = z + l_w/2$ and at a time of maximum gain. The experimental parameters are the same as in Fig. 2.
- Figure 9 Phase distribution as a function of transverse displacement at a time of maximum

phase change (near zero gain) at (a) $z = 115$ cm and (b) $z' = z + l_w/2$. The experimental parameters are the same as in Fig. 2.

Figure 10 (a) Oscilloscope traces (cf Fig. 2) of the beam voltage and of the intensity $I_y(EM)$ for 4 different positions z of the probing antenna, showing overall pattern shift to lower voltages. (b) beam energy parameter $\gamma_{max}(x)$ at maximum gain as a function of the axial displacement x .

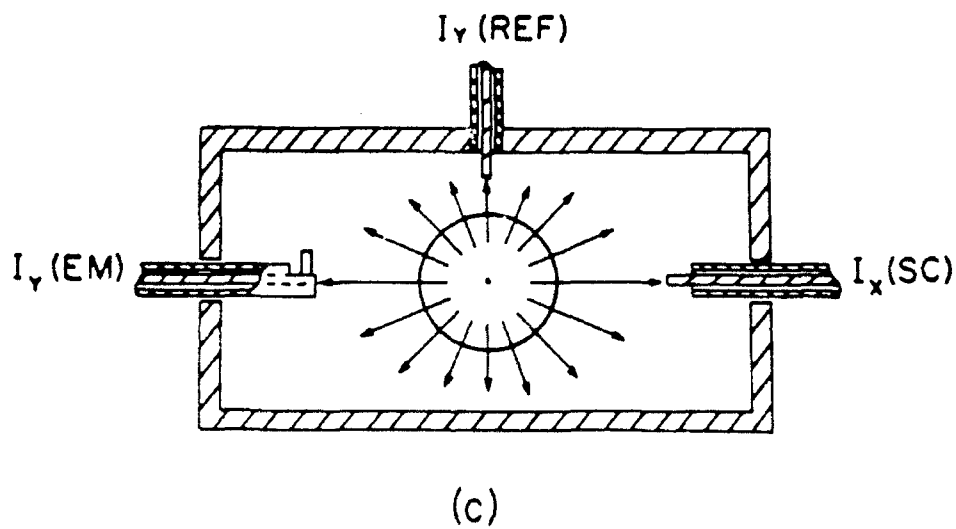
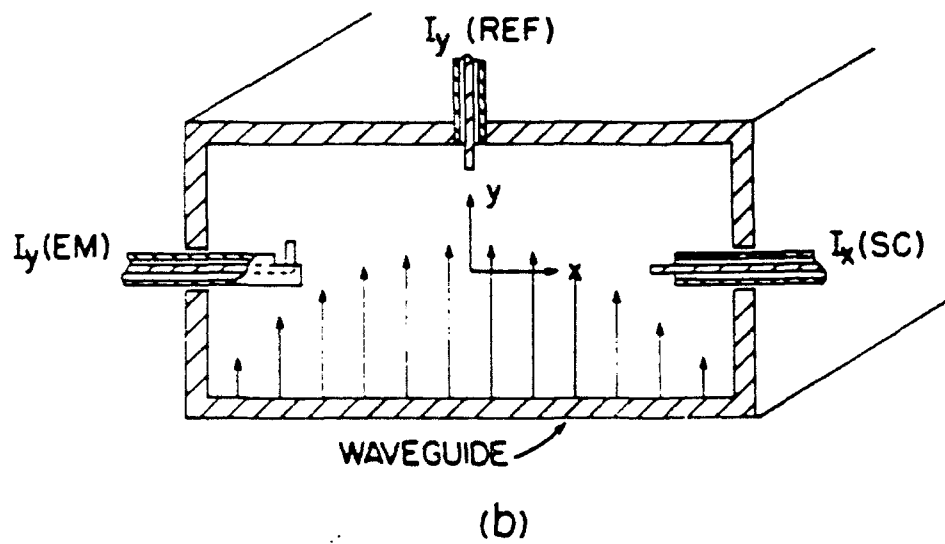
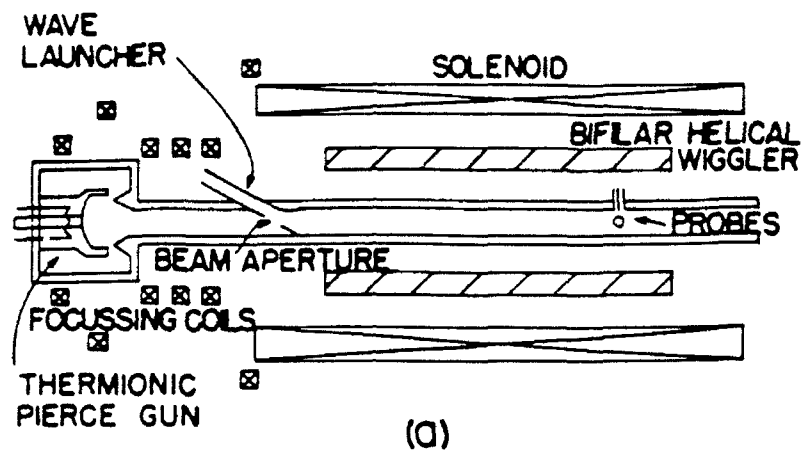


Fig.1 Xu,Bekefi,Leibovitch

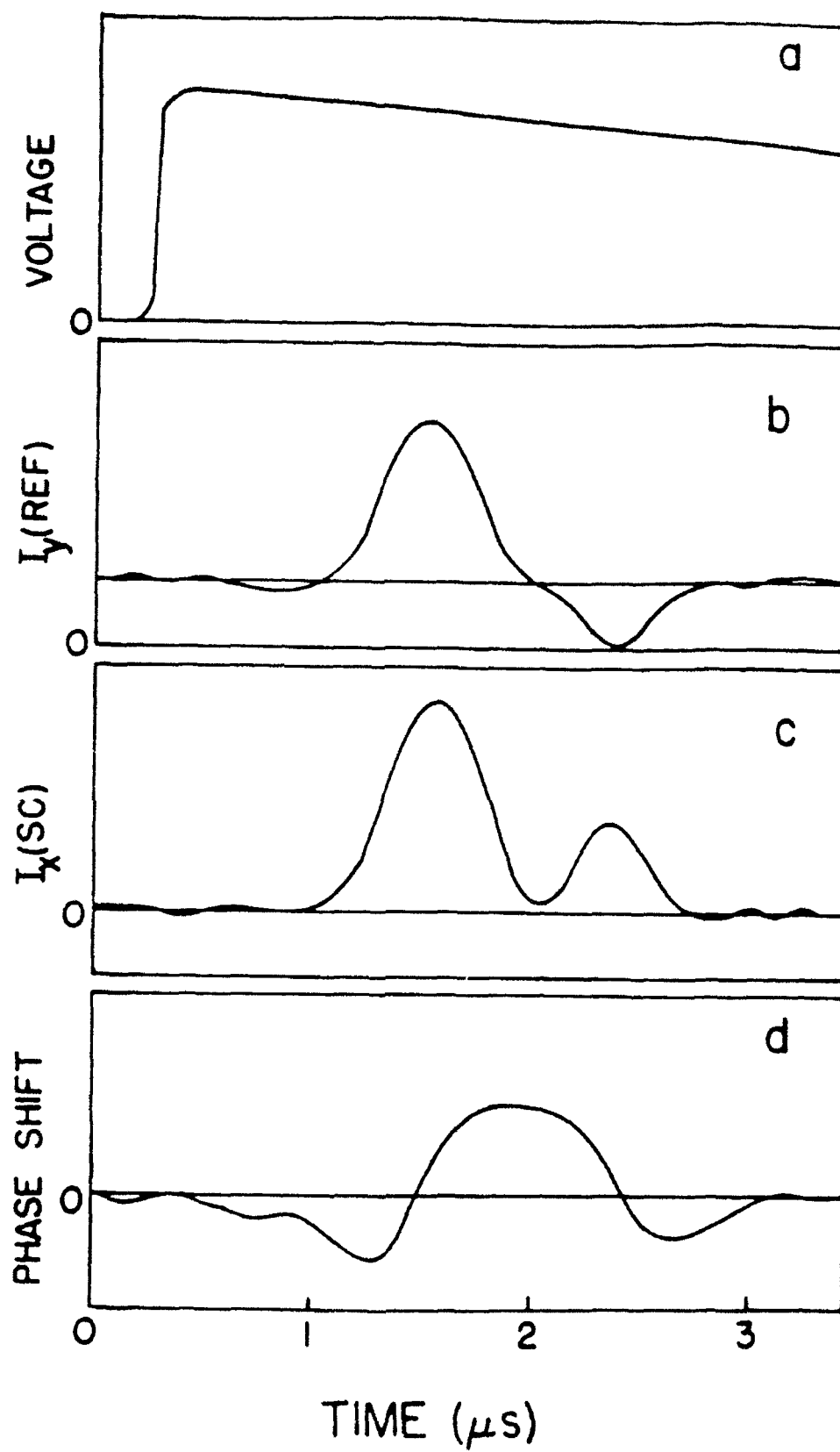


Fig.2 Xu,Bekefi,Leibovitch

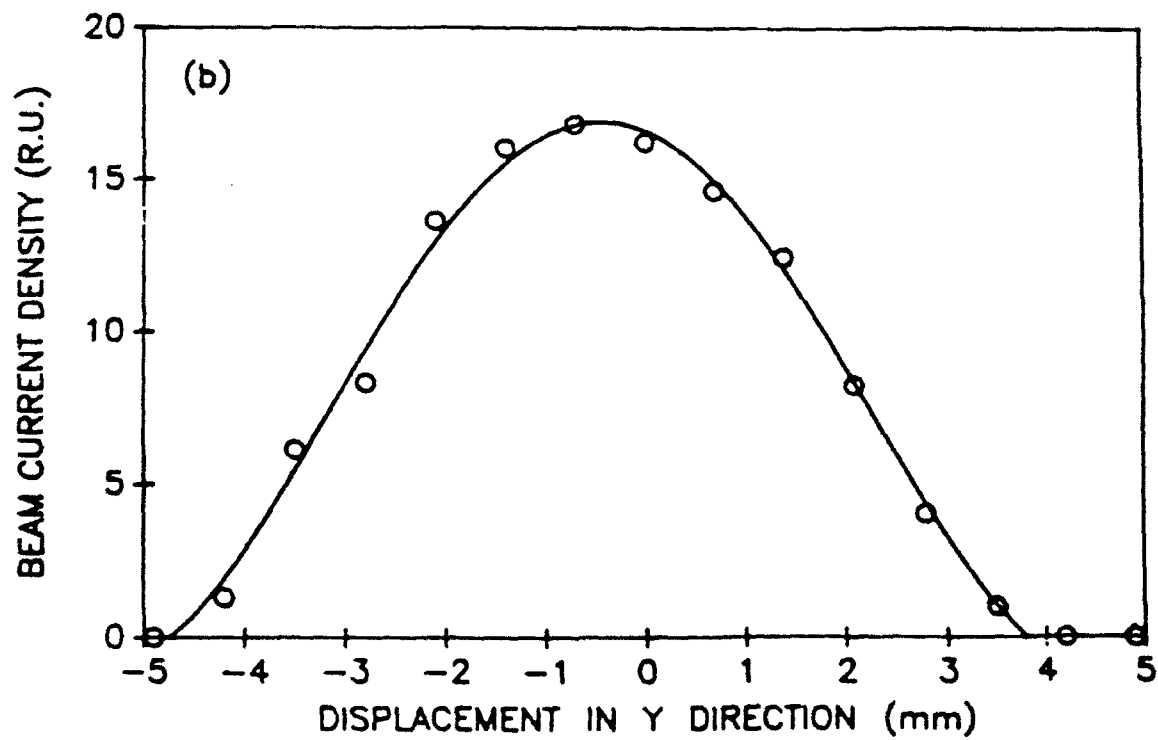
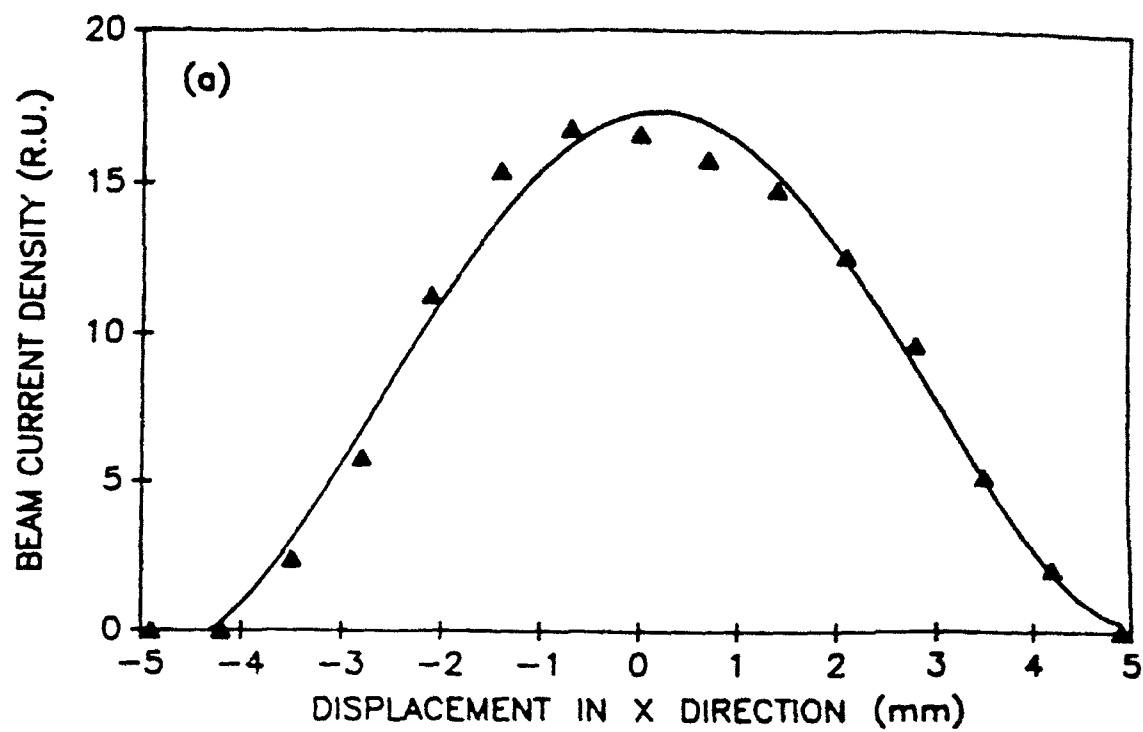


Fig.3 Xu,Bekefi,Leibovit

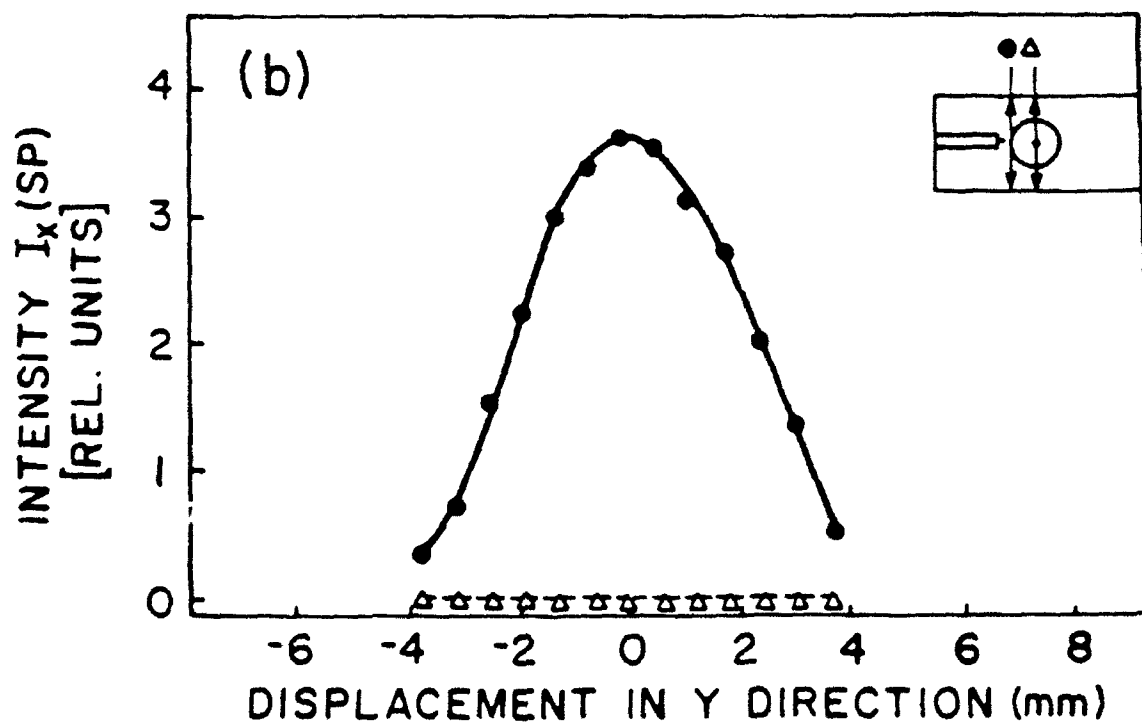
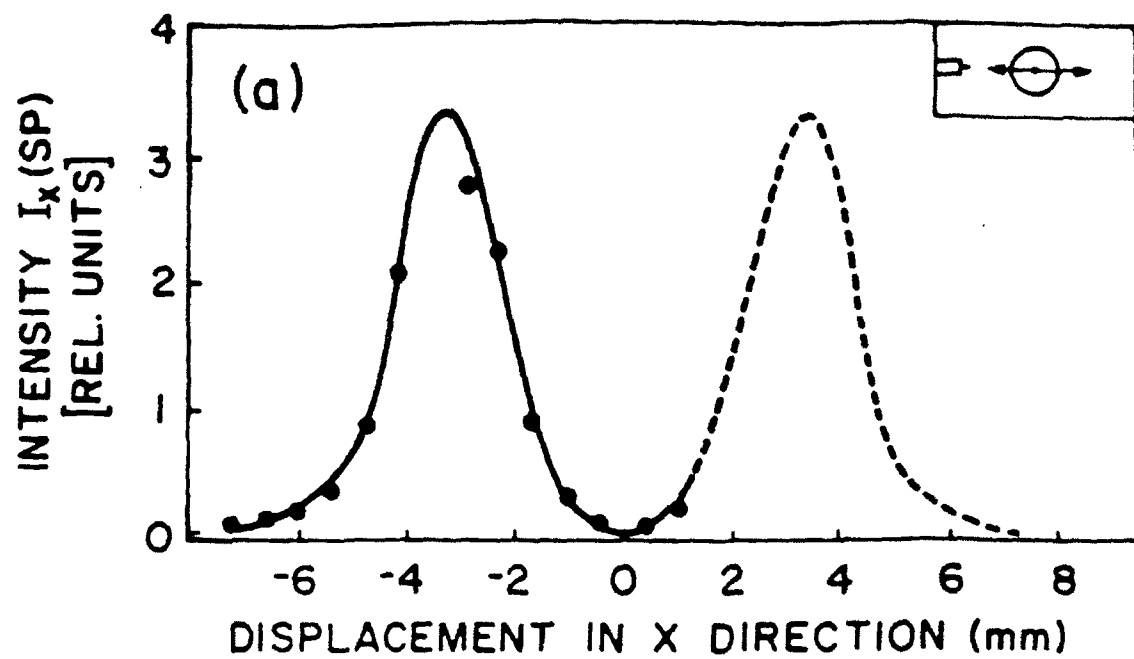
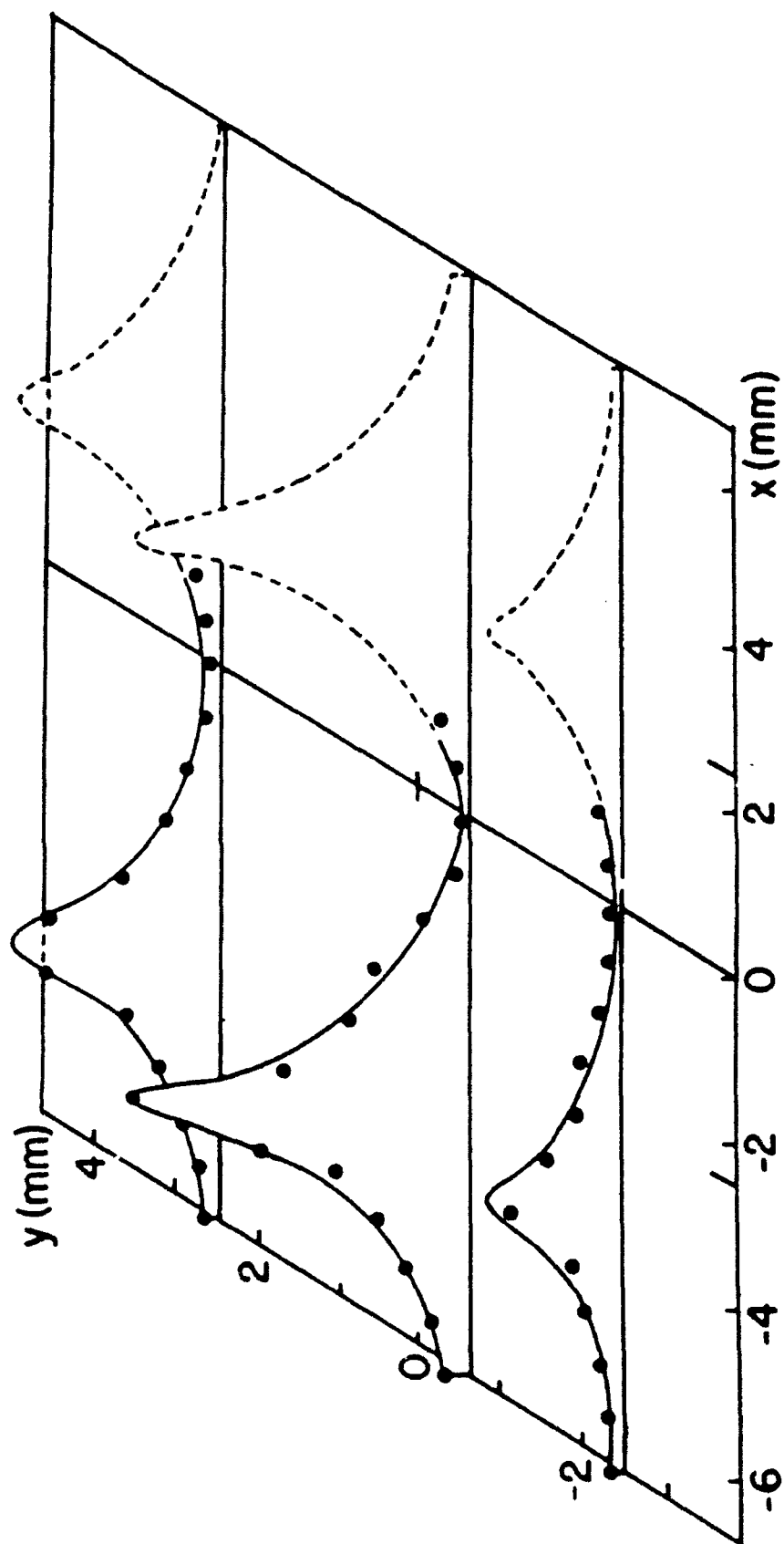


Fig.4 Xu, Bekefi, Leibovitch



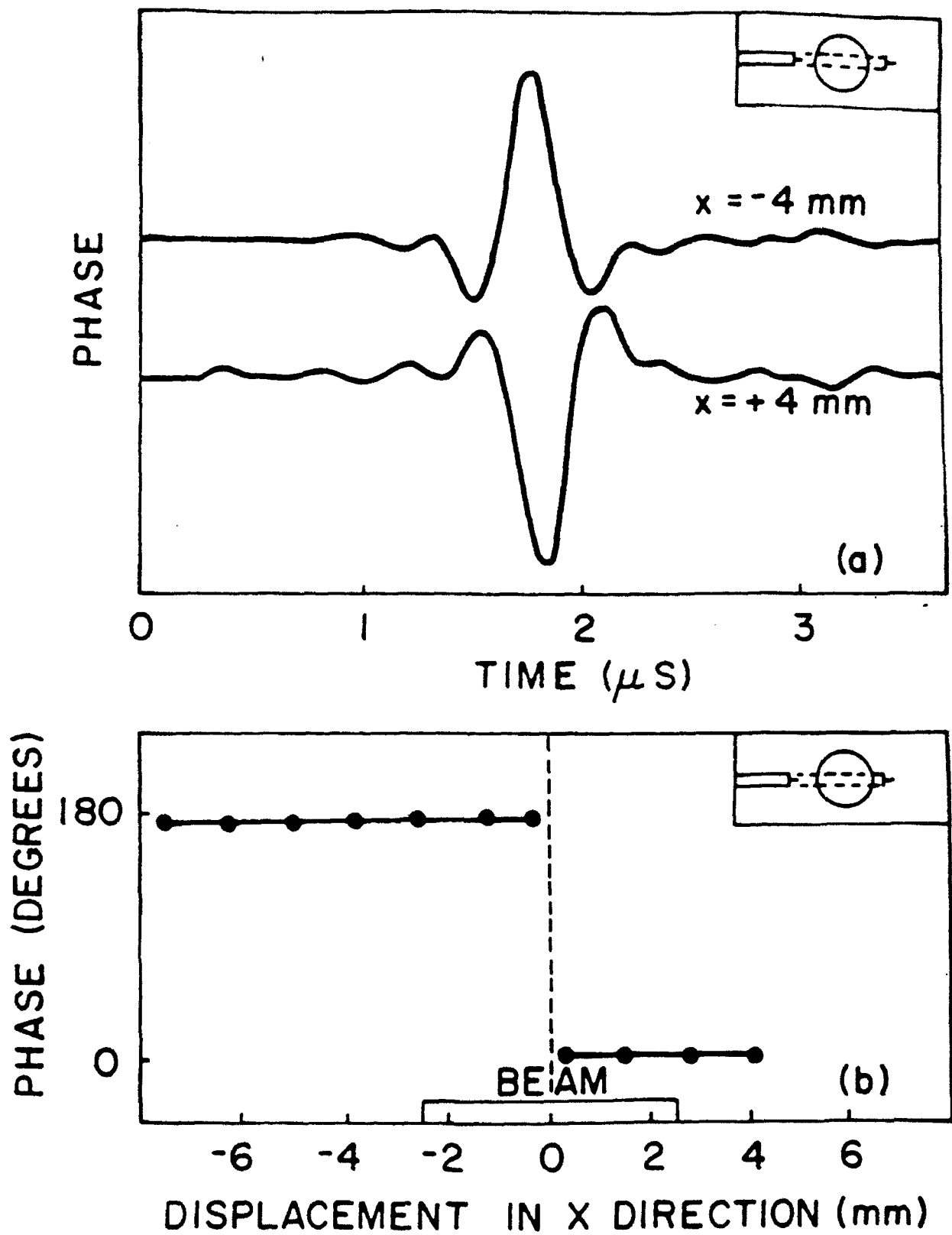
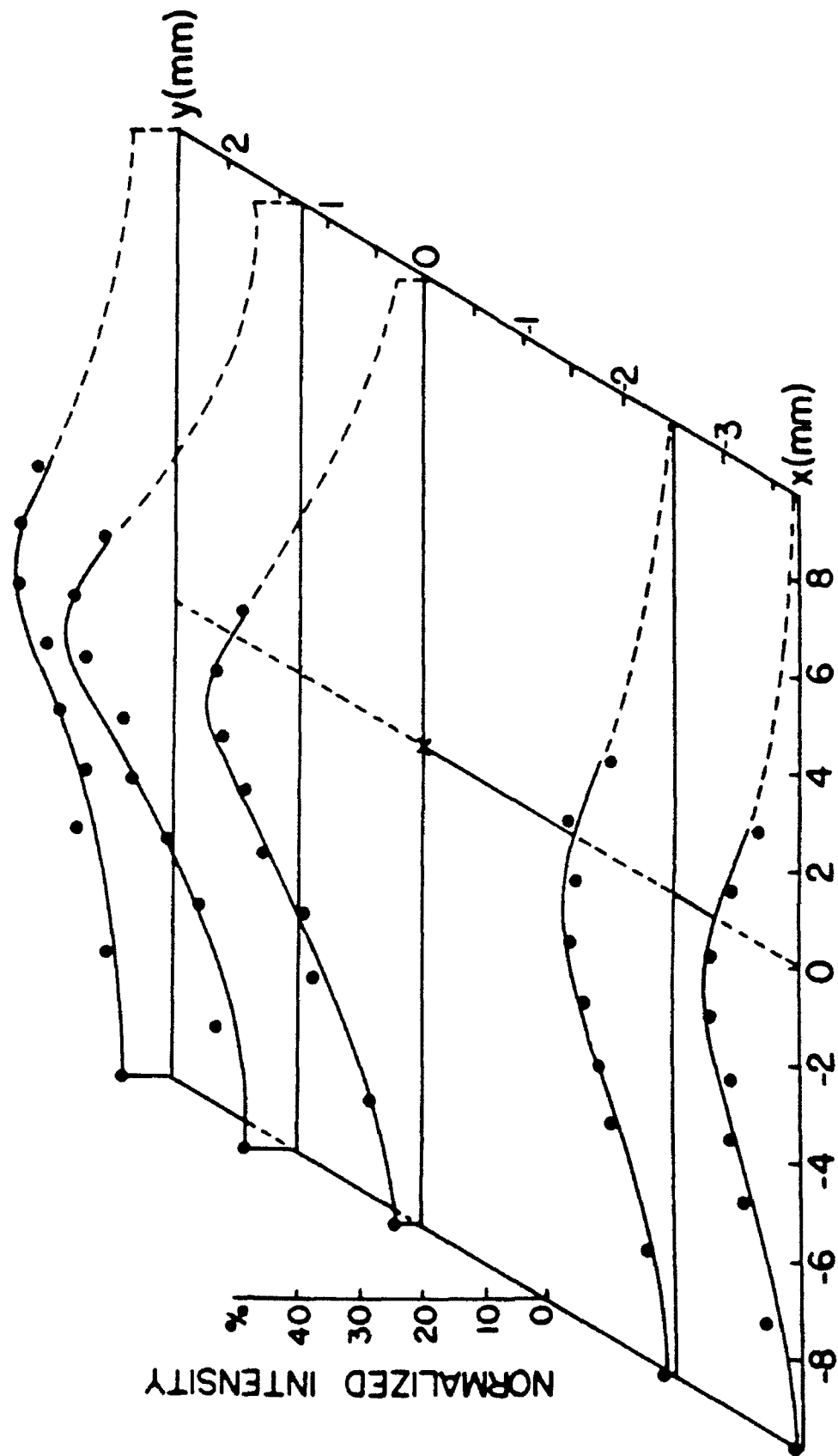


Fig.6 Xu,Bekefi,Leibovitch



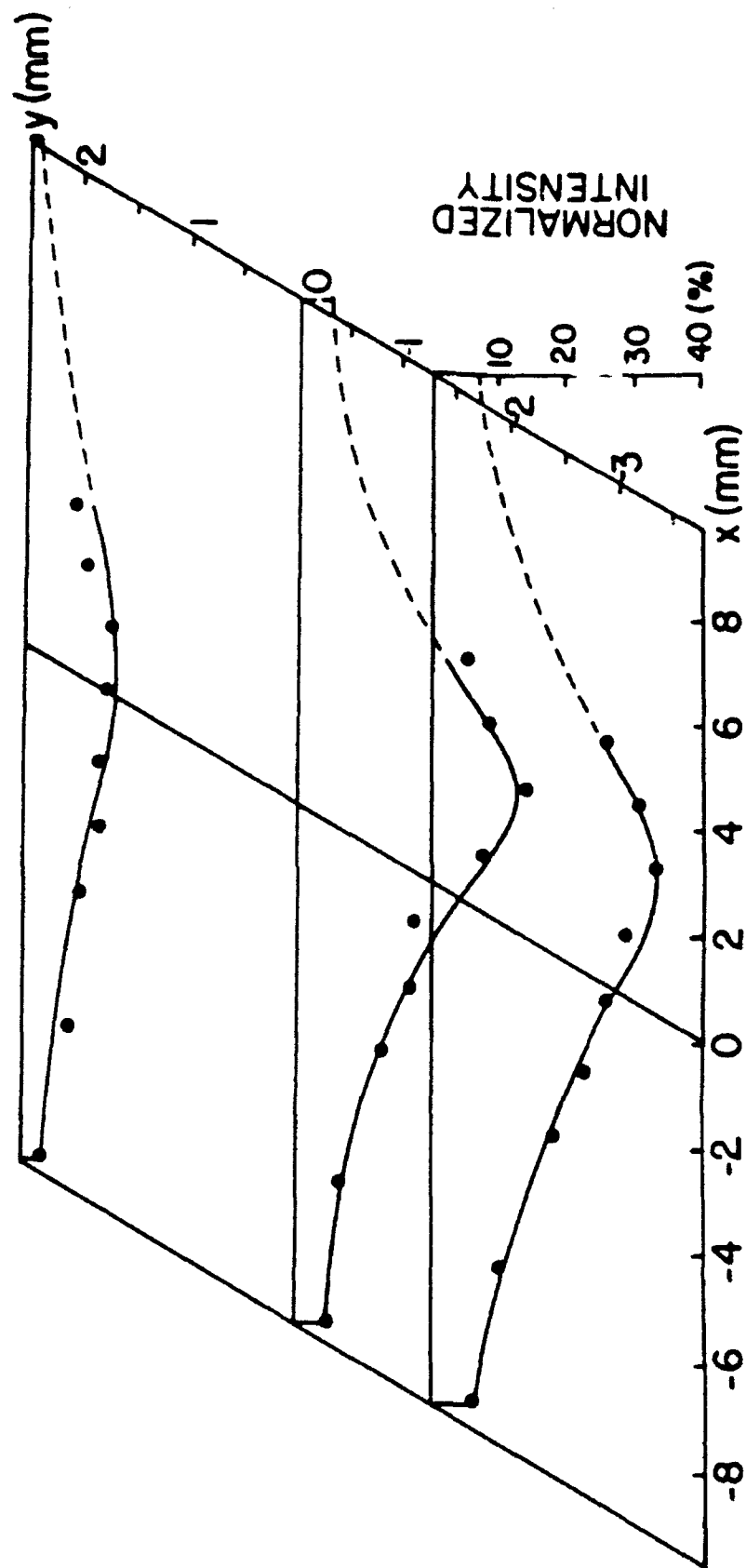


Fig. 8 Yu. Rekefi Izhnitsch

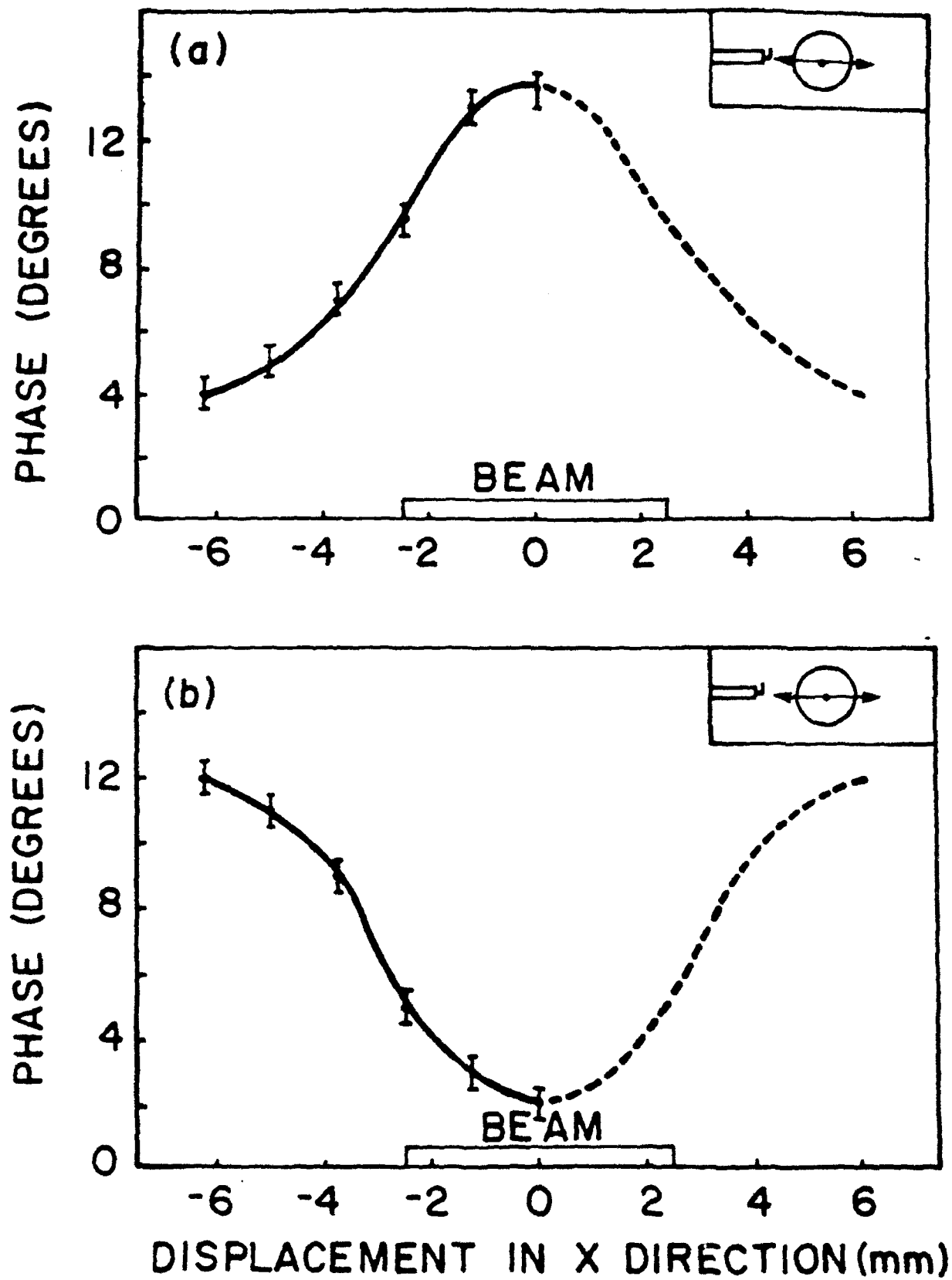


Fig.9 Xu,Bekefi,Leibovit

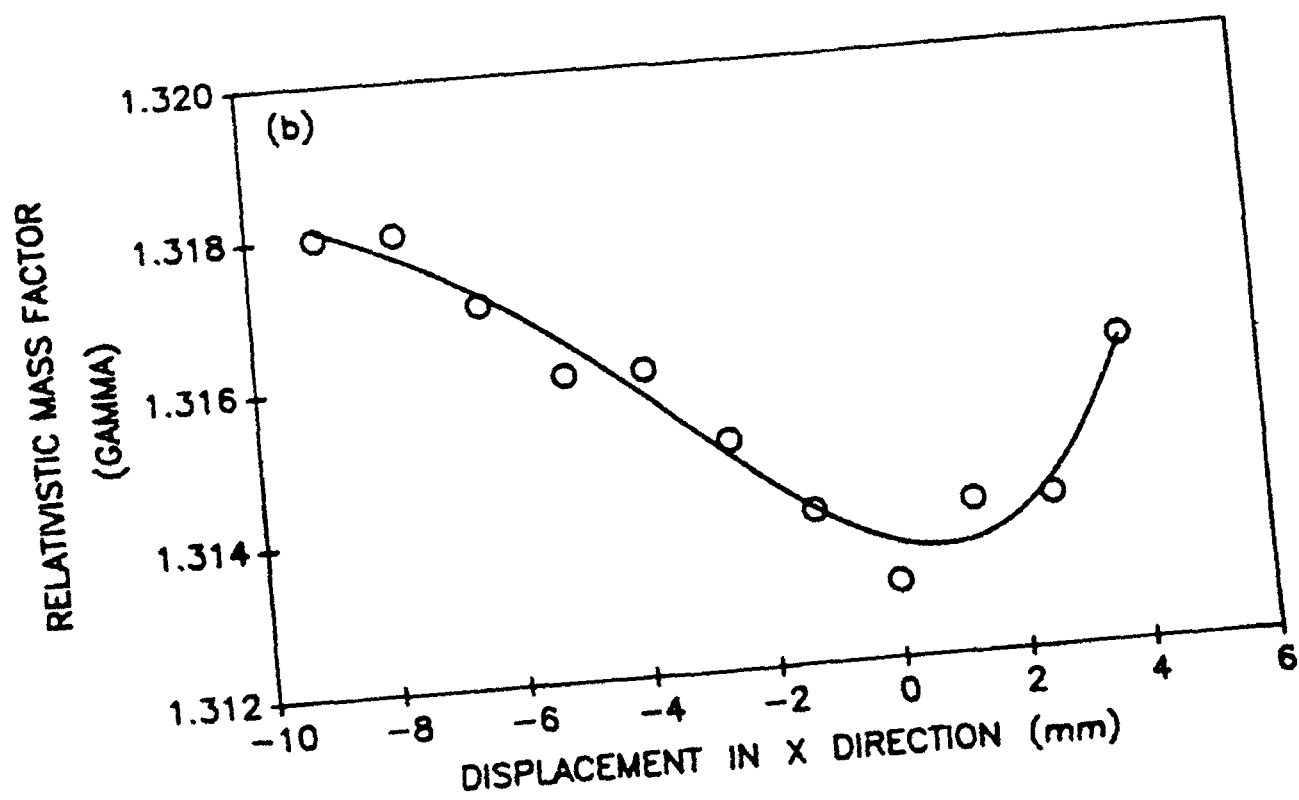
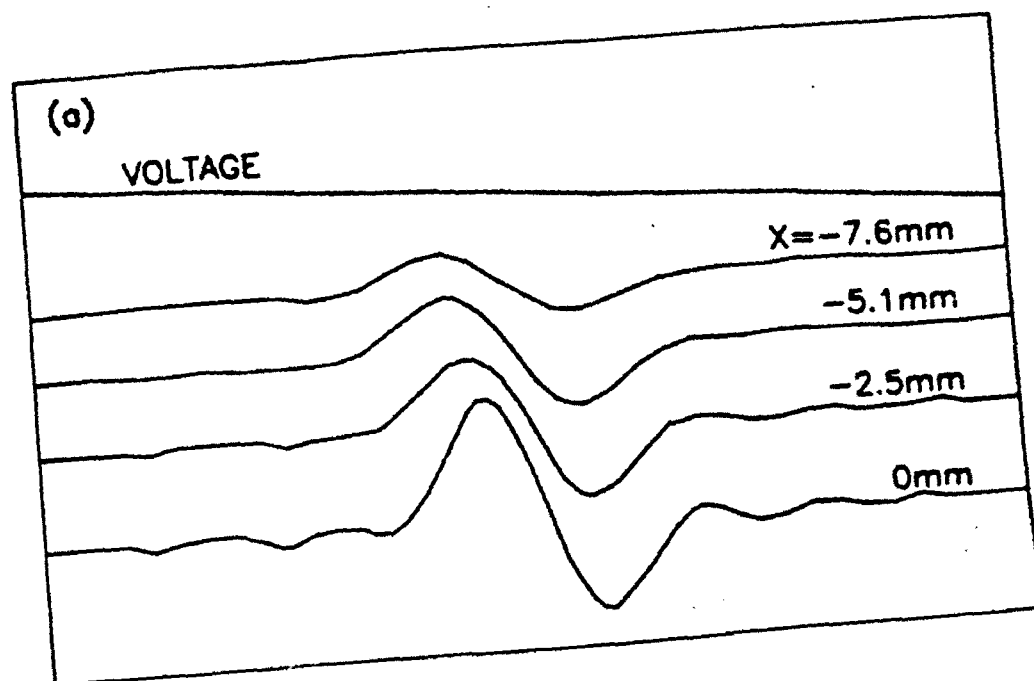


Fig.10 Xu,Bekefi,Leibovitch

PROJECT PERIOD
November 1, 1990 - October 31, 1991

Table of Contents

Project summary.....	91
The MIT 35 GHz cyclotron autoresonance CARM amplifier	92
A 35 GHz Ubitron-FEL amplifier	94
Basic studies of micropulse evolution and control	100
Appendix 1.....	106
Appendix 2.....	114

Project Summary

This is a continuation proposal on Microwave Emission from Relativistic Beams for the grant period of November 1, 1990 to October 31, 1991. Below we summarize the major research activities supported entirely or in part by the Air Force Office of Scientific Research.

The primary objective of the group is to develop a basic experimental and theoretical understanding of coherent generation by free electrons for wavelengths in the $1\mu\text{m}$ to 10 cm range. Particular emphasis is placed on free electron lasers, Čerenkov sources, relativistic magnetrons and other novel radiation sources.

The principal research activity described in this proposal is:

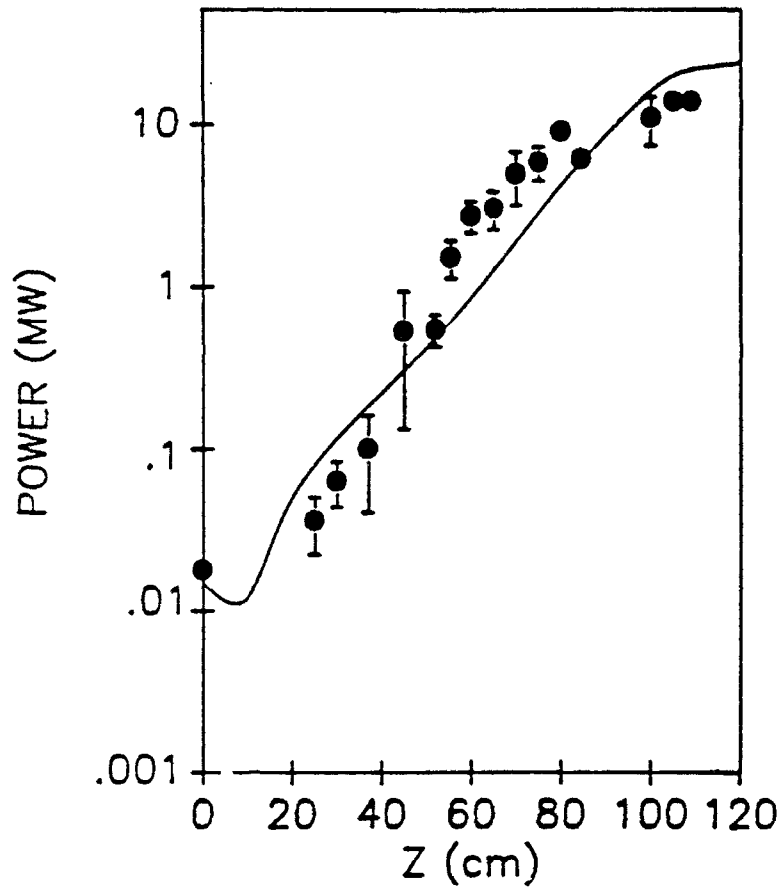
- (a) Development of ultra-high-power ($\sim 100\text{MW}$), high-frequency (10-40 GHz) coherent radiation sources.
- (b) Using these sources to power high-gradient accelerator sections for use in the next generation of rf Linacs.

1. The MIT 35 GHz Cyclotron Autoresonance Maser CARM Amplifier

We have now successfully completed research on what we believe is the first CARM amplifier. Power levels in the 20 MW regime have been achieved. Moreover, excellent agreement with theory is obtained, both in the linear and nonlinear regimes of operation. This is illustrated in Fig. 1. Here, the solid dots are from measurements and the curve is from a 3D numerical code developed at M.I.T. by C. Chen. More detail on the experiment is given in Appendix 1.

The experimental work was carried out by Anthony DiRienzo (a graduate student) and will soon be submitted to MIT's Physics Department in partial fulfillment of his PhD.

POWER GROWTH



Power as a function of interaction length for Group 1 wiggler orbits.

The dots are from measurements and the curve is from numerical simulations.

Figure 1

2. A 35 Ghz UBITRON-FEL AMPLIFIER

This high-efficiency FEL operates in the presence of a combined axial and wiggler magnetic field. The guide magnetic field is sufficiently high so as to place the operating regime in the region in which interaction with a space charge mode occurs. Here, according to Freund and Ganguly,¹ a negative mass instability is excited, leading to enhanced efficiency.

Our experimental setup is illustrated in Fig. 2, and the operating parameters are summarized in Table 1.

Experiments have recently begun and are being carried out by Manoel E. Conde, a graduate student. Figure 3 illustrates some of our initial measurements. It shows that the power increases exponentially with axial distance, as expected from theory. The measured growth rate is approximately 30 dB per meter, and the total power achieved in two polarizations is 25 MW. This corresponds to an efficiency of 22%.

Beginning this summer, this radiation will be fed into a ten-period accelerating section (see Figs. 4 and 5) loaned to us by the Lawrence Berkeley Laboratory (LBL). It was constructed and designed by Haimson Associates (cost: \$200,000). With the available power level, we expect to obtain accelerating gradients of approximately 100 MeV per meter length.

In the future we plan to improve the power output from our FEL by increasing the electron beam current. We hope to be able to achieve power levels in excess of 50 MW.

Reference

- ¹A. K. Ganguly and H. P. Freund, IEEE Trans. Plasma Sci. PS-16, 167 (1988).

SCHEMATIC OF THE EXPERIMENTAL SETUP

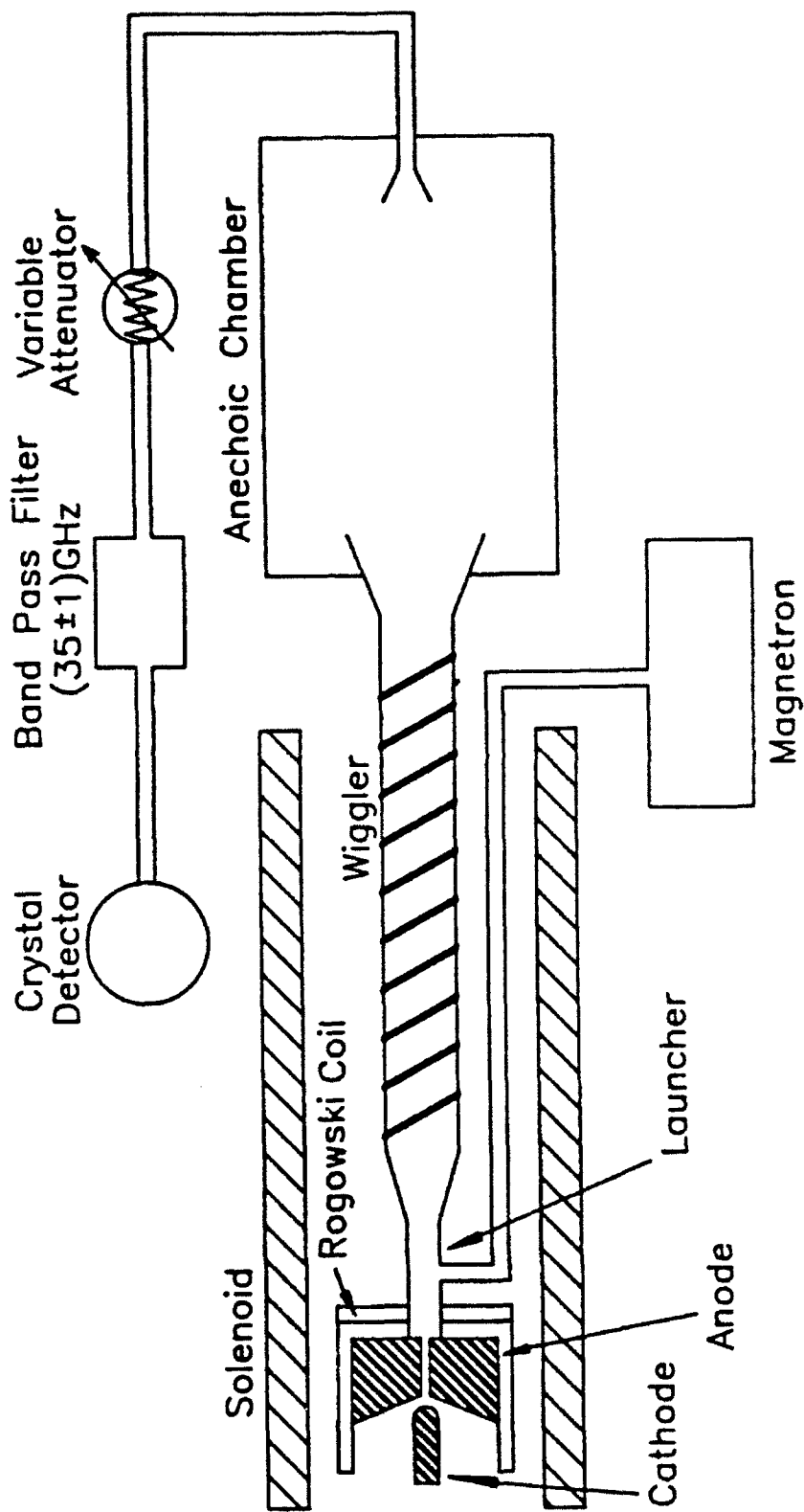


Figure 2

PARAMETERS

BEAM ENERGY	0.8 - 1.1 MeV
BEAM CURRENT	90 A
PULSE LENGTH	30 ns
RADIUS OF ELECTRON BEAM	0.25 cm
WAVEGUIDE RADIUS	0.51 cm
AXIAL MAGNETIC FIELD	9.0 - 12.6 kG
WIGGLER MAGNETIC FIELD	1.0 - 1.8 kG
WIGGLER PERIOD	3.18 cm
INPUT POWER	13 kW

Table 1

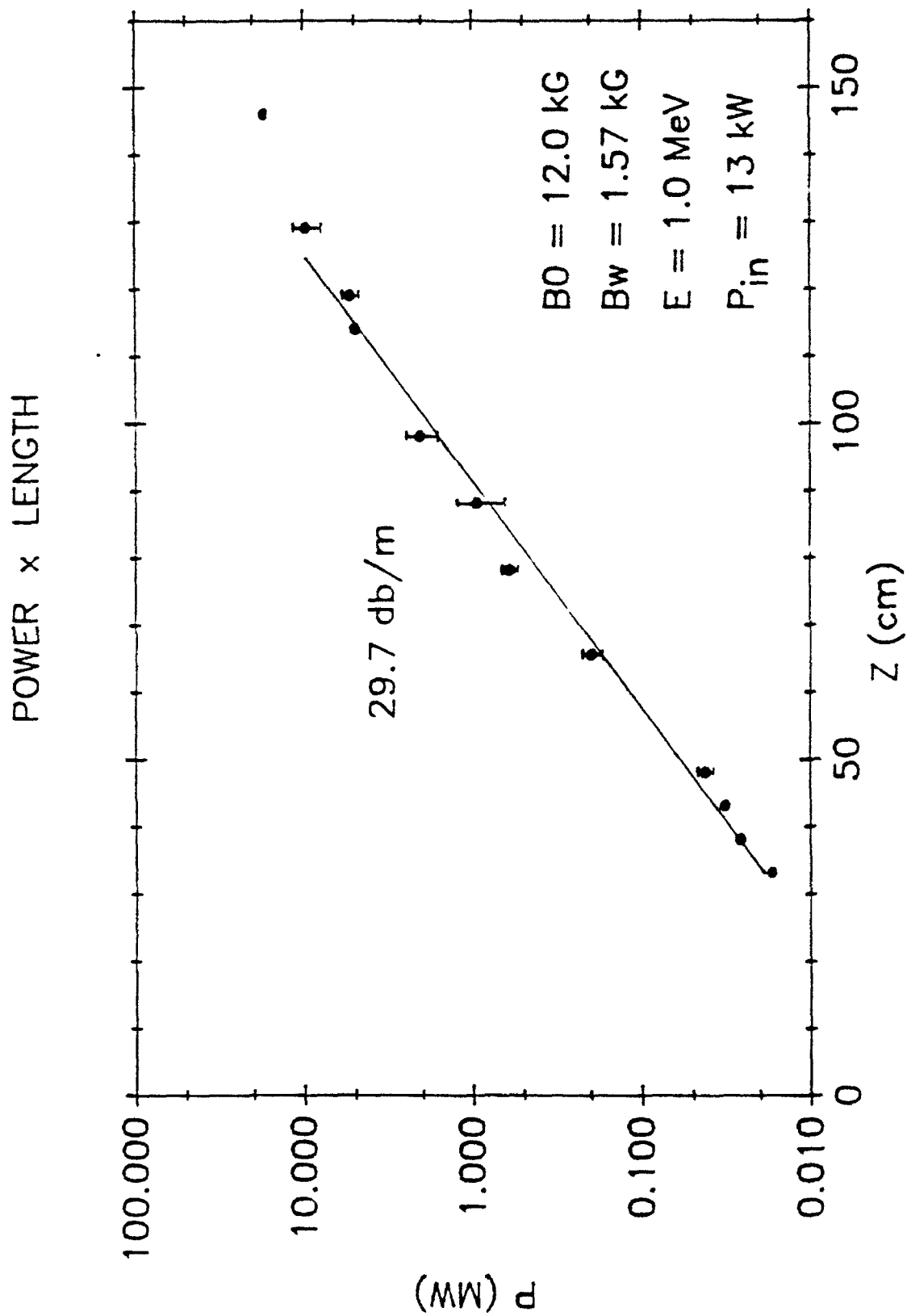


Figure 3

HIGH-GRADIENT ACCELERATOR TEST ASSEMBLY

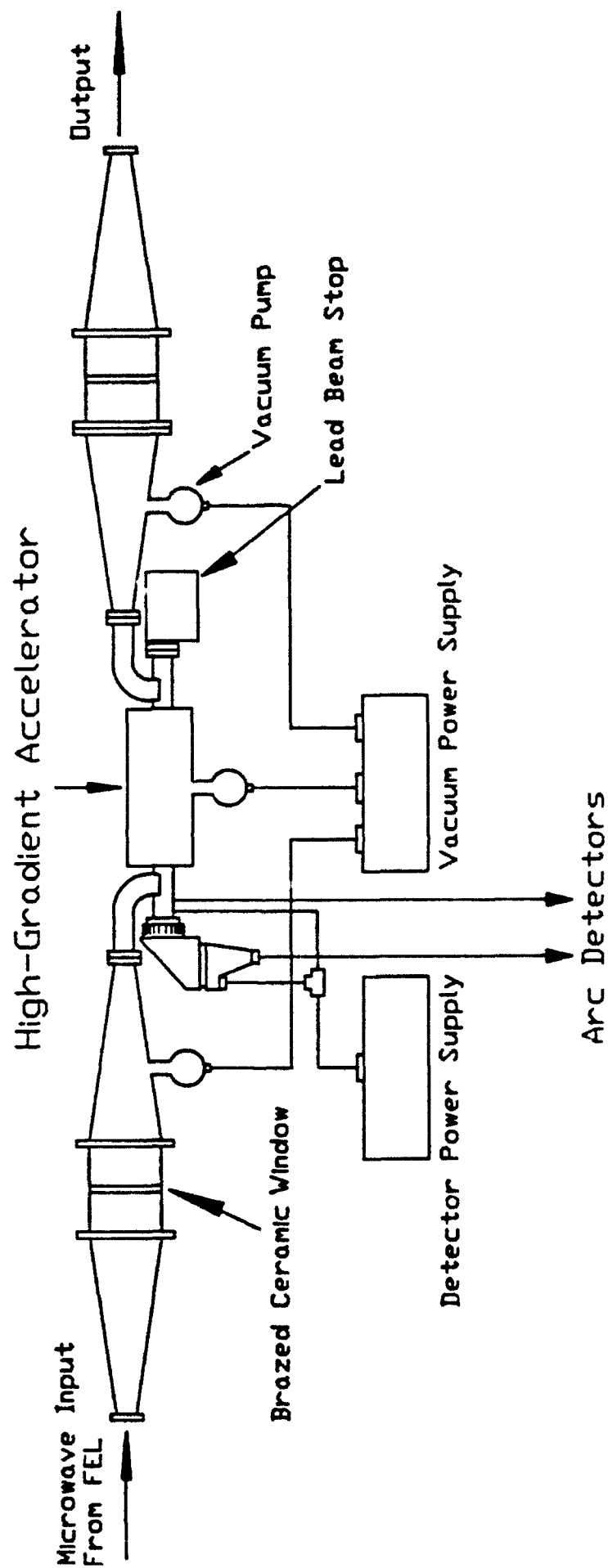


Figure 4

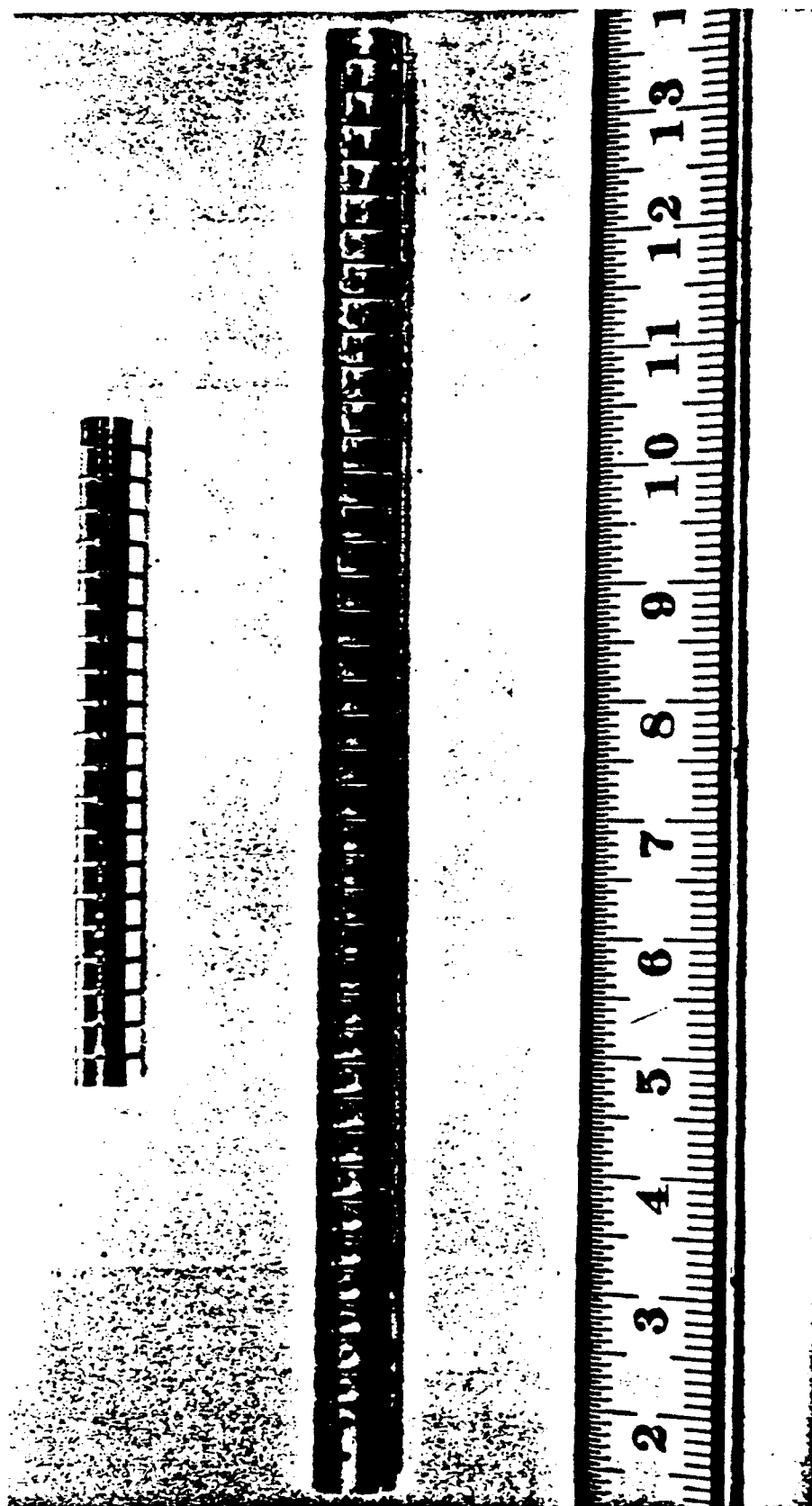


Figure 5

3. Basic Studies of Micropulse Evolution and Control

Studies of the evolution of the FEL signal from the spontaneously emitted background noise is an important topic in FEL research. Below we summarize our recent observations of spiking in an FEL oscillator. The initial observations will stimulate further studies of this phenomenon, which may well lead to methods of generating and controlling very short pulses and to ways of mode locking FELs.

Observations of spikes in the radiation power growing from noise in a free-electron laser oscillator are reported. These spikes, unlike those measured in previous studies⁹⁻¹², occur well before saturation, when the FEL is operating in the small-signal regime (and therefore they are not generated by the sideband instability). The FEL is driven by a continuous mildly relativistic electron beam ($E_{eb} \cong 200 \text{ KeV}$, $I \cong 1 \text{ A}$, $\tau \cong 25 \mu\text{s}$). It oscillates in the microwave regime (8-12 GHz) in a ring waveguide cavity. Periodic structures of spikes were observed. The width of each spike is roughly of the order of the slippage time (a few nanoseconds), and their period is roughly equal to a round-trip time in the ring oscillator ($\sim 40 \text{ ns}$).

The experimental set-up, shown in Fig. 6, is based on a FEL driven by a Marx accelerator without a pulse-forming network. It produces a continuous electron beam of $\sim 1 \text{ A}$ current and initial energy of 200 KeV. The e-beam energy decays exponentially with a time constant of $25 \mu\text{s}$, as $E_{eb} = 0.2 \exp(-t[\mu\text{s}]/25) \text{ MeV}$. A bifilar helical wiggler is used. Its parameters are $L_W = 2 \text{ m}$, $\lambda_W = 3.5 \text{ cm}$, and $B_W = 250\text{-}600 \text{ G}$. The e beam is confined to the axis by a $\sim 1 \text{ kG}$ focusing solenoid. The FEL operates in the microwave regime (8-12 GHz) in a rectangular waveguide (WR90).

The FEL oscillator is set up by connecting the output port to the input port with an external waveguide. Hence, a ring cavity with a total length of $L_c = 7.6 \text{ m}$ is formed. Figure 7 illustrates the observed microstructure and 8 shows predictions from computer simulations. These preliminary studies have been submitted to Physical Review Letters and are described in more detail in Appendix 2.

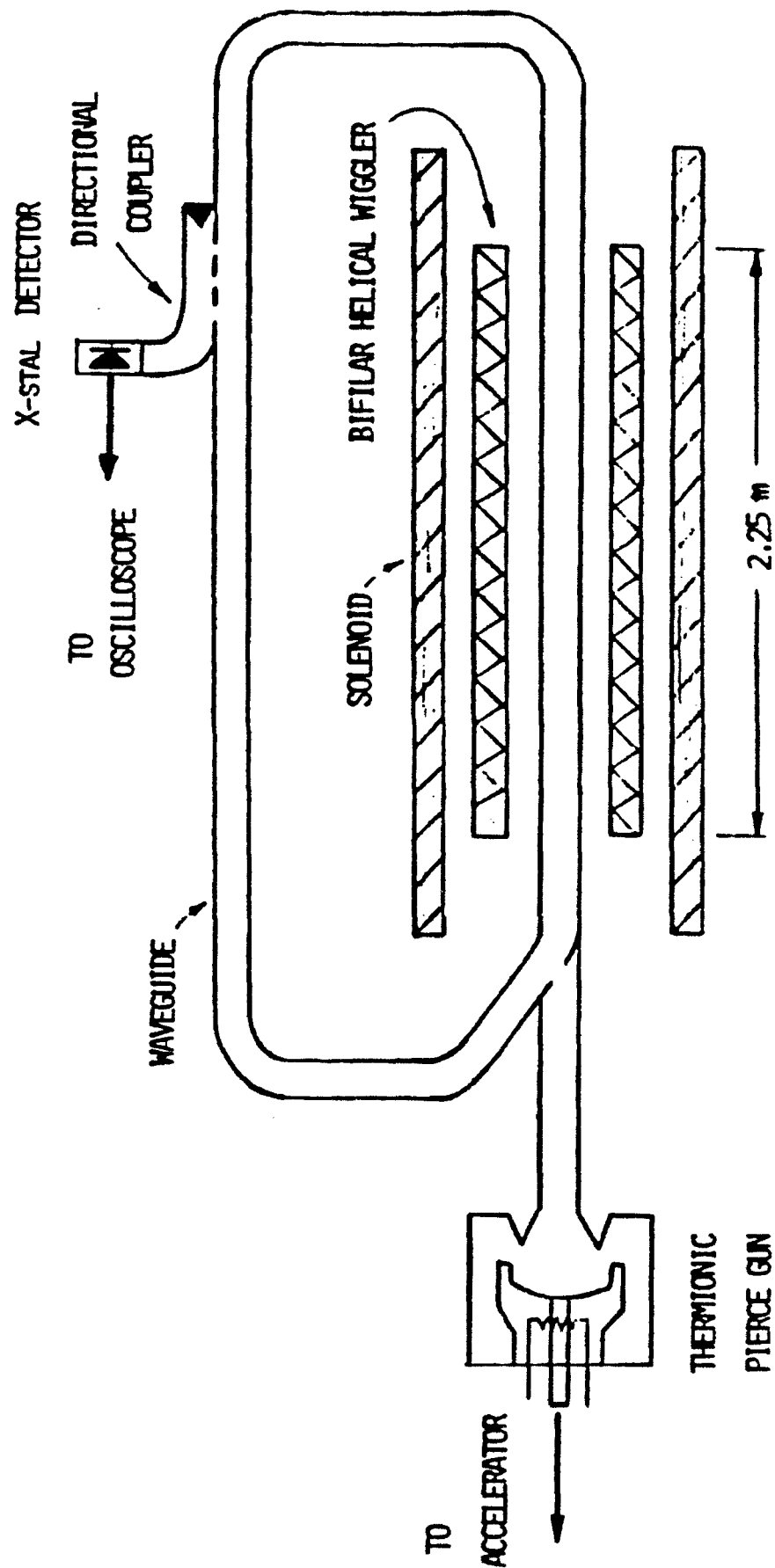


Figure 6

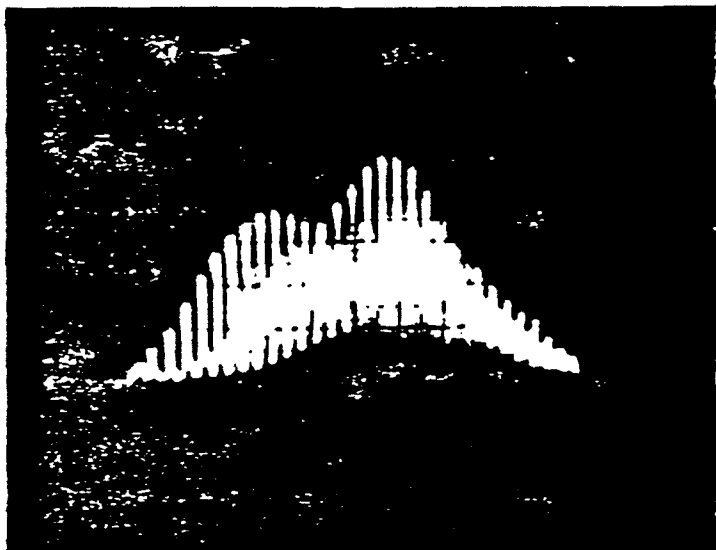


Figure 7

Impulse Response of the FEL Osc.

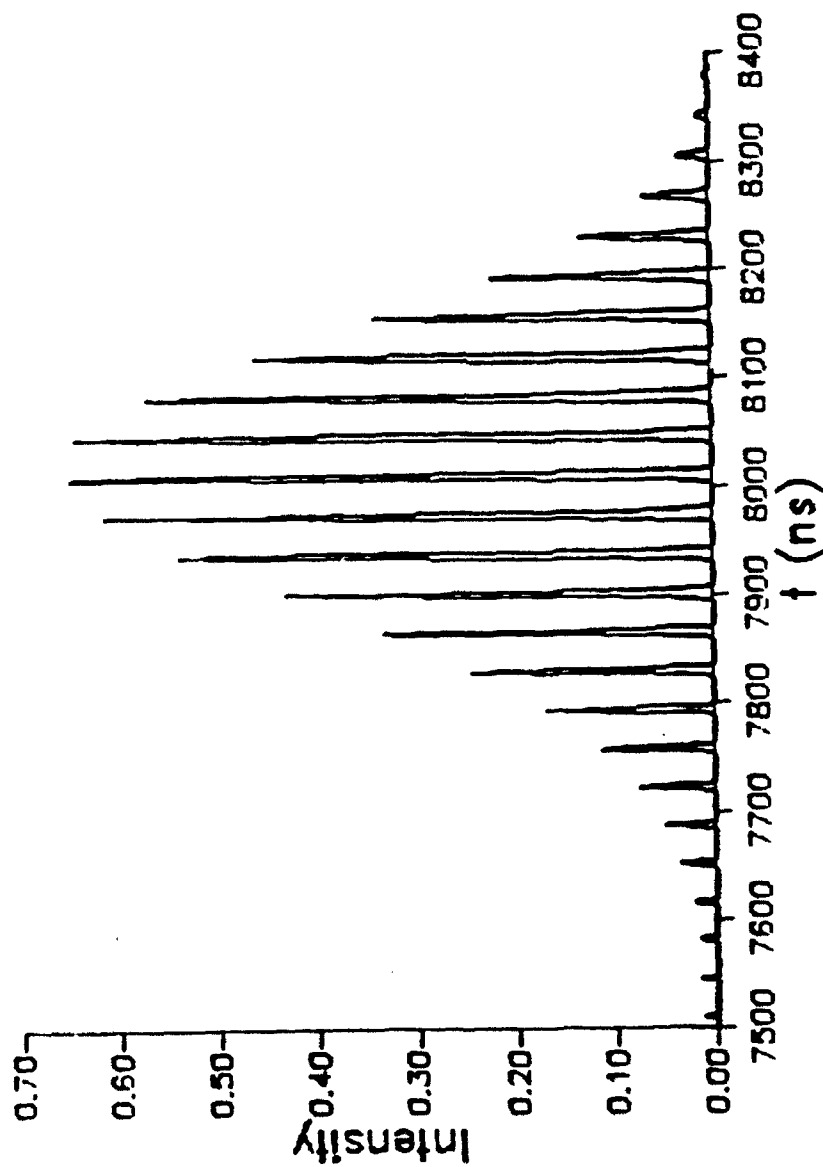


Figure 8

The origin and characteristics of the observed succession of spikes will be studied further and their relevance to mode locking will be investigated. We believe that this work has relevance to FEL mode control and to methods of generating very short tunable micropulses in free electron lasers. We expect this work to continue for the next twelve months or so.

References

1. S. C. Chen, G. Bekefi, S. DiCecca and A. C. Wang, *Proceedings of the Tenth International Conference on FEL*, Jerusalem, Israel, 1988 (North Holland, 1990), p. 290.
2. J. H. Booske, W. W. Destler, Z. Segalov, D. J. Racack, E. T. Rosenbury, T. M. Antonsen, Jr., V. L. Granatstein and I. D. Mayergoyz, *J. Appl. Phys.* **64**, 6 (1988) and the references therein.
3. R. M. White, *Appl. Phys. Lett.* **46**, 194 (1985).
4. G. Ramian, L. Elias and I. Kimel, *Nucl. Instr. Methods Phys. Res.* **A250**, 125 (1986).
5. B. G. Danly, G. Bekefi, R. C. Davidson, R. J. Temkin, T. M. Tran and J. S. Wurtele, *IEEE J. Quant. Electron.* **QE-23**, 103 (1987).
6. S. C. Chen, G. Bekefi, S. DiCecca and R. Temkin, *Appl. Phys. Lett.* **46**, 1299 (1989).
7. R. L. Sheffield, Workshop on Small Period Wigglers, LANL, April 1989.
8. K. Batchelor, I. Ben-zvi, R. Fernow, J. Gallardo, H. Kirk, C. Pellegrini, A. van Steenbergen, Brookhaven National Laboratory Report No. 43306 (1989).
9. B. A. Richman, J. M. J. Madey and E. Szarmes, *Phys. Rev. Lett.* **63**, 1682 (1989).
10. R. W. Warren, B. E. Newnam and J. C. Goldstein, *IEEE J. Quantum Electron.* **21**, 882 (1985).
11. J. Masud, T. C. Marshall, S. P. Schlesinger and F. G. Yee, *Phys. Rev. Lett.* **56**, 1567 (1986).
12. J. W. Dodd and T. C. Marshall, *Digest of the 11th International FEL Conference*, Naples, Florida; IEEE-LEOS 1989, L. R. Elias and I. Kimel, eds., p. 56.

APPENDIX 1

Reprinted from

Intense Microwave and Particle Beams

16-19 January 1990
Los Angeles, California



Volume 1226

©1997 by the Society of Photo Optical Instrumentation Engineers
Box 10, Bellingham, Washington 98227 USA. Telephone 206/676-3290.

The M.I.T.
35 GHz Cyclotron Autoresonance Maser (CARM) Amplifier

A. DiRienzo and G. Bekefi

Department of Physics
and
Research Laboratory of Electronics
Massachusetts Institute of Technology
Cambridge, Massachusetts 01239

Abstract

Studies of a cyclotron autoresonance maser (CARM) are presented. The measurements are carried out at a frequency of 35 GHz using a mildly relativistic electron beam (1.5 MeV, 300 A, 40 ns) generated by a field emission electron gun. Perpendicular energy is imparted to the electrons by means of a bifilar helical wiggler. Amplification measurements give a small signal growth rate of approximately 65 dB/m. The saturated power output is ~ 33 MW and the corresponding electronic efficiency is $\sim 7\%$.

Introduction

The cyclotron autoresonance maser (CARM) has the potential of becoming an interesting competitor to the gyrotron and the free electron laser as an efficient, high power electromagnetic source of millimeter and submillimeter wavelength radiation. Its capabilities are being studied theoretically [1-14] and experimentally as an oscillator [15] and as an amplifier [16-17]. This paper is a continuation of our earlier studies [16-17] of the CARM amplifier working at a frequency of 35 GHz, using a mildly relativistic electron beam with energy of 1.5 MeV and 300 A current. It is operated both as a superradiant source in which the radiation grows exponentially out of noise with a growth rate of 45 dB/m, and also as an amplifier excited by a high power magnetron driver with a growth rate of 65 dB/m. In the latter case, when it is driven to saturation, a peak output power of 33 MW and a corresponding electronic efficiency of 7% is achieved.

In addition to total RF power measurements, we also studied the angular distribution of the radiated power. We find that in the amplifier configuration, the radiation pattern corresponds to the lowest TE_{11} mode of excitation of our cylindrical waveguide. However, in the superradiant configuration, a more complicated radiation pattern results, suggesting excitation of at least two waveguide modes. We suspect that this multimoding is the cause of the reduced growth rate (45 dB/m) in the superradiant configuration as compared to the amplifier case (65 dB/m).

Experimental Setup

A schematic of the CARM amplifier is shown in Fig. 1. The accelerator potential is supplied by a Marx generator (Physics International Pulserad 110 A) with a maximum capability of 1.5 MV and 20 kA. The electron beam is generated by a field emission gun composed of a hemispherical graphite cathode and conical anode, which also acts as an emittance selector. The entire two meter long system is immersed in a solenoidal magnetic field.

The emittance selector removes the hot outer electrons. The remaining 300 A, 1.5 MV beam has a radius of 0.318 cm and a measured [18] normalized beam brightness equal to $2.8 \times 10^4 \text{ A cm}^{-2}\text{rad}^{-2}$. This corresponds to a normalized RMS emittance of $6.0 \times 10^{-2} \text{ cm-rad}$ and an RMS energy spread $\Delta\gamma_{||}/\gamma_{||} \approx 0.019$.

The electron beam is injected into a bifilar helical wiggler which imparts perpendicular energy to the electrons. The wiggler has a periodicity of 4.06 cm and is 6 1/2 periods long. Within the first 5 1/2 periods the wiggler magnetic field increases slowly and thereby provides an adiabatic input for the electron beam; the last period provides a uniform wiggler field with an amplitude on axis equal to 850 G. The resulting transverse electron velocity $v_{\perp} \approx 0.3v_{||}$. Fig. 2 shows the magnitude of the wiggler field components as a function of z . The downstream end of the wiggler is terminated abruptly by means of a metal shorting ring and the spinning electrons are allowed to drift into the 120 cm-long CARM interaction region where they are subjected to the uniform axial magnetic field only. In this region the axial magnetic field is typically 5.4kG and corresponds to the resonance requirements for CARM operation at 35 GHz:

$$\omega \approx \Omega_0 \frac{\gamma_{||}^2}{\gamma} \left\{ 1 \pm \beta_{||} \left[1 - \left(\frac{\omega_c \gamma}{\Omega_0 \gamma_{||}} \right)^2 \right]^{1/2} \right\}$$

Here Ω_0 is the nonrelativistic electron cyclotron frequency, $\beta_{||} = v_{||}/c$, $\gamma_{||} = (1 - \beta_{||}^2)^{-1/2}$, $\gamma = (1 - \beta_{||}^2 - \beta_{\perp}^2)^{-1/2}$, $\beta_{\perp} = v_{\perp}/c$, and the positive sign refers to the sought after Doppler upshifted CARM mode of operation.

We note that in the wiggler region the axial magnetic field is such that

$$\Omega_0 < k_w v_{||} \gamma$$

where $k_w = 1.55\text{cm}^{-1}$ is the wiggler wavenumber and $v_{||}$ is the axial electron velocity. This corresponds to the so called Type I orbits. This configuration differs from our earlier one [16,17] in which $\Omega_0 > k_w v_{||} \gamma$ and where $k_w = 0.90\text{cm}^{-1}$. The shorter wiggler periodicity leads to smaller electron excursions and thus a tighter electron beam. This greatly facilitates the electron beam alignment in the cylindrical drift tube.

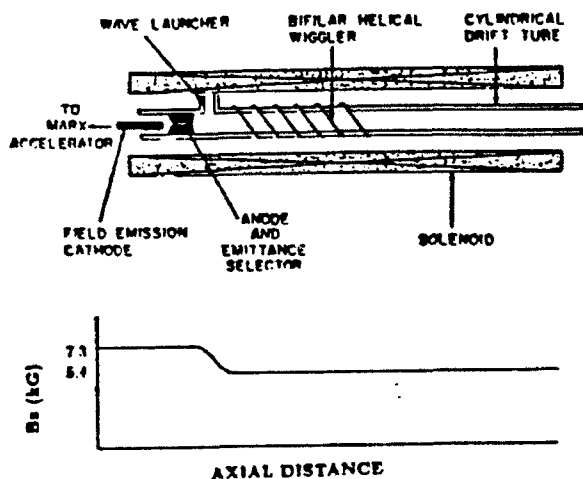


Fig.1 Schematic of the CARM apparatus

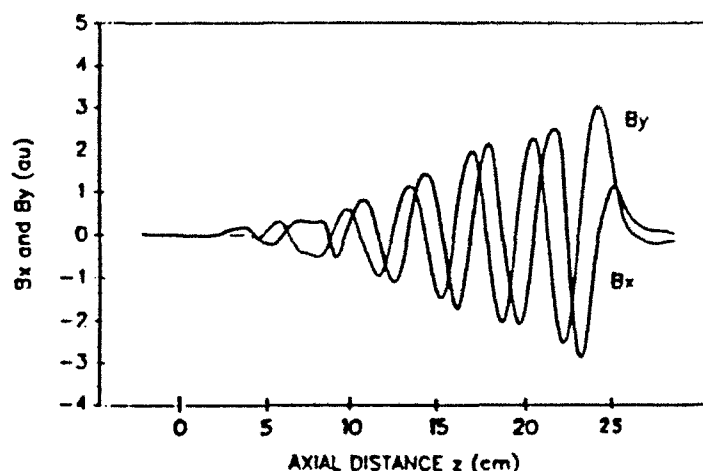


Fig.2 Wiggler magnetic field components B_x and B_y . Note the adiabatic uptaper and the abrupt cutoff.

Radiation Measurements

The CARM has been operated in two modes. In the superradiant mode, the signal has been allowed to grow out of the background RF noise. In the second mode, it operates as an amplifier of a high power input RF signal from a 35GHz, 100kW magnetron driver. In both cases the output signal is passed through a band pass RF filter, centered on 34.45GHz and with a bandwidth ΔB of 2.4GHz, before detection with calibrated crystal detectors. In this manner all extraneous signals are filtered out. In the amplifier mode the signal frequency Δf is, of course, much narrower than ΔB , and is typically equal to the bandwidth of the magnetron driver. However, in the superradiant mode, the signal frequency bandwidth is typically the CARM gain bandwidth which is considerably greater than ΔB . Using the filter in all of our measurements allowed us to make meaningful comparisons of the gains, growth rates and radiation patterns of the amplifier and superradiant systems.

In order to determine the growth rate of the wave, the output intensity is measured as a function of the length of the interaction region, z . This is accomplished by means of an axially movable horseshoe kicker electromagnet that deflects the electron beam into the waveguide wall at any desired position z , thereby terminating the interaction at that point. The position $z = 0$ denotes the end of the wiggler and the beginning of the CARM (wiggler free) interaction region.

In the superradiant mode we measure an unsaturated growth rate of 45 dB/m. This is shown in Fig. 3. No noticeable radiation was present in the wiggler region alone, all measureable radiation was due only to interactions within the CARM region. We note that the power grows roughly exponentially with the distance z with no evidence of saturation. This lack of saturation is not surprising since the CARM signal must grow out of a low power noise signal.

Fig. 4 shows the angular scan of the radiation pattern measured in the E plane in the (distant) Fraunhofer field of a conical horn attached to the cylindrical waveguide (horn radius equals 3.3 cm). Also shown for comparison is the angular scan of the magnetron driver radiating in the TE_{11} mode. We observe a central maximum and a very large side lobe at an angle of $\approx 15^\circ$. This suggests, that in the superradiant configuration, multimoding is taking place. Comparison with the radiation pattern from the magnetron signal alone (no electron beam) suggests that we are observing a combination of the radiation from the lowest TE_{11} waveguide mode which has a central maximum and a second mode (possibly the TM_{01} mode) which has a central minimum and a large off-axis lobe.

Utilizing the microwave input coupler shown in Fig. 1, a linearly polarized, TE_{11} mode, 30 kW input signal at 34.73 GHz was injected into the CARM. Fig. 5 shows the power gain as a function of z for the amplified signal. Saturation occurs after 60 cm of interaction length with a gain of 65 dB/m. A peak power of 33 MW is achieved. In order to insure that the TE_{11} mode of the input RF signal was the only signal amplified and that no satellite modes were excited by the CARM interaction, an angular scan of the power output was obtained and compared with the radiation pattern for the magnetron alone. This is shown in Fig. 6; the good agreement between the two radiation patterns confirms the fact that the input TE_{11} mode only is indeed amplified.

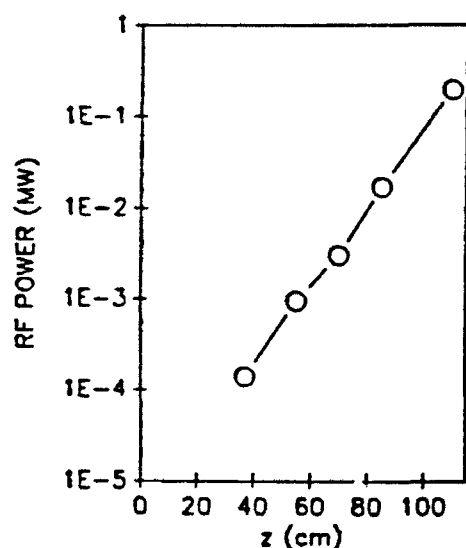


Fig.3 Power gain for the superradiant configuration as a function of interaction length.

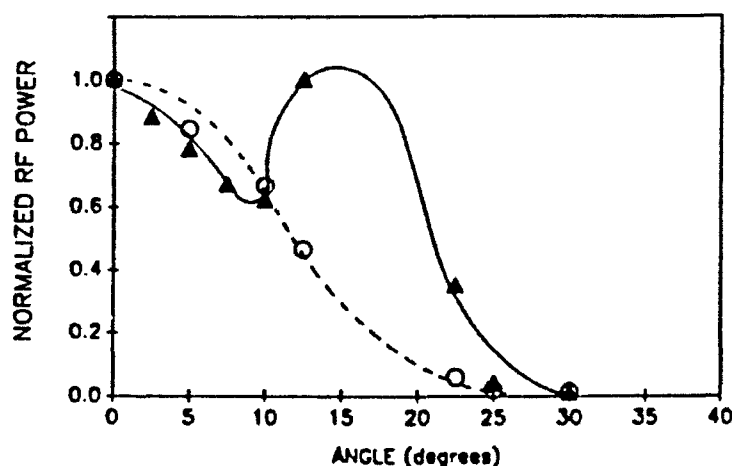


Fig.4 Angular scan for the superradiant configuration. Open circles are for comparison to the TE_{11} mode of the input magnetron signal alone.

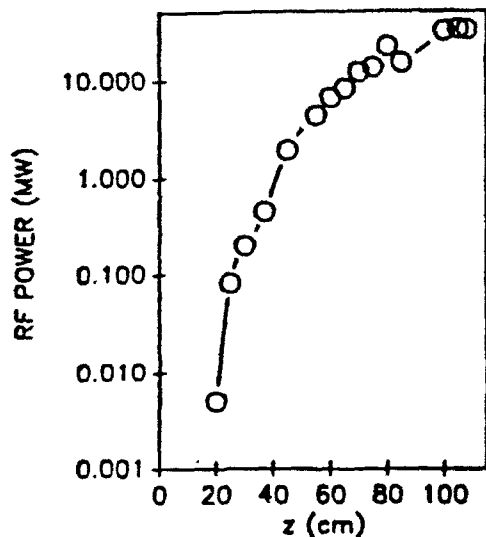


Fig.5 Power gain for the amplifier mode as a function of axial distance. Peak power is 33MW.

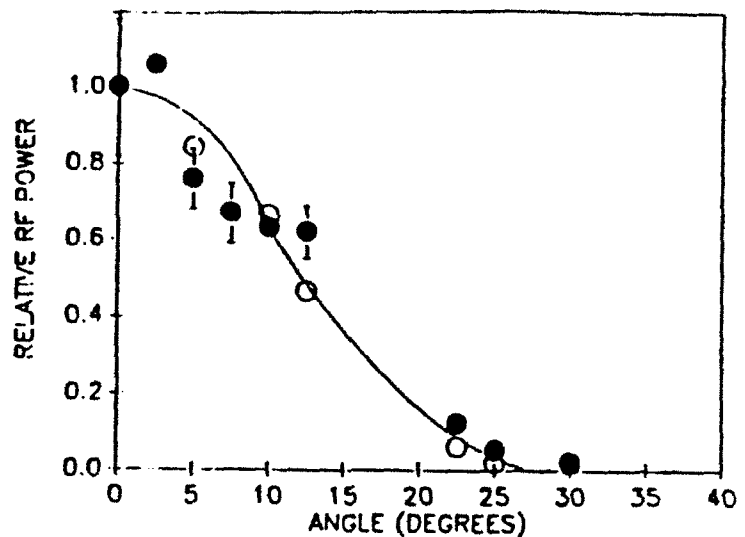


Fig.6 Angle scan for the amplifier configuration. Open circles are for the input magnetron signal alone.

Summary

We have reported our recent experimental results from our CARM amplifier experiments. We have redesigned the wiggler region so as to obtain a tighter beam with smaller transverse electron excursions and therefore more amenable to alignment in the beam transport system (the wiggler operates in the Type I electron orbit region).

The amplifier operates in the lowest TE_{11} waveguide mode, a fact confirmed by angular scans of the radiation pattern. The single pass, small signal gain is 65 dB/m. The saturated power output is 33 MW corresponding to a 7% electronic efficiency.

In the superradiant configuration, multimoding (same frequency, different wavenumber) seems to occur, as is suggested by the shape of the measured radiation pattern. The observed reduced growth rate (45 dB/m) relative to the amplifier configuration may be the result of this multimoding. It is noteworthy that a sufficiently powerful input signal in the amplifier configuration apparently suppresses multimoding.

Acknowledgments

This work was supported by the Air Force Office of Scientific Research and the Innovative Science and Technology Office of the Strategic Defense Initiative Organization. It was aided greatly by equipment on loan from the Lawrence Livermore National Laboratory and we gratefully acknowledge the help given us by B. D. Hopkins.

References

- [1] A.W. Fliflet, *Int. J. Electron.*, **61**, 1049-1080 (1986).
- [2] V.L. Bratman, N.S. Ginzburg, G.S. Nusinovich, M.I. Petelin and P.S. Strelkov, *Int. J. Electron.*, **51**, 541-567 (1981).
- [3] K.D. Pendergast, B.G. Danly, R.J. Temkin, and J.S. Wurtele, submitted to *IEEE Trans. Plasma Sci.*, April (1988).
- [4] A.T. Lin, *Int. J. Electron.*, **57**, 1097-1108 (1984).
- [5] B.G. Danly, K.D. Pendergast, R.J. Temkin, and J.A. Davies, *Proc. SPIE* **873**, (1988).
- [6] R.W. Twiss, *Aust. J. Phys.* **11**, 564 (1958).
- [7] J. Schneider, *Phys. Rev. Lett.* **2**, 504 (1959).
- [8] E. Ott and W.M. Manheimer, *IEEE Trans. Plasma Sci.* **25**, 1 (1975).
- [9] R.K. Chu and J.L. Hirshfeld, *Phys. Fluids* **21**, 461 (1978)
- [10] P. Sprangle and W.M. Manheimer, *Phys. Fluids* **18**, 224 (1975)
- [11] R.C. Davidson, and H.S. Uhm, *Phys. Fluids* **29**, 2713 (1986)
- [12] P. Sprangle and A.T. Drobot, *IEEE Trans. Microwave Theory Tech.* **25**, 528 (1977)
- [13] J.A. Davies, *Phys. Fluids B*, (1989).
- [14] A.T. Lin and C.C. Lin, *Int. J. Infrared Mill. Waves* **6**, 41 (1985).
- [15] I.E. Botvinnik, V.L. Bratman, A.B. Volkov, N.S. Ginzburg, C.G. Denisov, B.D. Kol'chugin, M.M. Ofitserov, and M.I. Petelin, *Pis'ma Zh. Eksp. Teor. Fiz.*, **35**, 418-420 (1982).
- [16] A. Di Rienzo, G. Bekefi, C. Leibovitch and B.G. Danly, *SPIE Proceedings*, **1061**, p. 338 (1989).
- [17] G. Bekefi, A. Di Rienzo, C. Leibovitch, and B.G. Danly, *Appl. Phys. Lett.* **54**, (14), (1989).
- [18] The technique is described by D. Proznitz and E.T. Scharlemann, Lawrence Livermore National Laboratory, ATA Note No. 229, Feb 22, 1984.

APPENDIX 2

PFC/JA-90-12

**Observations of Periodic Intensity Bursts
from a Free-Electron Laser Oscillator**

E. Jerby, G. Bekefi and J. S. Wurtele

April 1990

**Department of Physics
Research Laboratory of Electronics
and
Plasma Fusion Center**

**Massachusetts Institute of Technology
Cambridge, Massachusetts 02139 USA**

This work is supported in part by the National Science Foundation, the Air Force Office of Scientific Research and the Naval Research Laboratory. E.J. is supported by the Rothschild and Fulbright foundations.

Submitted for publication in Physical Review Letters.

Observations of Periodic Intensity Bursts from a Free-Electron Laser Oscillator

E. Jerby[†], G. Bekefi and J. S. Wurtele

Department of Physics
Research Laboratory of Electronics
and
Plasma Fusion Center

Massachusetts Institute of Technology
Cambridge, Massachusetts 02139

Abstract

Observations of periodic intensity bursts from a free-electron laser oscillator operating in the microwave regime are reported. Their periodic separation (~ 40 ns) equals the radiation round-trip time, and their width is approximately the slippage time (~ 2 -4 ns). Unlike previous studies, the bursts occur in the small signal regime, near oscillation threshold. The observations are compared with theoretical results from an impulse response model of the free-electron laser.

[†]Permanent address: Faculty of Engineering, Tel Aviv University, Ramat Aviv, 69978 Israel.

The study of the frequency spectrum and temporal evolution of electromagnetic pulses in lasers is a subject of considerable interest. In conventional atomic and molecular lasers short pulse phenomena have been known for many years. These include the nonlinear phenomenon of self (spontaneous) spiking¹ as well as a wide range of mode-locking mechanisms² and soliton formation.³

In free-electron laser (FEL) oscillators, radiation bursts, or spikes, as they are often called, have been studied experimentally and theoretically in the nonlinear regime by several groups.⁴⁻¹⁰ Their appearance comes about as a result of the FEL side-band instability caused by electron oscillations in the potential wells of the ponderomotive wave. In contrast, studies in this letter¹¹ deal with the build-up of short electromagnetic pulses well before saturation and near oscillation threshold, where linear phenomena dominate the interaction. The observed spikes have a temporal separation corresponding to the radiation transit time (~ 40 ns) in the cavity, and their widths (2-4 ns) are believed to correspond to the slippage time between the radiation pulses and the electron bunches. Each assembly of micropulses is contained within a well-defined "macropulse" of about $1\mu\text{s}$ duration. Although the macropulses occur at random times, their appearance is correlated with observed random current spikes in the electron beam.

Figure 1a shows a schematic of our experiment.¹² The accelerating potential is supplied by a Marx generator (Physics International Pulserad 615 MR). The electron beam is generated by a thermionically emitting, electrostatically focused, Pierce-type electron gun (250 kV, 250 A) from a SLAC klystron (Model 343). An emittance selector is used to limit the beam current to ~ 1 A. An assembly of focusing coils transports the electron beam into the rectangular stainless steel drift tube ($0.40'' \times 0.90''$), which also acts as the waveguide for the electromagnetic radiation. The beam is contained by a uniform 1.6 kG axial magnetic field produced by a solenoid.

A 65 period circularly polarized magnetic wiggler has a period $l_w = 3.5$ cm,

an amplitude $B_w = 200\text{--}400$ G, and is generated by bifilar conductors.^{12,13} Since an aperture limits the size of the electron beam to $r_b \simeq 0.07l_w$, the wiggler field appears nearly sinusoidal to the drifting electrons. At the wiggler entrance a slowly increasing field amplitude is produced by resistively loading the first six periods of the wiggler magnet.

The 2.7 m long drift tube acts as a rectangular waveguide whose fundamental TE_{10} mode has a cutoff frequency of 6.6 GHz. The drift tube closes upon itself and thereby forms a ring cavity 7.6 m in length (see Fig. 1a). The system is operated in a frequency range between 8 and 11 GHz. At those frequencies the empty waveguide can support only the fundamental (TE_{10}) mode, all higher modes being evanescent. The ring cavity loss is 5.5 dB. The single-pass FEL gain varies between 6 and 8.5 dB, so that the overall system gain is less than 3 dB. It is in this low net gain operating regime that all of our measurements are carried out, and where the periodic rf spikes are the clearest. In order to observe the rf spikes, the radiation field of the ring cavity is sampled by means of a 20 dB directional coupler and then measured with a calibrated crystal detector.

Figures 1b and 1c illustrate the time history of the beam energy and rf power as observed on an oscilloscope screen. Since our Marx accelerator has an RC droop with a 25 μs time constant, the electron beam energy sweeps through the range of values illustrated in Fig. 1b. Figure 1c shows that the overall rf pulse starts $\sim 7\mu\text{s}$ after the Marx ignition and lasts typically for 1 to 3 μs .

Expanding the oscilloscope time scale yields the observed micropulses shown in Fig. 2a. Placing a band pass filter (9.6-10.2 GHz) in the output arm of the directional coupler, reveals better the underlying micropulse structure, as illustrated in Fig. 2b. The filtered pulse is seen to be composed of a sequence of partially overlapping macropulses with random start-up times. Each macropulse consists of a series of micropulses within a bell-shaped macropulse envelope. The distance between two successive micropulses is 36 ns, which is the ring cavity round-trip time of a micropulse with a center frequency of $f_0 = 9.6$ GHz. The micropulse width is 2-4 ns, and no significant broadening is observed over many round-trips. Filtering the feedback signal by

a high-pass filter ($f > 9.6$ GHz.), installed in the return leg of the ring cavity (instead of filtering the sampled signal) leads to similar results.

As noted above, each of the overlapping macropulses starts at a random time. However, its appearance is correlated to spikes in the current density shown in Fig. 2c. The current density is measured by a tiny probe¹³ partially inserted within the electron stream and placed ~ 1 m from the beginning of the bifilar helical wiggler (Fig. 1a).

The simplified linear model of the FEL oscillator in the time domain discussed below takes into account both the statistical features of the electron beam and the FEL interaction. Random fluctuations of the electron beam initiate the oscillation process. They are described by a shot-noise model¹⁴⁻¹⁶ in which the density $n_i(t)$ is given by

$$n_i(t) = n_o + n_n \sum_i \delta(t - t_i), \quad (1a)$$

where t_i are random times distributed with a uniform density λ_e ; consequently $\delta(t - t_i)$ are Poisson impulses. The correlation function of $n_i(t)$ is therefore given by

$$R_n(\tau) = n_o^2 (\lambda_e^2 + \lambda_e \delta(\tau)). \quad (1b)$$

In what follows we apply the shot-noise model to the current spikes shown in Fig. 2c, i.e., to macroparticles rather than to single electrons. The average temporal density of the spikes is $\lambda_e \sim 5\mu s^{-1}$ as evaluated from experiments.

The FEL oscillator is modeled as a cascade of FEL blocks¹⁷ as shown in Fig. 3. Each stage l in the cascade represents one round-trip time τ_d , where D is a delay element equivalent to the feedback waveguide section. Each FEL block ($FEL^{(l)}$) has two inputs, one for the EM wave E_i , and the other for the electron beam density fluctuations n_i . Due to the voltage droop in the electron beam, each FEL block has different parameters determined by their instantaneous values at $t = l\tau_d$. We assume that these parameters are almost stationary during one round-trip. The round-trip period is updated in each round-trip according to the instantaneous center frequency

of the rf. Linear transfer functions define the relation between the output $\tilde{E}_o(\omega)$ and the two independent inputs, $\tilde{E}_i(\omega)$ and $\tilde{n}_i(\omega)$. These are given, in the frequency domain, for each FEL block (l) by

$$\tilde{E}_o(\omega)|_{n_i=0} = T_E^{(l)}(\omega)\tilde{E}_i(\omega) \quad (2a)$$

$$\tilde{E}_o(\omega)|_{E_i=0} = T_n^{(l)}(\omega)\tilde{n}_i(\omega). \quad (2b)$$

The transfer functions $T_E(\omega)$ and $T_n(\omega)$ are found from the gain-dispersion equations for the pre-bunched FEL.¹⁸

The response in the time domain of the FEL oscillator to a single density impulse, given by $n(t) = n_0 + n_n\delta(t)$ for $n\tau_d < t < (n+1)\tau_d$, is found by an inverse Fourier transform on the cascade transfer function

$$h_{osc}(t, t_1 = 0) = \frac{1}{2\pi} \int_{\omega} T_n^{(0)}(\omega) \prod_{l=1}^n T_E^{(l)}(\omega) e^{i\omega t} d\omega. \quad (3)$$

The intensity of the impulse response $|h_{osc}(t, t_1 = 0)|^2$ is computed for the parameters of the FEL used in the experiment and is shown plotted as a function of time in Fig. 4a. Figure 4b shows the corresponding frequency sweep due to the change in accelerator voltage shown in Fig. 1b. The first micropulse is the instantaneous response of the FEL to the electron beam impulse, and is essentially the time-domain representation of the FEL spontaneous emission induced by the density fluctuations. The width of the first micropulse is comparable with the FEL slippage time,¹⁹ $[(1/v_g) - (1/v_z)]L_w$, where v_g is the radiation group velocity, v_z is the axial electron beam velocity and L_w is the wiggler length. It is found both analytically and numerically that the tendency of the micropulse to broaden, due to the waveguide dispersion, is balanced by the FEL gain and phase shift. Consequently, the micropulse width is preserved in many round-trips. This confirms our experimental results, in which no significant micropulse broadening is observed.

The theoretically calculated impulse response intensity of the FEL oscillator shown in Fig. 4a is quite similar to the bell-shaped macropulses measured in the experiment, shown in Fig. 2b, as is the periodic micropulse structure.

In conclusion, we have reported what we believe are entirely new observations of an FEL operating near oscillation threshold. The observations show that the radiation field is composed of bursts with a periodic substructure correlated to bursts in the electron beam current. These studies may lead to a better understanding of the FEL oscillator start-up phase and to methods of generating very short, tunable micropulses in free electron lasers.

ACKNOWLEDGEMENTS

This work is supported in part by the National Science Foundation, the Air Force Office of Scientific Research and the Naval Research Laboratory. E. J. is supported by the Rothschild and the Fulbright foundations.

References

1. P. W. Smith, *IEEE J. Quantum Electron.*, **3**, 627, (1967).
2. —, *Proc. IEEE*, **58**, 1342 (1970); for recent studies on ultrafast laser phenomena, see the special issue of *IEEE J. Quantum Electron.*, **25** (1989).
3. L. F. Mollenauer and R. H. Stollen, *Opt. Lett.*, **9**, 13 (1984)
4. N. M. Kroll and M. N. Rosenbluth, in *Physics and Quantum Electronics* (Addison-Wesley, Reading, MA, 1980), Vol. 7, p. 147.
5. R. W. Warren, B. E. Newnam, and J. C. Goldstein, *IEEE J. Quantum Electron.*, **21**, 882, (1985).
6. J. Masud, T. C. Marshall, S. P. Schlesinger, and F. G. Yee, *Phys. Rev. Lett.*, **56**, 1567 (1986).
7. W. B. Colson, *Nucl. Instrum. Methods Phys. Res.*, **A250**, 168 (1986).
8. J. C. Goldstein, B. W. Newnam, R. W. Warren, and R. L. Sheffield, *Nucl. Instrum. Methods Phys. Res.*, **A250**, 4 (1986).
9. B. A. Richman, J. M. J. Madey, and E. Szarmes, *Phys. Rev. Lett.*, **63**, 1682 (1989).
10. J. W. Dodd and T. C. Marshall, Digest of the 11th Int. FEL Conf., Naples, Florida; IEEE-LEOS 1989, L. R. Elias and I. Kimel, Eds., p.56.
11. E. Jerby, J. S. Wurtele and G. Bekefi, *Bull. Am. Phys. Soc.*, **35**, 1026 (1990).
12. J. Fajans, G. Bekefi, Y. Z. Yin, and B. Lax, *Phys. Fluids*, **28**, 1995 (1985).

13. K. Xu, G. Bekefi, and C. Leibovitch, *Phys. Fluids*, **B1**, 2066 (1989), and references therein.
14. H. A. Haus, *IEEE J. Quantum Electron.*, **17**, 1427 (1981).
15. P. Sprangle, C. M. Tang, and I. Bernstein, *Physical Review A*, **28**, 2300 (1983).
16. K. J. Kim, *Phys. Rev. Lett.*, **57**, 1871 (1986).
17. A. Gover, H. Freund, V. L. Granatstein, J. H. McAdoo, and C. M. Tang, *Infrared and Millimeter Waves*, vol. 11, ch. 8, K. J. Button, Ed., New York, Academic, 1984.
18. I. Schnitzer and A. Gover, *Nucl. Instrum. Methods Phys. Res.*, **A237**, 124 (1985). For a 2D derivation of Eqs. (4a,b), see E. Jerby, "Angular Steering of the FEL Far-Field Radiation Beam," to be published in *Phys. Rev. A*.
19. R. Bonifacio, C. Maroli and N. Piovella, *Optics Communications* **68**, 369 (1988).

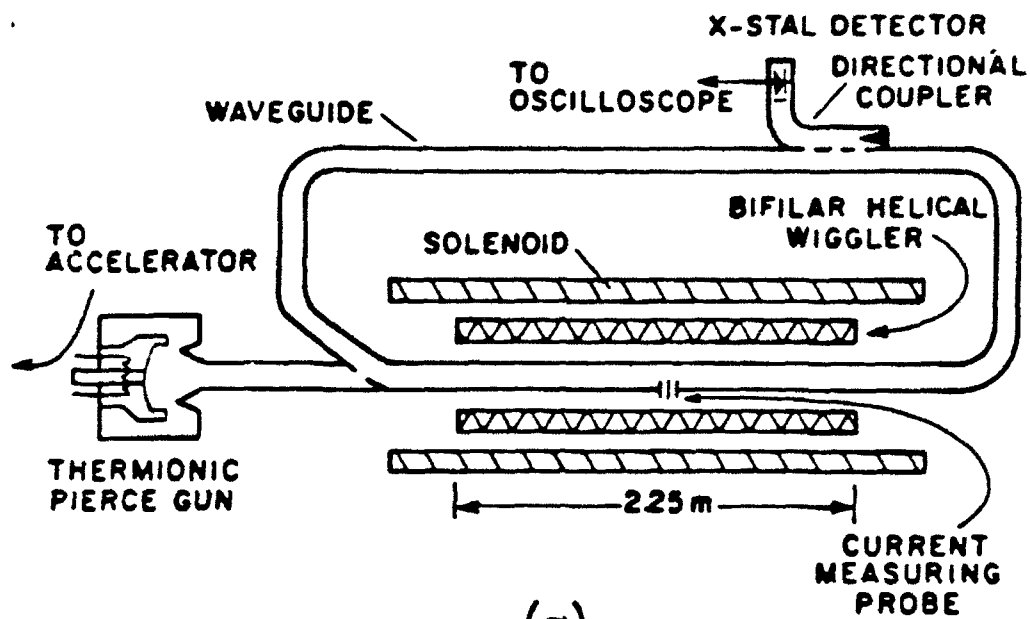
Figure Captions

Figure 1 (a) Experimental arrangement showing the ring cavity of the FEL oscillator; (b) and (c) are typical oscilloscope traces of the beam voltage and a radiation burst, respectively.

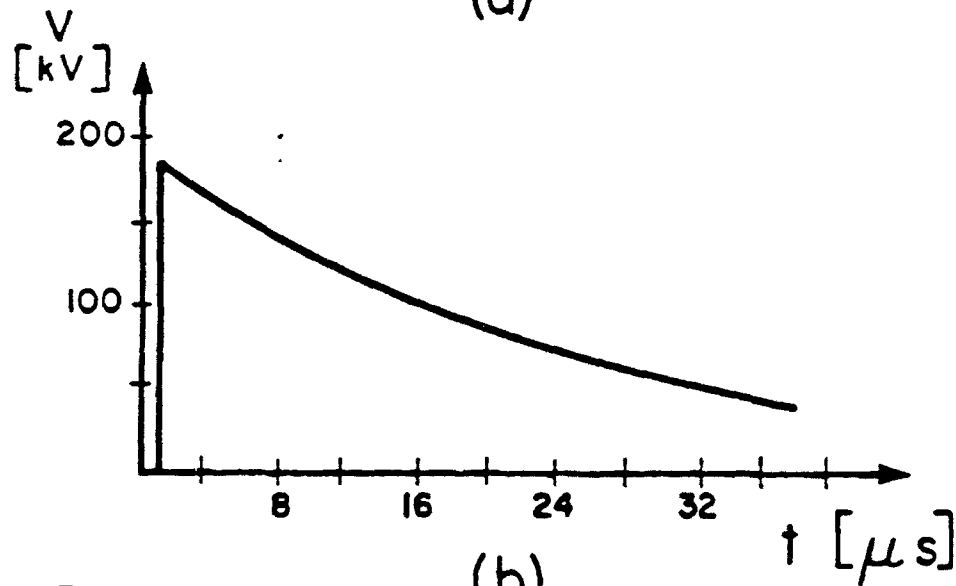
Figure 2 Expanded oscilloscope traces of typical radiation bursts before (a) and after (b) filtering (see text); (c) typical bursts in the electron beam current density.

Figure 3 Schematic of the computational model of the FEL oscillator.

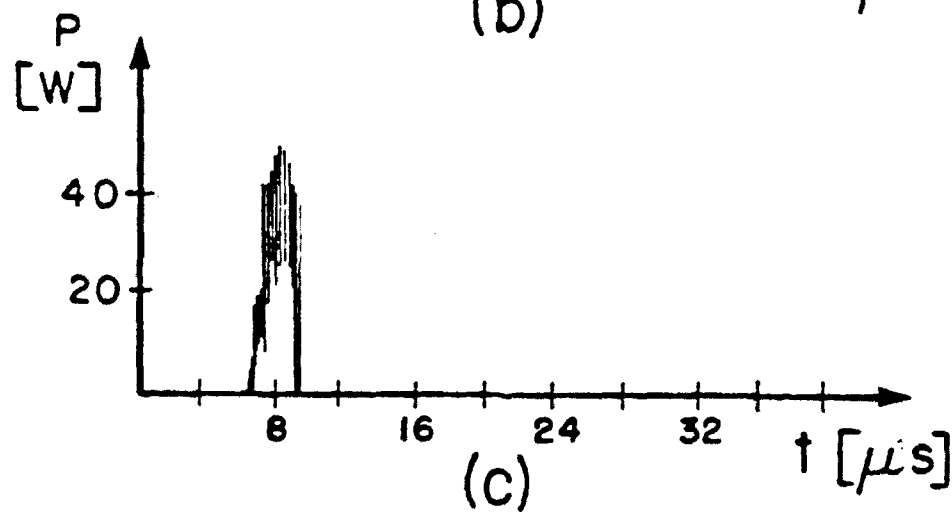
Figure 4 (a) The computed impulse response of the FEL oscillator (to be compared with the experimental result in Fig. 2b), and (b) the corresponding center frequency associated with each pulse.



(a)



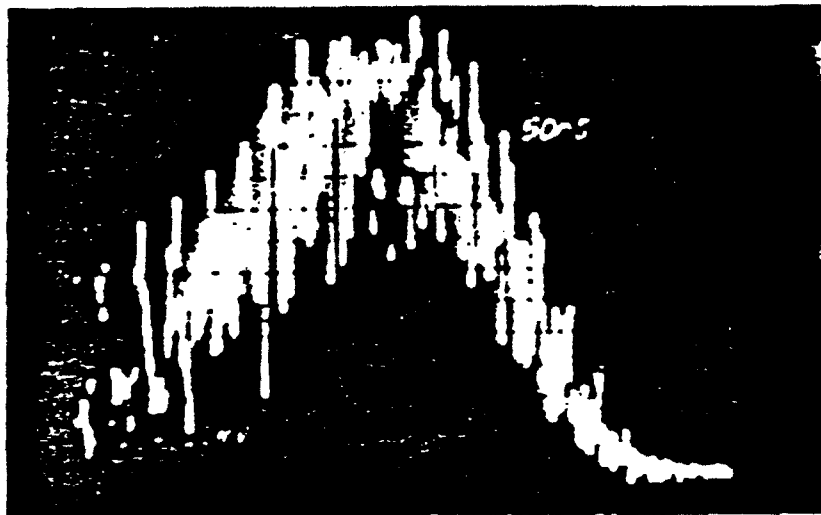
(b)



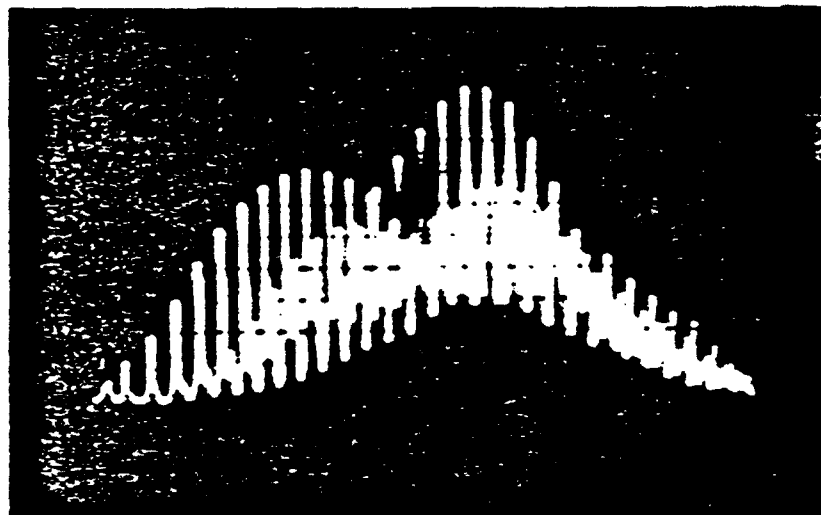
(c)

Fig.1 Jerby, Bekefi, Wurtele

intensity



intensity



current

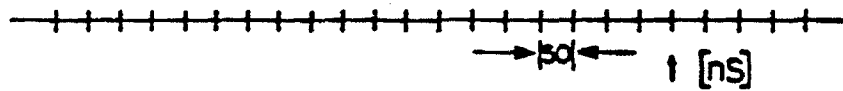
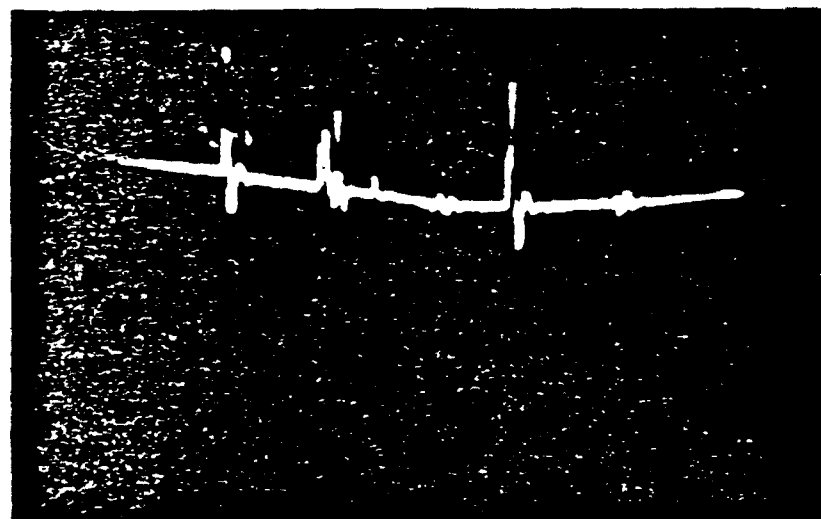


Fig.2 Jerby, Bekefi, Wurtele

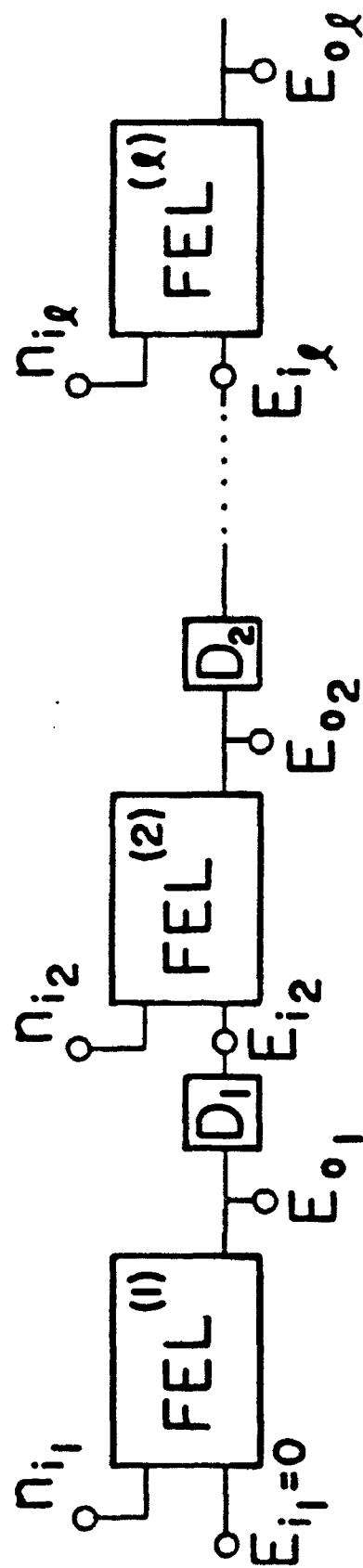


Fig.3 Jerby, Bekefi, Murtele

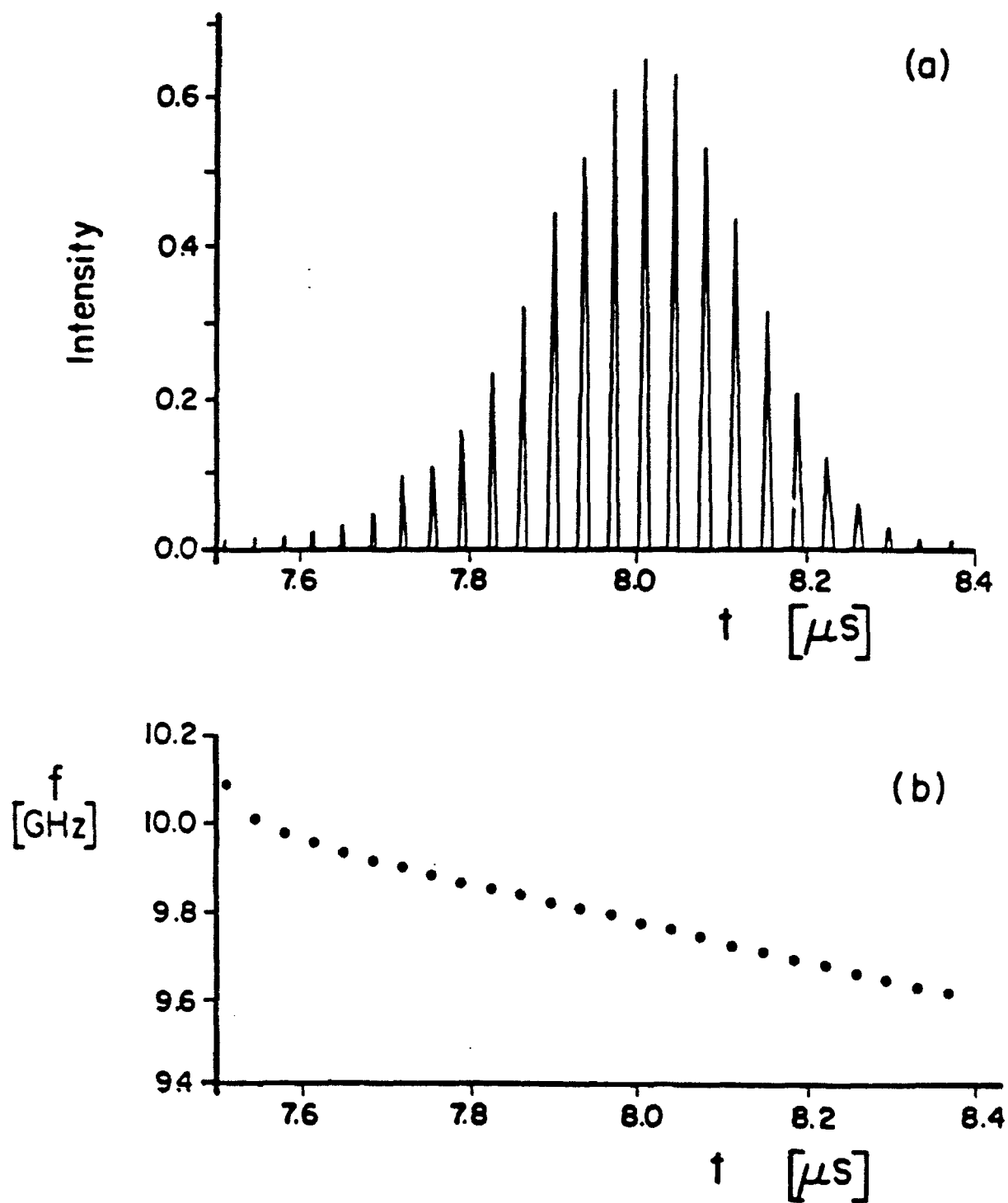


Fig.4 Jerby, Bekefi, Wurtele

PROJECT PERIOD
November 1, 1991 - December 31, 1992

Table of Contents

Project summary.....	131
The MIT 33.3 GHz high power laser with reversed guide magnetic field.....	132
Observations of periodic intensity bursts during the start-up phase of a free electron laser	142
Appendix.....	147

Project Summary

Microwave Emission from Relativistic Electron Beams represents a continuation proposal under the aegis of the AFOSR for the grant period November 1, 1991 to October 31, 1992.

The primary purpose of the research conducted under this grant is the experimental and theoretical study of novel coherent sources of millimeter wavelength radiation. During the forthcoming year we propose to concentrate on the following two research areas:

1. Further improvement of a novel high power FEL working in a regime that is hitherto been unexplored.
2. A continuation of our studies of the start-up phase of a FEL oscillator.

1. The MIT 33.3 GHz High Power Free Electron Laser with Reversed Guide Magnetic Field

As a result of an inadvertent mistake (serendipity?), we have discovered a new regime of FEL operation. Normally a FEL in the presence of a combined axial and wiggler magnetic field operates in a way in which the cyclotron motion of the electrons in the guide magnetic field reinforce the electron motion in the helical wiggler field. However, because of the forementioned error we have operated our FEL in a way in which the guide magnetic field opposes the wiggler field. In our so-called reverse wiggler configuration we have obtained unprecedented efficiency and high power output.

The experimental set-up is illustrated in Fig. 1, showing the position of the guide magnetic field, the wiggler field, and the microwave diagnostics. Table I gives a summary of the operating parameters. Table II lists the two conventional regimes of operation together with the reversed field operation. These three regimes are better understood by reference to Fig. 2 which represents a plot of the axial electron velocity as a function of the axial magnetic field. The solid dots show the regions of operation. Figs. 3, 4 and 5 illustrate the measured power output as a function of interaction length of the FEL wiggler.

It is noteworthy that the highest power (65 MW) and the highest efficiency (28%) were obtained in the reversed field configuration. The reason for this highly successful regime of operation remains as yet not understood. During the coming year we plan to do a detailed theoretical investigation together with appropriate three-dimensional simulations.

In addition to the power measurements, we have also carried out a detailed study of the spectral characteristics. The experimental set-up is illustrated in Fig. 6 and experimental results are shown in Fig. 7. We note that the radiation frequency is centered around 33.4 GHz and is very narrow-band (less than 80 MGz).

During the coming year we also plan to investigate in further detail the type II regime, in particular the negative mass regime of Freund and Ganguly.¹ Wiggler tapering for increased efficiency is also contemplated.

¹ A.K. Ganguly and H.P. Freund, IEEE Trans. Plasma Science, PS-16, 167 (1988).

SCHEMATIC OF THE EXPERIMENTAL SETUP

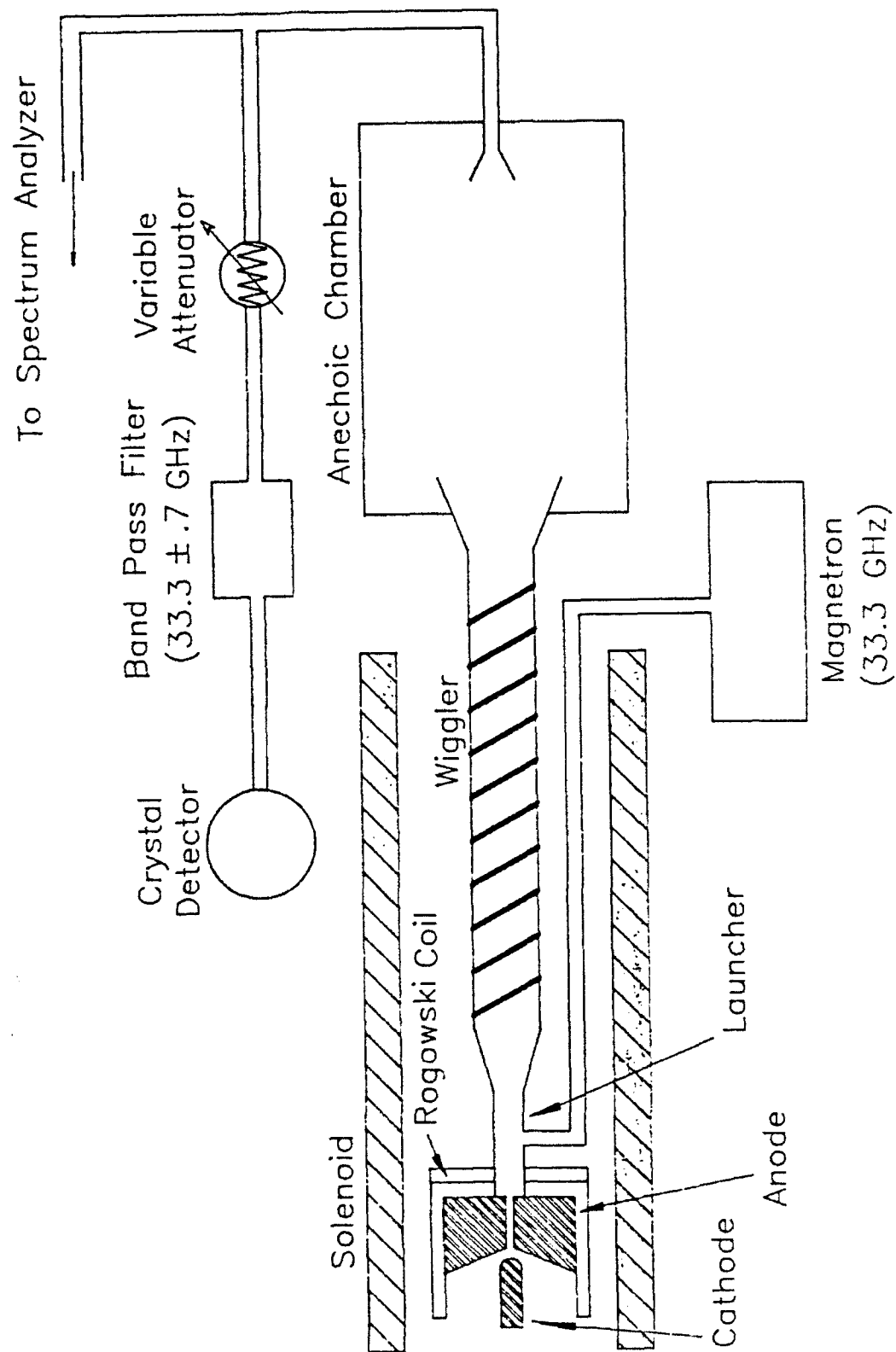


Figure 1

PARAMETERS OF FEL AMPLIFIER

FREQUENCY	33.38 GHz
BEAM ENERGY	800 keV
BEAM CURRENT	90 - 300 A
PULSE LENGTH	30 ns
RADIUS OF ELECTRON BEAM	0.25 cm
WAVEGUIDE RADIUS	0.51 cm
AXIAL MAGNETIC FIELD	4 - 11 kG
WIGGLER MAGNETIC FIELD	0.6 - 1.5 kG
WIGGLER PERIOD	3.18 cm
INPUT POWER	17 kW
OUTPUT POWER	65 MW
EFFICIENCY	28%

Table I

THREE DIFFERENT REGIMES OF OPERATION OF A FREE ELECTRON LASER AMPLIFIER:

- 1) PLACING THE ELECTRONS INTO GROUP I
ORBITS
- 2) PLACING THE ELECTRONS INTO GROUP II
ORBITS
- 3) REVERSING THE AXIAL GUIDE MAGNETIC
FIELD

CALCULATED IDEAL ORBITS

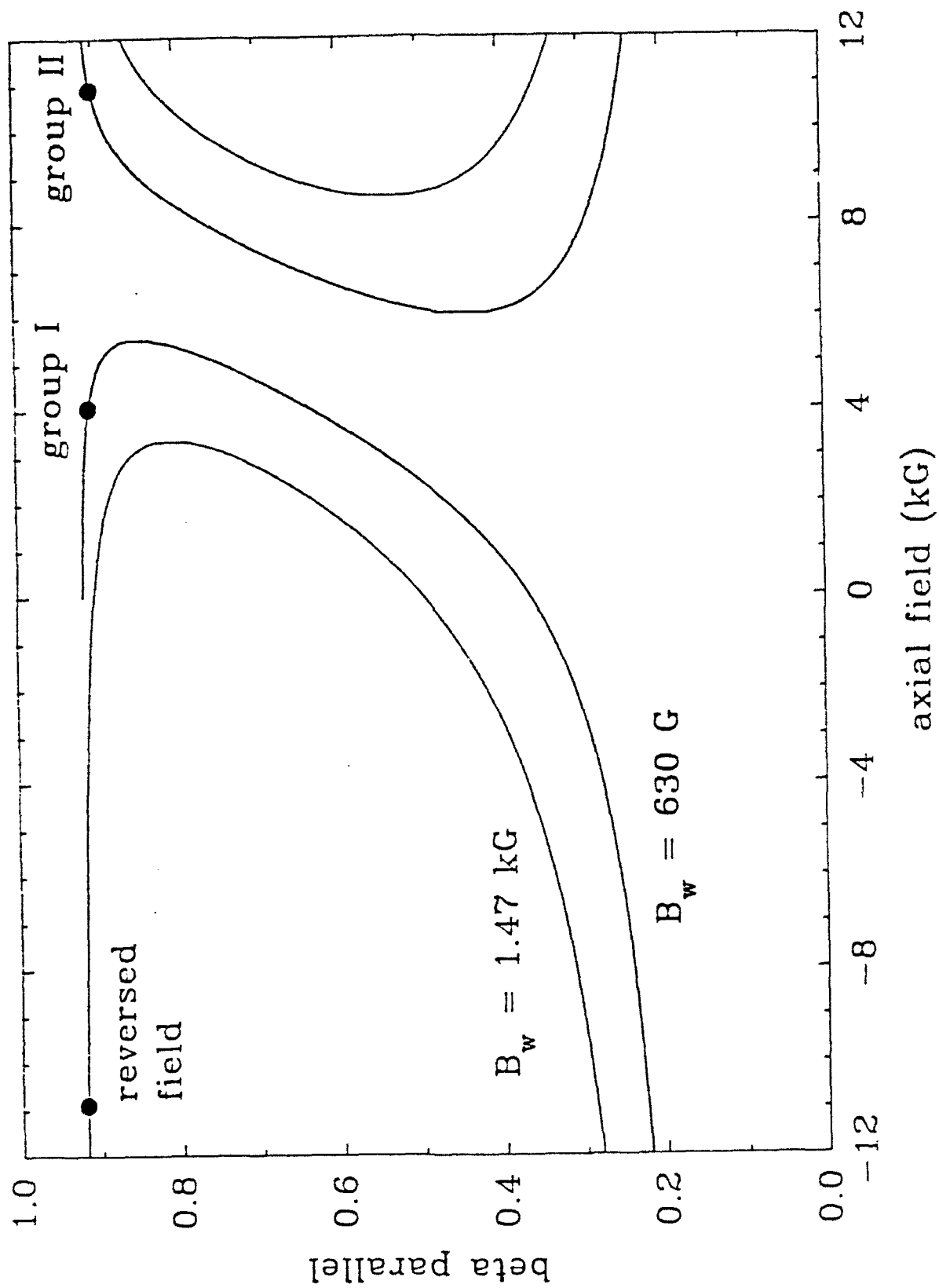


Figure 2

REVERSED FIELD — POWER vs. INTERACTION LENGTH

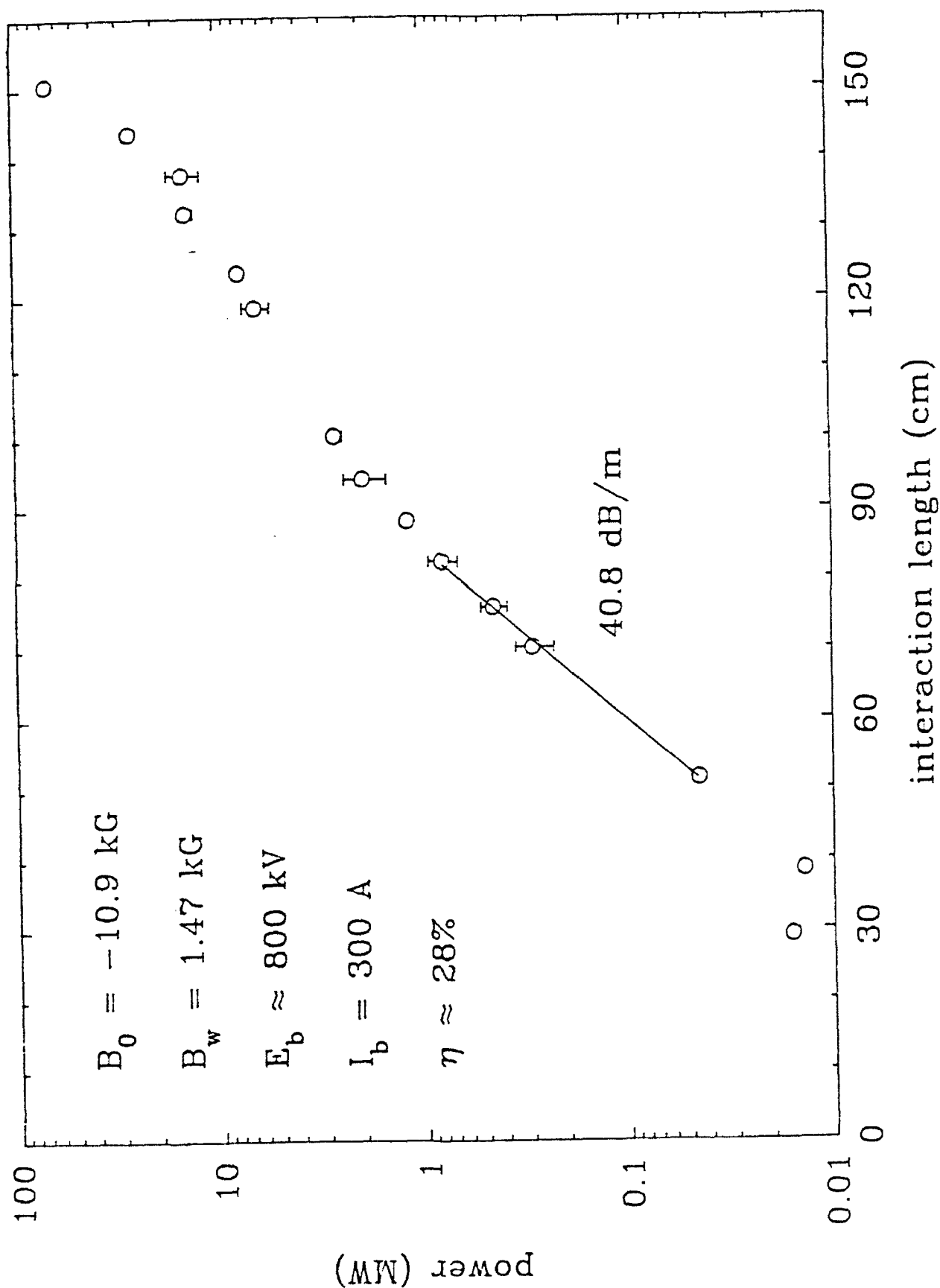


Figure 3

GROUP I -- POWER vs. INTERACTION LENGTH

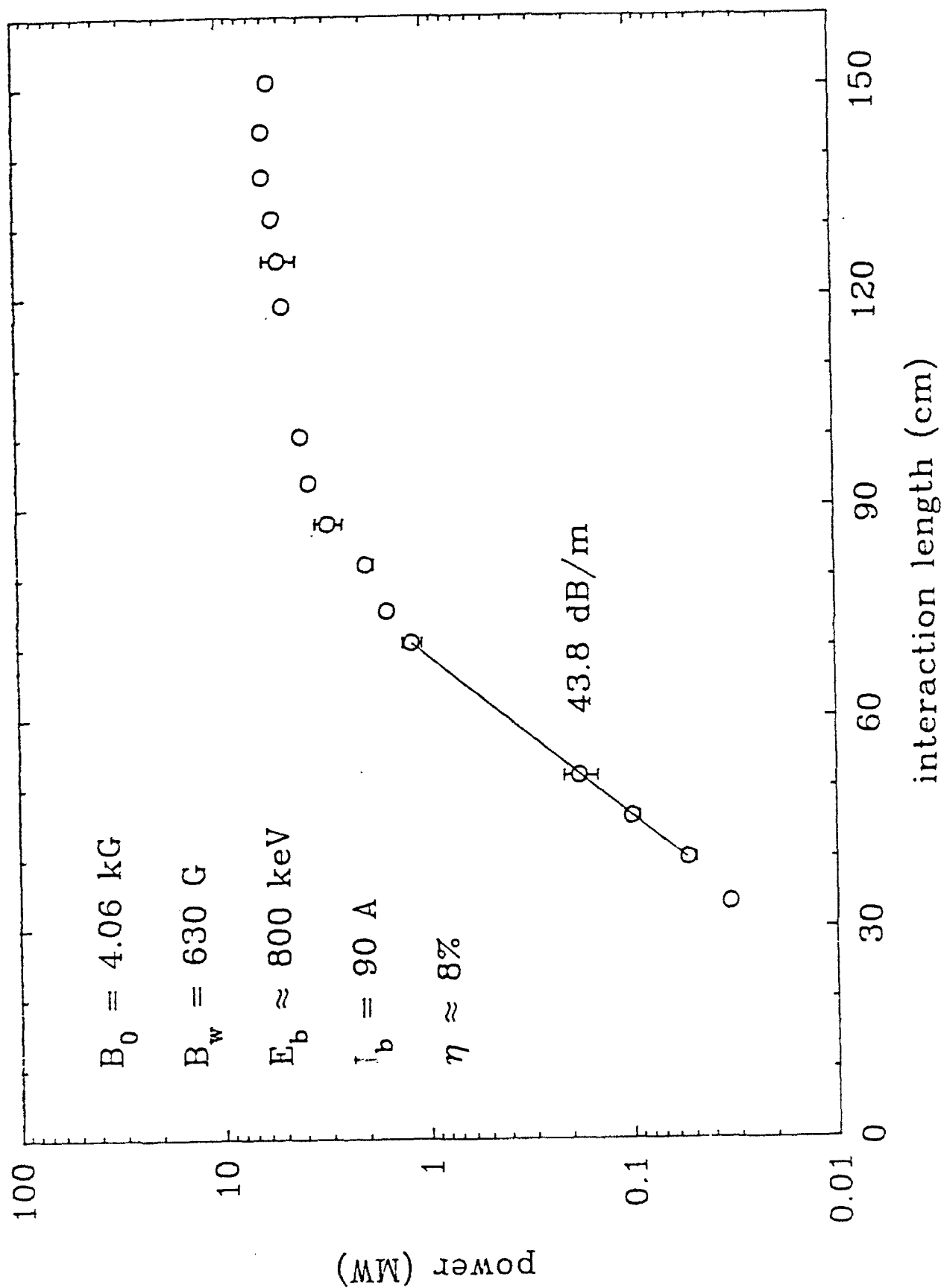


Figure 4

GROUP II - POWER vs. INTERACTION LENGTH

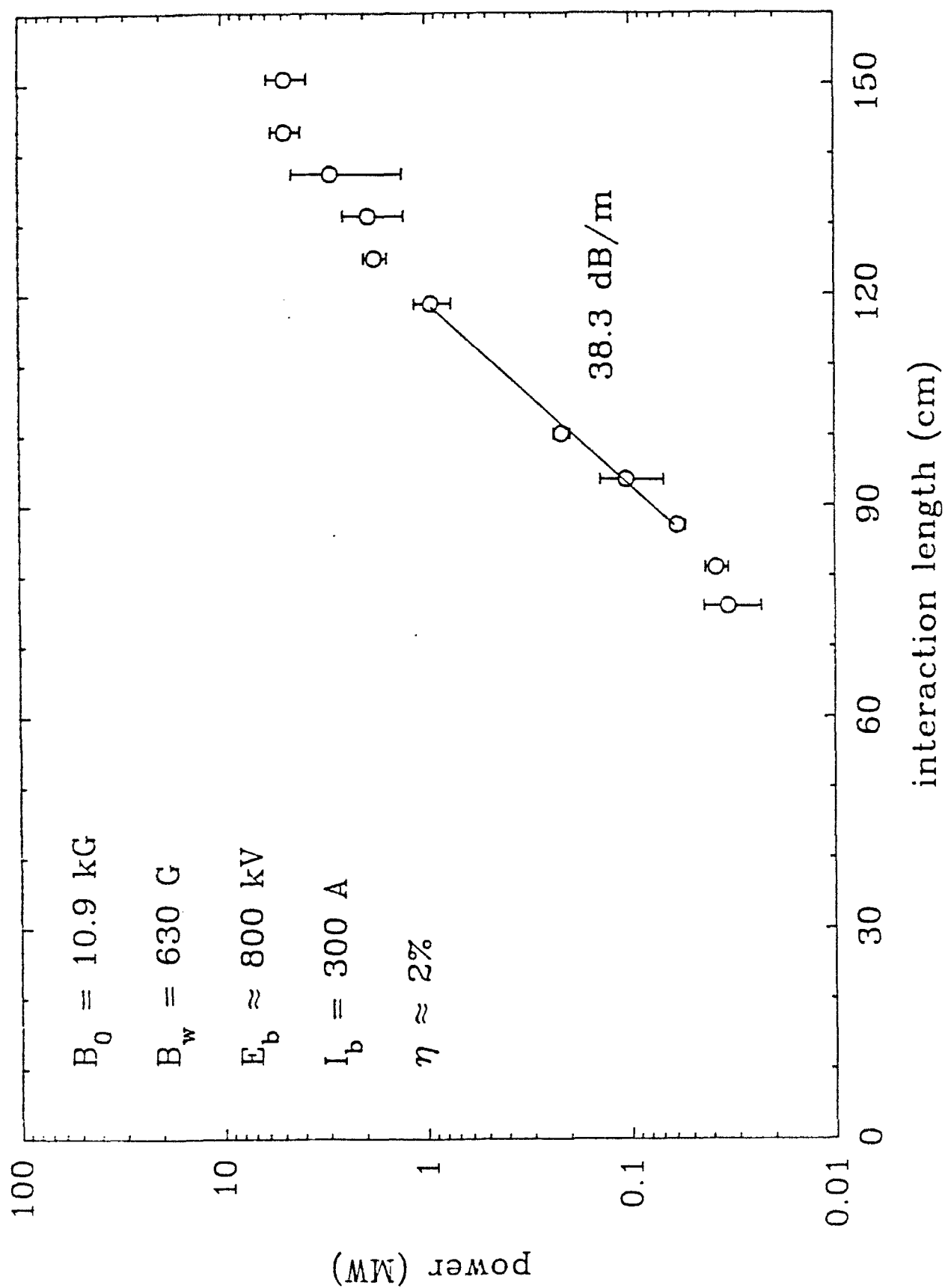


Figure 5

33.3 GHz Spectrum Analyzer

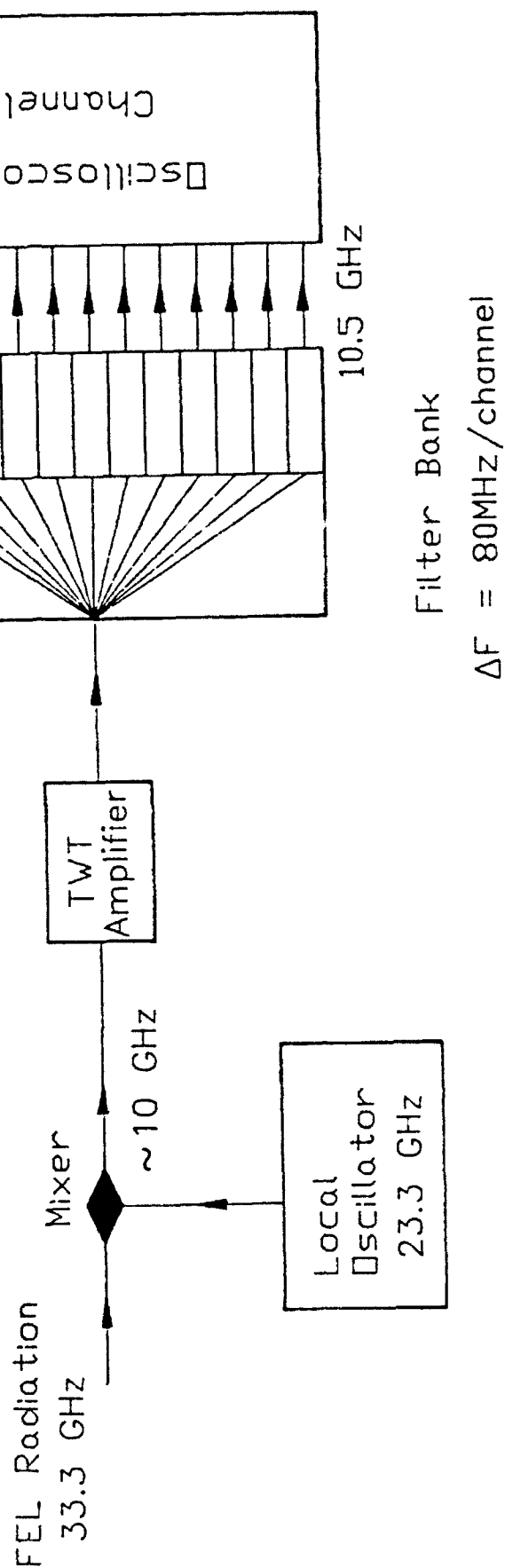


Figure 6

FREQUENCY SPECTRUM — Reversed Field Regime

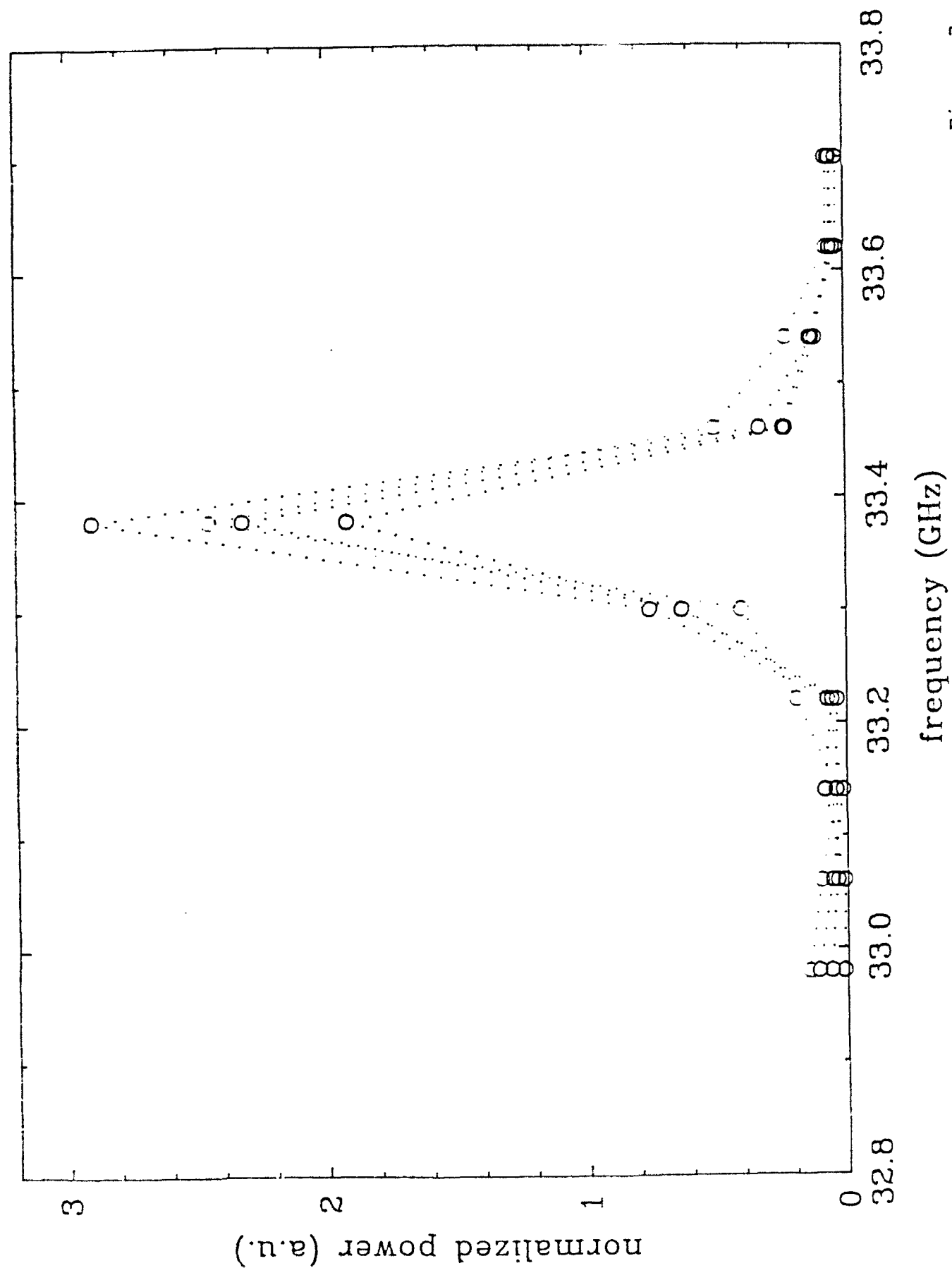


Figure 7

2. Observations of Periodic Intensity Bursts during the Start-Up Phase of a Free Electron Laser Oscillator

The study of the frequency spectrum and temporal evolution of electromagnetic pulses in lasers is a subject of considerable interest. In conventional atomic and molecular lasers short-pulse phenomena have been known for many years. These include the nonlinear phenomenon of self (spontaneous) spiking¹ as well as a wide range of mode-locking mechanisms² and soliton formation.³

In free electron laser (FEL) oscillators, radiation bursts, or spikes, as they are often called, have been studied experimentally and theoretically in the nonlinear regime by several groups.^{4,11} The appearance of bursts in this nonlinear FEL regime comes about as a result of the FEL sideband instability caused by electron oscillations in the potential wells of the ponderomotive wave.

In contrast, our studies deal with the buildup of short electromagnetic radiation bursts well before saturation and near oscillation threshold, where linear phenomena dominate the interaction. Here an observed radiation burst consists of periodic micropulses contained within a bell-shaped macropulse envelope. The start-up of the radiation macropulses are correlated with random current spikes superposed on a uniform current-density beam. The experimental observations agree with a theoretical linear model of the FEL impulse response in the time domain. The results shed light on start-up processes, mode locking, and micropulse formation in FEL oscillators.

Figure 8a shows a schematic of our experiment. The accelerating potential is supplied by a Marx generator (Physics International Pulserad 615 MR). The electron beam is generated by a thermionically emitting, electrostatically focused, Pierce-type electron gun (250 kV, 250 A) from a SLAC klystron (model 343). An emittance selector is used to limit the beam current to ~ 1 A. An assembly of focusing coils transports the electron beam into the rectangular stainless-steel drift tube (0.40" x 0.90"), which also acts as the waveguide for the electromagnetic radiation. The beam is contained by a uniform 1.6-kG axial magnetic field produced by a solenoid.

A 65-period circularly polarized magnetic wiggler has a period $l_w = 3.5$ cm, an amplitude $B_w = 200$ –400 G, and is generated by bifilar conductors.^{12, 13} Since an aperture limits the size of the electron beam to $r_b \sim 0.07 l_w$, the wiggler field appears nearly sinusoidal to the drifting electrons. At the wiggler entrance a slowly increasing field amplitude is produced by resistively loading the first six periods of the wiggler magnet.

The 2.7-m-long drift tube acts as a rectangular waveguide whose fundamental TE_{10} mode has a cutoff frequency of 6.6 GHz. The drift tube closes upon itself and thereby forms a ring cavity 7.6 m in length [see Fig.8]. The system is operated in a frequency range between 8 and 11 GHz. At those frequencies the empty waveguide can support only the fundamental (TE_{10}) mode, all higher modes being evanescent. The ring-cavity loss is 5.5 dB. The single-pass FEL gain varies between 6 and 8.5 dB, so that the overall system gain is less than 3 dB. It is in this low-net-gain operating regime that all of our measurements are carried out, and where the periodic rf spikes are the clearest. In order to observe the rf bursts, the radiation field of the ring cavity is sampled by means of a 20-dB directional coupler and a high-pass filter ($f > 9.6$ GHz), and then measured with a calibrated crystal detector.

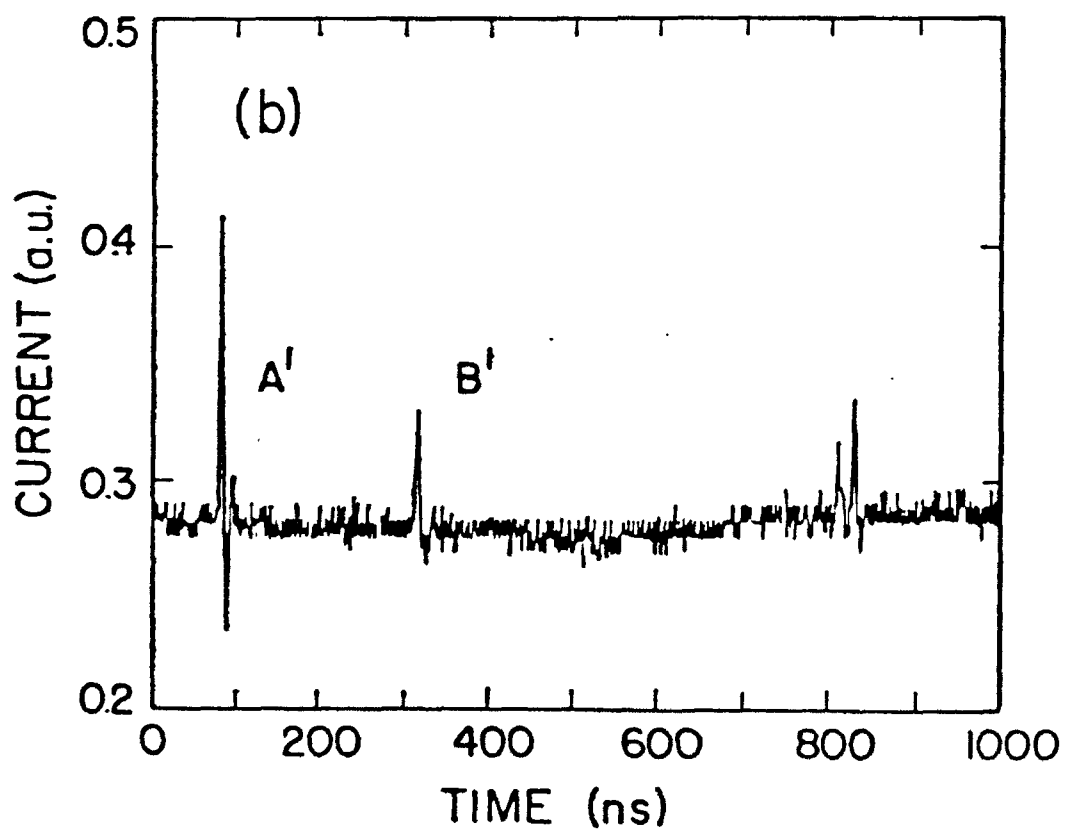
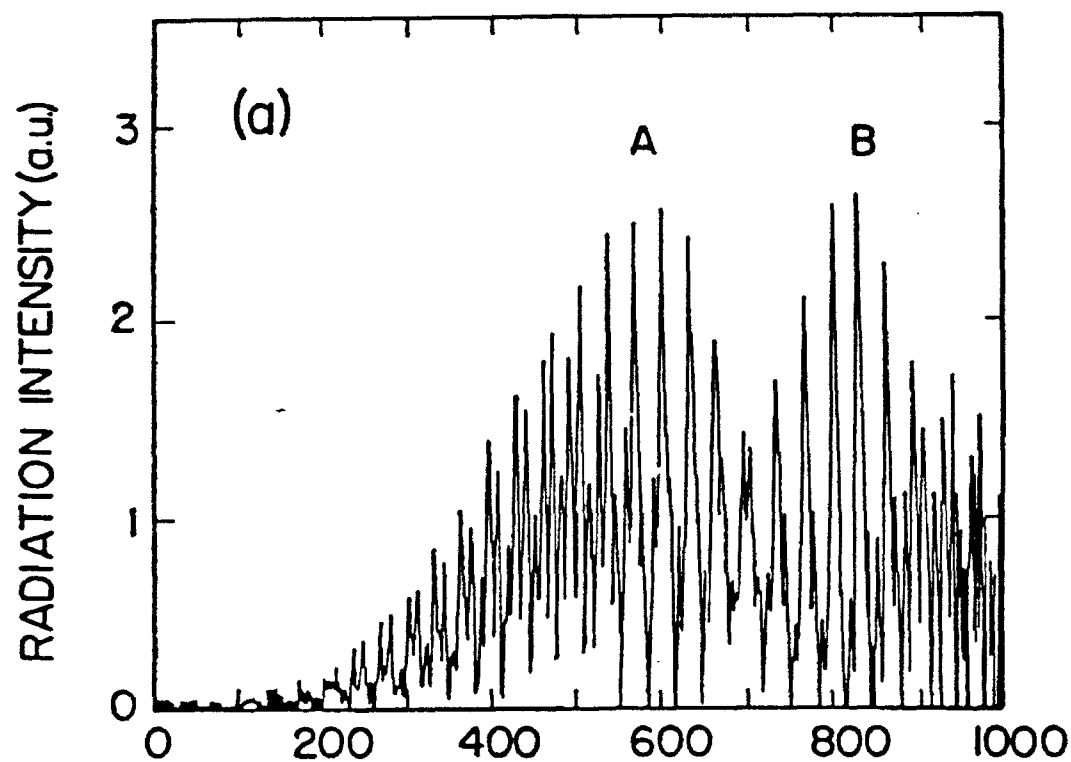
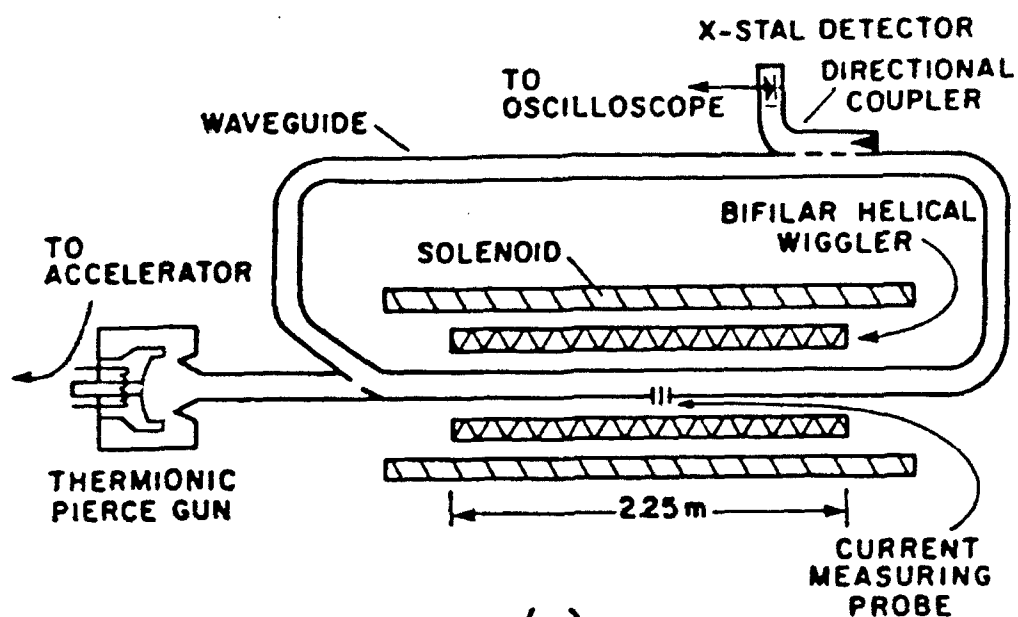
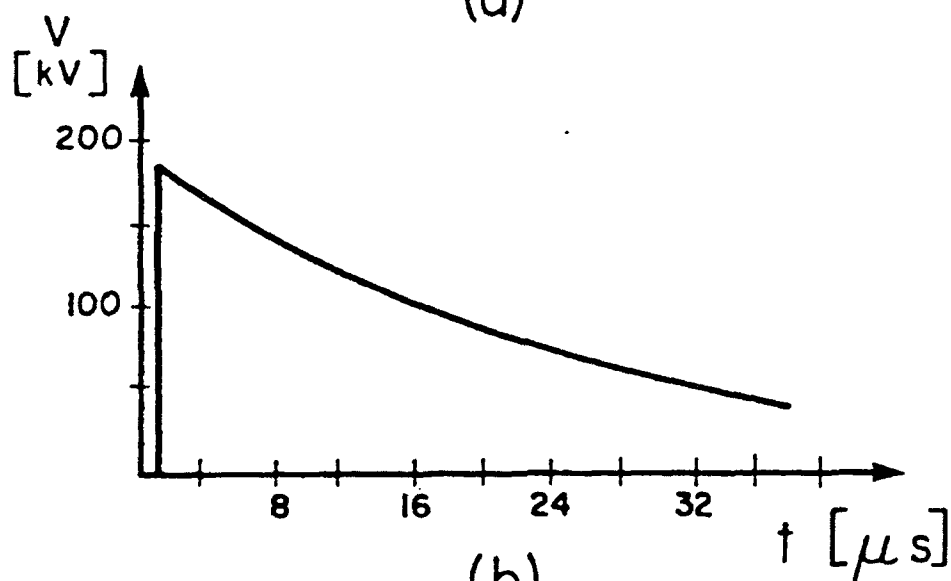


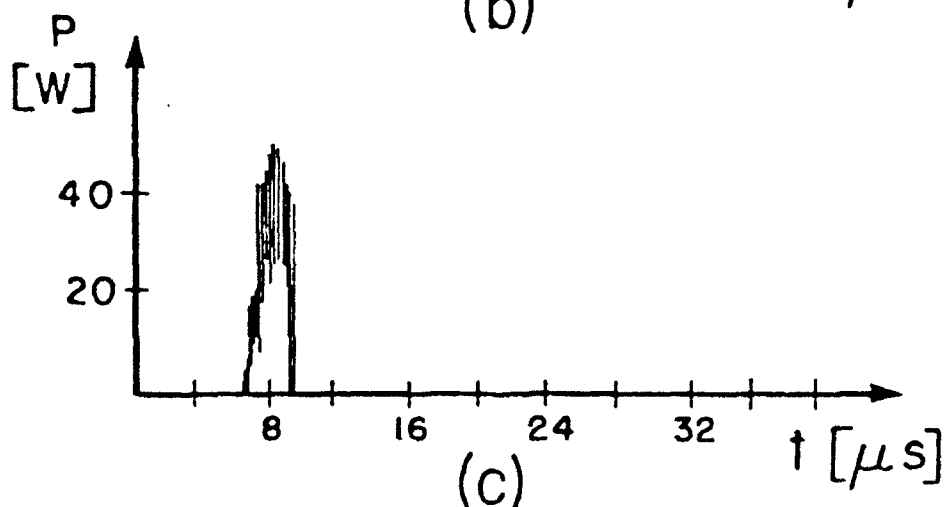
Figure 8



(a)



(b)



(c)

Figure 9

Figures 8(b) and 8(c) illustrate the time history of the beam energy and the rf power as observed on an oscilloscope screen. Since our Marx accelerator has an RC droop with a $25\text{-}\mu\text{s}$ time constant, the electron-beam energy sweeps through the range of values illustrated in Fig.8(b). Figure 8(c) shows that under these experimental conditions the overall rf bursts start $\sim 7\text{-}\mu\text{s}$ after the Marx ignition and last typically for 1-2 μs .

The radiation bursts and the electron-beam current are recorded simultaneously by a fast two-channel digital oscilloscope (LeCroy 7200, with 1-GHz sampling rate). The stored numerical data enable a precise analysis of the rf intensity and the current fluctuations, and of the correlation between these signals. Figure 9 shows a typical example of the radiation bursts on an expanded scale. Two dominant macropulses, marked as *A* and *B*, are clearly seen within partially overlapping bell-shaped envelopes. Each macropulse consists of a series of micropulses; the distance between two successive micropulses is 32 ns in macropulse *A*, and 34 ns in *B*. The micropulse width in both macropulses is 5.3 ns. Details of the experimental studies done to date will be found in Appendix 1.

During the coming year we propose to continue the above studies. In particular we shall concentrate on the question of the micropulse's width as it evolves within a given bell-shaped macropulse. Figure 10 shows the theoretical prediction of this evolution of the micropulse width. It represents a combination of pulse narrowing due to the active medium represented by the FEL and a pulse broadening due to waveguide dispersion. Convoluted in this development is also the question of the so called FEL slippage time. This is defined as $\tau_s = [(1/v_z) - (1/v_g)] L_w$ where v_z is the axial electron velocity, v_g is the radiation group velocity, and L_w is the wiggler length.

References

- ¹P.W. Smith, IEEE J. Quantum Electron. **3**, 627 (1967).
- ²P.W. Smith, Proc. IEEE **58**, 1342 (1970); for recent studies on ultrafast laser phenomena, see the special issue of IEEE J. Quantum Electron. **25** (1989).
- ³L.F. Mollenauer and R.H. Stollen, Opt. Lett. **9**, 13 (1984).
- ⁴N.M. Kroll and M.N. Rosenbluth, in *Physics and Quantum Electronics* (Addison-Wesley, Reading, MA, 1980), Vol. 7, p. 147.
- ⁵R.W. Warren, B.E. Newman, and J.C. Goldstein, IEEE J. Quantum Electron, **21**, 882 (1985).
- ⁶J. Masud, T.C. Marshall, S.P. Schlesinger, and F.G. Yee, Phys. Rev. Lett. **56**, 1567 (1986).
- ⁷W.B. Colson, Nucl. Instrum. Methods Phys. Res., Sect. A **250**, 168 (1986).
- ⁸J.C. Goldstein, B.W. Newman, R.W. Warren, and R.L. Sheffield, Nucl. Instrum. Methods Phys. Res. Sect. A **250**, 4 (1986).
- ⁹B.A. Richman, J.M.M. Madey, and E. Szarmes, Phys. Rev. Lett. **63**, 1582 (1989).
- ¹⁰J.W. Dodd and T.C. Marshall, in *Proceedings of the Eleventh International Conference on Free Electron Lasers, Naples, Florida*, edited by L.R. Elias and I. Kimel, FEL '89 Conference Digest (IEEE-LEOS, New York, 1989).
- ¹¹T. Kawamura, K. Toyoda, and M. Kawai, Appl. Phys. Lett., **51**, 795 (1987).
- ¹²J. Fajans, G. Bekefi, Y.Z. Tin and B. Lax, Phys. Fluids **28**, 1995 (1985).
- ¹³K. Xu, G. Bekefi, and C. Leibovitch, Phys. Fluids **B 1**, 2066 (1989), and references therein.

APPENDIX

Experimental and Theoretical Study of Periodic Intensity Bursts in the Start-up Phase of a Free-Electron Oscillator

E. Jerby[†], G. Bekefi, and J. S. Wurtele

April 13, 1991

Department of Physics, Research Laboratory of Electronics
and Plasma Fusion Center

Massachusetts Institute of Technology
Cambridge, Massachusetts 02139

Submitted to IEEE Journal of Quantum Electronics, Special Issue on Free-Electron Lasers

[†]Permanent address: Faculty of Engineering, Tel Aviv University, Ramat Aviv 69978, Israel.

Abstract

Experimental observations and a theoretical analysis of periodic radiation bursts and macropulse formation in the start-up phase of a free-electron laser (FEL) oscillator are presented. This microwave FEL uses a long pulse electron beam with a slowly decaying voltage. The output radiation consists of a superposition of bell-shaped macropulses, each of which is composed of a periodic sequence of short micropulses. The micropulses are separated by a cavity round-trip time. Each bell-shaped macropulse has a random start-up time and amplitude. The start-up of the radiation macropulses are correlated with random current spikes on the continuous electron beam. The observed macropulse signal agrees with a theoretical calculation of the impulse response of the FEL oscillator when the shift in the FEL resonance frequency arising from the slow voltage drop of the electron beam is included in the analysis. Possible applications of the macropulse formation phenomena in the FEL are discussed.

1 Introduction

This paper presents new experimental observations of the spontaneous excitation of periodic radiation bursts and macropulse formation in the start-up phase of a free-electron laser (FEL) oscillator. The radiation pulse consists of a superposition of bell-shaped macropulses each of which is composed of a sequence of short-pulse micropulses. The micropulses within a given macropulse are separated by a cavity round trip time. The amplitude of the micropulses has the bell-shaped macropulse structure. The structure of a macropulse, including micropulse width and separation and the bell-shaped envelope, is described by a linear model of the impulse response of the FEL oscillator.

Mechanisms of micropulse formation have been studied in a wide variety of fields, such as microwave tubes, conventional lasers and free electron lasers. In most cases micropulse formation is related to nonlinear phenomena, such as mode-locking or solitons. Narrow microwave pulses were produced in the early fifties with regenerative oscillators. One such short-pulse generator was constructed as a closed loop of a travelling wave tube (TWT) amplifier, a filter, and a nonlinear pulse expander [1]. It produced microwave micropulses of ~ 2 ns width. Short pulse phenomena in conventional atomic and molecular lasers have been studied intensively in the last two decades. These include the nonlinear phenomenon of self (spontaneous) spiking [2], as well as a wide range of mode-locking mechanisms [3] and soliton formation [4].

In free electron lasers, radiation bursts, or spikes, as they are often called, have been studied experimentally and theoretically in the nonlinear regime by several groups [5]-[11]. The appearance of radiation spikes in the FEL nonlinear regime is caused by the sideband instability which, in turn, is driven by electron oscillations in the potential well of the ponderomotive wave. In contrast, our studies [13] deal with the build-up of short electromagnetic radiation bursts that occur well before saturation and near oscillation threshold, where linear phenomena dominate the interaction.

Numerous theoretical and experimental investigations of phenomena related to radiation bursts are found in the literature. These include studies of noise in FEL amplifiers [14], spontaneous emission and coherence build-up [15], self amplification of spontaneous emission [16], prebunching [17,18], slippage and superradiance [19,20], effects of electron

energy drift [21], mode competition [22], phase-locking [23], spectral analysis [24] and pulse compression [25].

This paper is organized as follows: In section 2 we describe the experimental system and results. In section 3, we utilize the linear analysis of the prebunched FEL amplifier to evaluate the impulse response of a multipass FEL oscillator. The model includes the slow voltage droop on the electron beam, and the competition of waveguide losses and dispersion with FEL gain and dispersion. The radiation from an initially localized density perturbation, calculated in the time domain over many passes through the wiggler, agrees with the experimentally observed macropulse structure. A discussion of the macropulse formation in FEL oscillators and some possible applications is presented in section 4. A list of symbols appears in Appendix A.

2 The FEL Oscillator Experiment

The microwave FEL oscillator in this experiment employs a long pulse, low-energy electron beam regime. In its start-up phase, the oscillator emits periodic short rf micropulses in bell-shaped envelopes. The experimental apparatus is described in Section 2.1, and the experimental observations are presented in Section 2.2.

2.1 Experimental Configuration

The FEL oscillator is shown schematically in Fig. 1. A microwave FEL amplifier [24,25] was converted to operate as an FEL oscillator by eliminating the input signal and feeding the microwave output power back to the wiggler entrance.

The accelerating potential is supplied by a Marx generator (Physics International Pulserad 615 MR) without a pulse forming network. The potential decays exponentially, due to the Marx RC droop, as

$$V_{eb}(t) = V_0 \exp(-t/\tau_m), \quad (1)$$

where $V_0 \cong 0.2$ MV is the initial ($t = 0$) Marx voltage and $\tau_m \cong 25\mu\text{s}$ is the time constant of the Marx RC circuit.

The electron beam is generated by a thermionically emitting, electrostatically focused, Pierce-type electron gun (250 kV, 250 A) from a SLAC klystron (Model 343). An emittance selector limits the beam current to ~ 1 A.

The electron beam is transported into the rectangular stainless steel drift tube by an assembly of focusing coils. The beam is confined in the FEL region by a uniform 1.6 kG axial magnetic field produced by a solenoid and FEL coupling is provided by a bifilar helical wiggler. The wiggler has period $\lambda_w = 3.5$ cm, field amplitude $B_w = 200$ -400 G and a length of 65 periods. An aperture limits the size of the electron beam to $r_b \cong 0.07\lambda_w$, so that the wiggler field appears nearly sinusoidal to the drifting electrons. At the wiggler entrance a slowly increasing field amplitude taper is produced by resistively loading the first six periods of the wiggler.

The 2.7 m long drift tube acts as a rectangular waveguide for the electromagnetic radiation. Its inner dimensions are $0.90'' \times 0.40''$; the fundamental TE_{10} mode then has a cutoff frequency of 6.6 GHz. The waveguide closes upon itself, thereby forming a ring cavity 7.6 m in length, as shown in Fig. 1. The system is operated in a frequency range between 8 and 11 GHz. At these frequencies the empty waveguide can support only the fundamental (TE_{10}) mode, all higher modes being evanescent. The ring cavity loss is 5.5 dB and the single-pass FEL gain varies between 6 and 8.5 dB, so that the overall system gain is less than 3 dB. It is in this low net gain operating regime, where the periodic rf spikes are the clearest, that all of our measurements are carried out.

The radiation field in the ring cavity is sampled by means of a 20 dB directional coupler. In some of our measurements the sampled signal passes through a band-pass filter (9.6-10.2 GHz) or by a high-pass filter (9.6 GHz). The radiation power is measured with a calibrated crystal detector.

2.2 Experimental Observations

The FEL oscillator emits bursts of microwave radiation. Fig. 2a shows the full rf signal during one shot, and Fig. 2b shows, on the same time scale as Fig. 2a, the Marx potential droop. In this experiment the bursts start typically $\sim 7\mu\text{s}$ after the Marx ignition and they completely disappear $\sim 9\mu\text{s}$ after the Marx ignition.

Figure 3 shows a more detailed look at typical radiation bursts. The pulse appears noisy and irregular, though some periodic structures can be identified. The underlying temporal structure is revealed by filtering the microwave with a band-pass filter placed in the output arm of the directional coupler. Figure 4 shows radiation bursts detected through a 9.6-10.2 GHz band-pass filter. The filtered pulse is seen to be composed of a sequence of partially overlapping bell-shaped macropulses with random start-up times and amplitudes. Each macropulse consists of a series of micropulses within a macropulse envelope. The micropulse width (FWHM) is ~ 5 ns, and no significant broadening is observed over many roundtrips. The distance between two successive micropulses in Fig. 4 is ~ 36 ns. This period is the roundtrip time of a rf micropulse with a center frequency of $f_0 \cong 9.6$ GHz in the 7.6 m ring cavity. Increasing the cavity length to 11.3 m results in a similar bell-shaped macropulses with a longer period (51 ns) between the micropulses. The (51 ns) micropulse period is in agreement with the rf roundtrip time in the 11.3 m cavity.

In all the runs performed (totalling over 100), the bell-shaped macropulse is observed to be the underlying building block of the radiation bursts. The RF bursts appear to be composed of a sequence of partially overlapping bell-shaped macropulses with random start-up times and random amplitudes. The macropulses are most easily observed when the FEL is operated just above threshold. As the gain is increased, the density of macropulses increases and individual macropulses are harder to distinguish. For fixed system parameters, macropulses in a burst varies randomly from one run to another. The separation of the micropulses within each macropulse corresponds to the cavity roundtrip time of an rf pulse at the FEL resonance frequency, as determined (at the instantaneous electron beam energy). Similar bell-shaped macropulses are observed by filtering the feedback signal in the return leg of the ring cavity instead of filtering the output signal.

We found that the random start-up times of the macropulses and their appearance are correlated to spikes in the current density. Fig. 5 shows the electron beam current density measured by a tiny probe [26] which is partially inserted into the electron beam. The probe is placed ~ 1 m from the beginning of the wiggler. The random current spikes are clearly seen superposed on the dc current. The width of the current spikes (FWHM), measured by a fast transient recorder (Tektronix SCD 1000) was found to be typically narrower than 1 ns.

The radiation bursts and the electron beam current were recorded simultaneously using a LeCroy 7200 two-channel digital oscilloscope with 1 GHz sampling rate. The stored data enables a detailed analysis of the RF intensity, the current fluctuations, and any correlations between their temporal structures. In these measurements, in order to reduce the micropulse broadening, we used a high-pass filter ($f > 9.6$ GHz) to reject low frequency signals, instead of a band-pass filter.

Figure 6a shows a typical example of the radiation bursts in an expanded scale. Two dominant macropulses, marked as A and B, are clearly seen with partially overlapping bell-shaped envelopes. Each macropulse consists of a series of micropulses. The micropulse period is 32 ns in macropulse A, and 34 ns in B. The micropulse width in both macropulses in Fig. 6a is ~ 5 ns, and no significant broadening is observed in successive round-trips.

Figure 6b shows the simultaneous envelope of the electron beam current and the random spikes associated with it on the same time scale as Fig. 6a. The first two current spikes are marked in Fig. 6b as A' and B'. The distance between the current spike A' and the peak points of the macropulses A is 516 ns, and the distance between the current spike B' and the peak points of the macropulses B is 510 ns. The relation between these current spikes and the radiation pulses in Fig. 6a is examined in the next sections.

3 A Time Domain Analysis of the FEL Oscillator

The periodic radiation bursts and macropulse formation in an FEL oscillator presented in the previous section are observed well before saturation, i.e., in the small signal regime. Therefore, we can apply a small-signal linear theory to analyze these phenomena. In Section 3.1 we review the linear model of the prebunched FEL amplifier in the frequency and time domains. In section 3.2 we extend the model to describe the FEL oscillator in the time domain. The impulse response of the FEL oscillator is computed and compared to the rf macropulses observed in the experiment.

3.1 Amplification, Prebunching, and Spontaneous Emission

The FEL emits electromagnetic radiation by various mechanisms, such as the spontaneous emission [15], the signal amplification [27], the prebunched electron beam [17,18], and the self amplification of spontaneous emission [16]. These mechanisms can be distinguished by the source of excitation which initiates the radiation. In the amplification process, the FEL radiation is stimulated by the injection of an input field at the same frequency. The prebunched FEL is excited by an initial modulation of the electron beam distribution at the signal frequency. In the spontaneous emission process, the FEL emission of radiation is induced by random velocity and density fluctuations in the electron beam. These noise sources spread on a wide spectrum, including the FEL resonance frequency band in which the FEL radiation is excited. All these effects are described by similar transfer functions which relate the FEL output radiation to the excitation sources; the input field and the non-uniform electron beam distribution at the entrance.

In the FEL amplification process, the relation between the output field, $\tilde{E}_o(i\delta k, \omega)$, and the input field, $\tilde{E}_i(\omega)$, is given, for a cold beam, in wavenumber-frequency space, by the gain-dispersion equation [27,28]:

$$\tilde{E}_o(i\delta k, \omega) = \frac{(\delta k - \theta)^2 - \theta_p^2}{i\delta k[(\delta k - \theta)^2 - \theta_p^2] + i\kappa\theta_p^2} \tilde{E}_i(\omega), \quad (2)$$

where δk is the complex modification of the electromagnetic wave wavenumber due to the

FEL interaction, and $s = ik_z + i\delta k$ is the Laplace transform variable, $\bar{a}(s) = L\{a(z)\} = \int_z a(z)e^{-sz}dz$.

The FEL parameters θ_p , κ , and $\bar{\theta}$ are easily related to physical quantities. The space-charge parameter, θ_p , is

$$\theta_p = \sqrt{\frac{e\rho_0}{\gamma\gamma_z^2\epsilon_0 m V_z^2}}, \quad (3)$$

the coupling parameter, κ , and the gain parameter, Q , are

$$\kappa = \frac{1}{4} \frac{\omega}{V_z} \left(\frac{\bar{V}_\perp}{c} \right)^2, \quad Q = \kappa \theta_p^2, \quad (4a, b)$$

and the detuning parameter $\bar{\theta}$ is defined by

$$\bar{\theta} = \theta L_w = \left(\frac{\omega}{V_z} - k_z - k_w \right) L_w. \quad (5)$$

In the process of spontaneous emission and for initial prebunching of the electron beam, the FEL output field is excited by an initially nonuniform electron beam distribution. The relations between the output field, $\tilde{E}_o(i\delta k, \omega)$, and the ac input density component $\tilde{n}_i(\omega)$ and velocity component, $\tilde{v}_i(\omega)$, are given [17,29] by

$$\tilde{E}_o(i\delta k, \omega) = j\alpha_n \frac{(\delta k - \theta)}{D(i\delta k, \omega)} \tilde{n}_i(\omega), \quad (6a)$$

and

$$\tilde{E}_o(i\delta k, \omega) = -j\alpha_v \frac{(k_z + k_w)}{D(i\delta k, \omega)} \tilde{v}_i(\omega), \quad (6b)$$

respectively, where the coefficients α_n and α_v are

$$\alpha_n = \frac{1}{4} e Z_0 V_\perp, \quad \alpha_v = \frac{1}{4} \rho_0 Z_0 \frac{V_\perp}{V_z}, \quad (7a, b)$$

and $D(i\delta k, \omega)$ is the denominator of Eq. (2),

$$D(i\delta k, \omega) = i\delta k[(\delta k - \theta)^2 - \theta_p^2] + i\kappa\theta_p^2. \quad (8)$$

Eqs. (6a, b) apply to a prebunched electron beam in which the ac components $\tilde{n}_i(\omega)$ and $\tilde{v}_i(\omega)$ are at the same frequency as the rf output signal. These relations can be extended to describe shot-noise and other types of random fluctuations in which the

electron beam distribution is defined by statistical features such as its spectral power density.

The FEL transfer functions (2, 6a, b) are given in the Laplace-Fourier space ($i\delta k, \omega$). In order to find the spectral transfer functions of the FEL interaction between the FEL output radiation $\tilde{E}_o(\omega)$ at the wiggler exit $z = L_w$, and each of the input excitations $\tilde{E}_i(\omega)$, $\tilde{n}_i(\omega)$, and $\tilde{v}_i(\omega)$ at $z = 0$, we perform an inverse Laplace transform on the relations (2, 6a, b).

The FEL dispersion equation (the denominator of Eq. (2))

$$D(i\delta k_m, \omega) = 0, \quad (9)$$

is a Pierce-type cubic equation [30]. The zeroes δk_m ($m = 1, 2, 3$) of the cubic dispersion equation (9) are found numerically. The residues of Eqs. (2), (6a), and (6b) are denoted as R_m^E , R_m^n and R_m^v , respectively. The residues of Eq. (2), for instance, are given by

$$R_m^E = \left[\frac{(\delta k - \theta)^2 - \theta_p^2}{i\delta k[(\delta k - \theta)^2 - \theta_p^2] + i\kappa\theta_p^2} \cdot (\delta k - \delta k_m) \right]_{\delta k = \delta k_m} \quad (10)$$

for $m = 1, 2, 3$. In the same manner the residues of Eq. (6a) are $R_m^n = [j\alpha_n(\delta k - \theta)(\delta k - \delta k_m)/D(i\delta k, \omega)]|_{\delta k = \delta k_m}$, and the residues of Eq. (6b) are $R_m^v = [-j\alpha_v(k_z + k_w)(\delta k - \delta k_m)/D(i\delta k, \omega)]|_{\delta k = \delta k_m}$.

With the above definitions, the spectral transfer functions between the FEL output $\tilde{E}_o(\omega)$ and each of the inputs are given by the inverse Laplace transform as

$$T_E(\omega) = \sum_{m=1}^3 R_m^E e^{s_m L_w}, \quad T_n(\omega) = \sum_{m=1}^3 R_m^n e^{s_m L_w}, \quad T_v(\omega) = \sum_{m=1}^3 R_m^v e^{s_m L_w}, \quad (11a, b, c)$$

where $s_m = i\delta k_m + ik_z$ are the poles in the complex s -plane. Fig. 7 shows the amplitude curves of the FEL gain, $T_E(\omega)$, and the prebunched FEL emission, $T_n(\omega)$, for the parameters of our experiment. (The latter curve corresponds also to the FEL spontaneous emission for a uniform spectral density of the electron fluctuations, $|n_i(\omega)|^2 = \text{const.}$).

The output field radiation due to the various sources of excitation is given by the superposition

$$\tilde{E}_o(\omega) = T_E(\omega)\tilde{E}_i(\omega) + T_n(\omega)\tilde{n}_i(\omega) + T_v(\omega)\tilde{v}_i(\omega). \quad (12)$$

and the corresponding output spectral power density is given by $|\tilde{E}_o(\omega)|^2$.

In the time domain, the FEL *impulse response* functions are obtained by performing the inverse Fourier transform of Eqs. (11a, b, c). For instance, the FEL response to a density impulse in the electron beam is given by

$$h_n(\tau) = F^{-1}\{T_n(\omega)\} = \frac{1}{2\pi} \int_{-\infty}^{\infty} T_n(\omega) e^{-i\omega\tau} d\omega. \quad (13)$$

The function $h_n(\tau)$ gives the output field $E_o(\tau)$ due to an impulse electron density $n(\tau) = \delta(\tau)$. Similar integrals define the FEL responses to an input field impulse, $h_E(\tau) = F^{-1}\{T_E(\omega)\}$, and to a velocity impulse, $h_v(\tau) = F^{-1}\{T_v(\omega)\}$. Fig. 8 shows the amplitude of the FEL impulse response function $h_n(\tau)$ for the parameters of our experiment. The output field produced by an electron current impulse at $t = 0$ is a delayed pulse with a finite width.

The impulse response $h_n(\tau)$ can be found analytically in the limit of weak-coupling, low-gain ($\bar{Q} = \kappa\theta_p^2 L_w < 1$), and a tenuous electron beam ($\bar{\theta}_p = \theta_p L_w < \pi$). Though our FEL operates in the intermediate high-gain regime, and we use numerical methods to analyze it, analytical solutions in the low gain limit can provide physical insight.

The dispersion equation (9) has a simple first-order solution in the low-gain limit. The prebunched FEL equation (6a) can be expanded to the first-order in Q , as

$$\tilde{E}_o(i\delta k, \omega) = \{D_0(i\delta k, \omega)^{-1} - D_0(i\delta k, \omega)^{-2} \cdot Q\} \cdot j\alpha_n(\delta k - \theta)\tilde{n}_i, \quad (14)$$

where the zero-order dispersion equation in this limit is $D_0(i\delta k, \omega) = i\delta k(\delta k - \theta)^2$. An inverse Laplace transform is performed analytically by a partial fraction expansion of Eq. (6a) (where the poles of the dispersion equation are $\delta k_1 = 0$ and $\delta k_{2,3} = \theta$). This yields the known spectral relation for the prebunched FEL in the low gain limit

$$T_n(\omega) = \alpha_n L_w \frac{\sin(\bar{\theta}(\omega)/2)}{\bar{\theta}(\omega)/2}. \quad (15)$$

The spectral power density $|T_n(\omega)|^2 = (\alpha_n L_w)^2 \text{sinc}^2(\bar{\theta}(\omega)/2)$ is the spontaneous emission from a uniformly distributed shot-noise ($|\tilde{n}_i(\omega)|^2 = \text{const.}$). The impulse responses $h_n(\tau)$ is found by the inverse Fourier transform (13). In the low-gain limit, it has the simple form,

$$h_n(t) = A e^{-i\omega_0 t} \cdot \begin{cases} 1 & t_g < t < t_e \\ 0 & \text{otherwise,} \end{cases} \quad (16)$$

where the resonance frequency ω_0 is defined by $\bar{\theta}(\omega_0) = 0$, and the amplitude is $A = \alpha_n L_w / (t_e - t_g)$. The response $h_n(\tau)$ from a current impulse at $t = 0$, (in the low-gain limit) has a square pulse envelope which starts at $t_g = L_w/V_g(\omega_0)$ and ends at $t_e = L_w/V_z$, where t_g and t_e are the propagation times through the wiggler [31] of the radiation power and of a single electron, respectively. The impulse response pulse width is simply

$$\tau_s = t_e - t_g = \frac{L_w}{V_z} - \frac{L_w}{V_g} \quad (17)$$

The time constant τ_s , the FEL slippage time, is related to the coherence time and to the line width in the low-gain limit, $\Delta\omega \cong \pi/\tau_s = \omega_0/2N_w$.

The output field for any time-dependent electron beam density at the entrance, $n_i(t)$, can be found from a convolution with the impulse response $h_n(\tau)$

$$E_o(t, z = L_w) = \int_{\tau} n_i(t - \tau) h_n(\tau) d\tau. \quad (18)$$

Similar expressions can be derived which relate the output field to the input field, E_i ; and a velocity perturbation, V_i .

3.2 Linear Model of the FEL Oscillator

The radiation build-up process in a FEL oscillator incorporates processes of spontaneous emission and amplification. The oscillator consists of an FEL section and a cavity or a feedback loop, as shown schematically in Fig. 9. The FEL is modelled here as a block with two inputs, $\tilde{E}_i(\omega)$ and $\tilde{n}_i(\omega)$, and one output, $\tilde{E}_o(\omega)$, with known linear relations between them (given by Eqs. (11a) and (11b), respectively).

The feedback loop, made of a waveguide in a form of a ring cavity geometry, is a lossy dispersive medium. The phase shift during one roundtrip in the cavity is given by

$$\phi_d(\omega) = \sqrt{(\omega/c)^2 - (\pi/a)^2} L_c, \quad (19)$$

where L_c is the cavity length. The waveguide dispersion curve and the FEL tuning line $\bar{\theta}(\omega, k_z, V_z) = 0$ are shown in Fig. 10. The intersection of these curves at the points A and B determine the FEL operating conditions. As the electron energy decays, the slope of the beam mode line decreases, and the intersection points A and B converge

to C. When the beam energy falls too low, no intersection is possible, and when the separation between the beam and waveguide becomes too large, no power is produced.

In our experiment the FEL parameters are slightly time dependent due to the slow variation in the electron beam energy (1). Fig. 11 shows the time dependence of the FEL resonance frequency f_0 , of the corresponding cavity roundtrip time $t_d = L_c/V_g$, and of the slippage time τ_s (17). The results show that in our experimental parameters the slippage time is much shorter than the roundtrip time,

$$\tau_o \ll t_d \ll \tau_m, \quad (21)$$

thus we can apply a two-time-scale approach. The short one is the FEL time scale, $t \sim \tau_s$, and the long one is the cavity time scale, $t \sim t_d$.

In order to find the impulse response of the FEL oscillator, we model it as a cascade of FEL blocks [32] as shown in Fig. 12. Each stage l in the cascade represents one round-trip period which includes an FEL section ($FEL^{(l)}$) and a waveguide section (modeled as a delay element D_l (19)). Each FEL block has two inputs; one for the EM wave E_i , and the other for the electron beam density fluctuations n_i . By allowing each FEL block to have slightly different beam parameters, we can model the slow energy variation on the beam.

In our model of this experiment, the FEL interaction is initiated by a density an input signal in the n_i port, which represents the shot-noise or fluctuations in the electron beam density. This generates radiation emission at the output port E_o , which is then fed back to the input port, E_i , by the feedback loop, and is reamplified in successive roundtrips. The spiky behavior of the electron beam current described in the previous section leads us to model the electron beam density as a shot-noise process, namely

$$n_i(t) = n_0 + n_n \sum_i \delta(t - t_i), \quad (20)$$

where t_i are random points on the time axis distributed with a uniform density. Consequently, $\delta(t - t_i)$ are uncorrelated Poisson impulses. Such a shot-noise model refers usually to fluctuations from single electrons. In our case, however, we apply it to the current spikes, shown in Fig. 5, as macroparticles.

For each FEL block, the linear transfer functions (11a) (11b) define the spectral relation between the output $\tilde{E}_o(\omega)$ and the two independent inputs, $\tilde{E}_i(\omega)$ and $\tilde{n}_i(\omega)$,

respectively, as

$$\tilde{E}_o(\omega)|_{n_i=0} = T_E^{(l)}(\omega) \tilde{E}_i(\omega), \quad \tilde{E}_o(\omega)|_{E_i=0} = T_n^{(l)}(\omega) \tilde{n}_i(\omega), \quad (22a, b)$$

where the transfer functions $T_E^{(l)}(\omega)$ and $T_n^{(l)}(\omega)$ are computed for the instantaneous FEL parameters at the l^{th} roundtrip.

The response of the FEL oscillator to a single density impulse $n_i(t) = n_0 + n_n \delta(t - t_i)$, is given in the frequency domain by

$$\tilde{E}_o^{(l)}(\omega) = T_n^{(0)}(\omega) \cdot D^{(1)}(\omega) \cdot T_E^{(1)}(\omega) \cdot D^{(2)}(\omega) \cdot \dots \cdot T_E^{(l)}. \quad (23)$$

Fig. 13a shows the spectral evolution of the signal in successive roundtrips, as computed from Eq. (23). Fig. 13b shows the corresponding sweep of the center frequency of each micropulse due to the change in the accelerator voltage (1).

In the time domain, the FEL response at $t = t_2$ is given by an inverse Fourier transform of the cascade transfer function (23),

$$h_{osc}(t_2, t_1) = \frac{1}{2\pi} \int_{-\infty}^{\infty} T_n^{(0)}(\omega) \prod_{l=1}^m T_E^{(l)}(\omega) e^{i\omega t_2 - i(m-1)\phi_d(\omega)} d\omega, \quad (24)$$

where $l = 0$ corresponds to $t = t_1$, and $l = m$ is the number of roundtrips at $t = t_2$. The FEL response to a non-impulse electron density fluctuation $n_i(t) = n_0 + n_f(t)$, where $n_f(t)$ is much shorter than a roundtrip time, is given in general by the convolution integral $E_o(t) = \int_{-\infty}^t h_{osc}(t, \tau) n_f(\tau) d\tau$.

We assume density fluctuations $n_i(t) = n_0 + \sum_j n_j \delta(t - t_j)$, with random amplitudes, n_j , and random appearance times, t_j . Thus the output radiation $E_o(t)$ is a linear superposition of impulse responses $h_{osc}(t_2, t_1)$ for the random spikes, $E_o(t_2) = \sum_j n_j h_{osc}(t_2, t_j)$. The output power is then

$$|E_o(t_2)|^2 = \left| \sum_j n_j h_{osc}(t_2, t_j) \right|^2 = \sum_j n_j^2 |h_{osc}(t_2, t_j)|^2. \quad (25)$$

The intensity of the impulse response $|h_{osc}(t_2, t_1)|^2$ with a high-pass filter ($f > 9.6 \text{ GHz}$) is computed for the parameters of the experiment, and plotted as a function of time in Fig. 14. The theoretically calculated intensity shown in Fig. 14 resembles the observed bell-shaped macropulses shown in Figs. 4 and 6a. In the computed FEL

impulse response, the macropulse peak point appears after 507 ns from the current impulse, the period between two micropulses is ~ 33 ns, and the micropulse width is ~ 5 ns. These theoretical results are quite similar to the experimental measurements shown in Fig. 6. The spikes A' and B' (Fig. 6b) appear at $t_{A'} = 82$ ns and $t_{B'} = 317$ ns, respectively. The peak points of macropulses A and B (Fig. 6a) appears at $t_A = 598$ ns and $t_B = 827$ ns, respectively. Hence, the time difference $t_A - t_{A'} = 516$ ns is close to the difference $t_B - t_{B'} = 510$ ns, and to the theoretical result, 507 ns. The observed signals in all our experimental runs are composed of partially overlapping macropulses with random amplitude and random appearance time. The observed macropulses have the same structure as the computed $|h_{osc}(t_2, t_1)|^2$ shown in Fig. 14.

Fig. 15 shows the pulsewidth of each micropulse plotted in Fig. 14a and the pulse width of the a micropulse without the FEL interaction (but with waveguide dispersion) It can be seen that, for these parameters, the tendency of waveguide dispersion to broaden the micropulse is counteracted somewhat by the high gain and phase modification of the FEL.

4 Discussion

In this paper, we have identified a fundamental signal structure, the bell-shaped macropulse of Figs. 4 and 6a, which is the underlying building block of the rf pulse near oscillation threshold. The experimental measurements of the time dependence of the macropulse are in agreement with a theoretical shot-noise analysis of the FEL oscillator.

The agreement between experiment and theory is remarkable, but some underlying assumptions in the theory used to produce Fig. 14 cannot be verified experimentally with our present apparatus. In the experiment we observed a correlation between the macropulses (Fig. 6a) and spikes superposed on the electron beam current (Fig. 6b). In the theoretical analysis, a random sequence of ideal impulses (20) serves as a model for the current spikes (Fig. 5). The observed spikes may have a pulsewidth of the order of 1 ns, which is much longer than a wavelength ($\lambda = 0.1$ ns). We assume however, without an experimental verification, that these random spikes have a non-zero spectral content in the FEL frequency band. The effect of this spectral content, which has an almost uniform spectral density, is modeled here by the impulse response model. A non-uniformity in the spectral content of the spikes in the FEL frequency band causes some widening of the micropulses which can be easily evaluated by a convolution integral as in Eq. (18). The agreement between the experimental and the theoretical results as presented above, confirms our understanding that the radiation macropulse is generated by a current spike. In particular, in the example shown in Figs. 6a,b the spike A' excited the macropulse A, and the spike B' excited the macropulse B. In general, the same macropulse occur in the start-up phase of the FEL oscillator, without the current spikes observed. In the microscopic scale, the shot-noise components of the electron beam excite the same macropulse signals. Thus, we believe, the radiation power in the start-up phase of an FEL oscillator is composed of a large number of such macropulses with uncorrelated random start-up times, as in Eq. (25).

The bell-shaped envelope of the macropulse results from the beam voltage droop. This droop leads eventually to a violation of the FEL resonance conditions, and therefore to a reduction in the micropulses growth rate. In the peak point of the macropulse, the FEL amplification equals to the waveguide attenuation, and the net gain is zero. With a constant electron beam energy, the reamplification of the micropulse would

continue until saturation.

The micropulse bounces in the FEL oscillator, thus it is obvious that the micropulse periodicity equals its roundtrip time in the cavity, as confirmed by experiment and theory. The micropulse is subjected to the waveguide dispersion and to the FEL phase shift, and therefore its width and its amplitude are expected to evolve as a function of time. The first micropulse in Fig. 14 is the instantaneous response of the FEL to the electron beam impulse. Its width is the FEL slippage time, $\tau_s \cong 2.5$ ns. In the following roundtrips it is slowly broadening to 5 ns near the macropulse peak point, in agreement with the experiment (Fig. 6a). This width is narrower than the pulse width which would evolve if the waveguide dispersion would be effective solely, without the FEL (Fig. 15). Hence, we conclude that the FEL net amplification and phase shift counteract the waveguide dispersion and balance the tendency of the micropulse to broaden.

Further experimental investigation of study methods to control the micropulse and macropulse structure suggest themselves. For example, the macropulse could be initiated by an applied current perturbation, the electron beam energy droop can be adjusted to change the number of micropulses, and the dispersion may be adjusted to change the micropulse width. This macropulse formation phenomenon may have practical applications, especially for electrostatic FELs, as a method to produce sequences of tunable high-power short micropulses. A photo-cathode for instance may produce a sequence of short pulses, in addition to a dc electron beam, as in Eq. (2)). In principle, with good control of the electron beam energy, the FEL may produce long macropulses with uniform amplitude.

Appendix: List of symbols

ω	wave frequency
$k = \omega/c$	wave wavenumber in free-space
$Z_0 = \sqrt{\frac{\mu_0}{\epsilon_0}}$	free-space impedance
a, b	waveguide transverse dimensions
$k_z = \sqrt{k^2 - (\pi/a)^2}$	axial wavenumber of the TE ₁₀ waveguide mode
$V_g(\omega)$	group velocity in the waveguide
L_c	length of the ring cavity
$t_d = L_c/V_g$	roundtrip time of a pulse in the cavity
$\omega_0 = 2\pi f_0$	FEL resonance frequency
B_w	wiggler magnetic field
λ_w	wiggler period
L_w	wiggler length
$k_w = 2\pi/\lambda_w$	wiggler wavenumber
B_z	axial magnetic field
e	electron charge
m	electron mass
n_0	average electron density
$\rho_0 = -en_0$	
V_\perp	amplitude of the electron perpendicular velocity component in the com
V_z	electron axial velocity component
$\beta = V/c$	normalized electron velocity
$\beta_z = V_z/c$	
$\gamma = 1/\sqrt{1 - \beta^2}$	the relativistic factor
$\gamma_z = 1/\sqrt{1 - \beta_z^2}$	

References

- [1] C. C. Cutler, "The regenerative pulse generator," *Proc. IRE*, pp. 140-148, Feb. 1955.
- [2] P. W. Smith, "The self pulsing laser oscillator," *IEEE J. Quantum Electron.*, vol. 3, pp. 627-635, 1967.
- [3] P. W. Smith, "Mode locking of lasers," *Proc. IEEE*, vol. 58, pp. 1342-1357, 1970; for recent studies on ultrafast laser phenomena, see the special issue of *IEEE J. Quantum Electron.*, vol. 25, 1989.
- [4] L. F. Mollenauer and R. H. Stollen, "The soliton laser," *Opt. Lett.*, vol. 9, pp. 13-15, 1984.
- [5] R. W. Warren, B. E. Newnam, and J. C. Goldstein, "Raman spectra and the Los Alamos free electron laser," *IEEE J. Quantum Electron.*, vol. 21, pp. 882-888, 1985.
- [6] J. Masud, T. C. Marshall, S. P. Schlesinger, and F. G. Yee, "Gain measurements from start-up and spectrum of a Raman free-electron-laser oscillator," *Phys. Rev. Lett.*, vol. 56, pp. 1567-1570, 1986.
- [7] W. B. Colson, "The trapped particle instability in free electron laser oscillators and amplifiers," *Nucl. Instrum. Methods Phys. Res.*, vol. A250, pp. 168-175, 1986.
- [8] J. C. Goldstein, B. W. Newnam, R. W. Warren, and R. L. Sheffield, "Comparison of the results of theoretical calculations with the Los Alamos free electron laser oscillator experiment," *Nucl. Instrum. Methods Phys. Res.*, vol. A250, pp. 4-11, 1986.
- [9] B. A. Richman, J. M. J. Madey, and E. Szarmes, "First observation of spiking behavior in the time domain in a free electron laser," *Phys. Rev. Lett.*, vol. 63, pp. 1682-1684, 1989.
- [10] J. W. Dodd and T. C. Marshall, "Spiking radiation in the Columbia free electron laser," *Nucl. Instrum. Methods Phys. Res.*, vol. A296, pp. 4-8, 1990.

- [11] Y. Kawamura, K. Toyoda, and M. Kawai, "Observation of periodic short pulse trains in free electron laser oscillations," *Appl. Phys. Lett.*, vol. 51, pp. 795-797, 1987.
- [12] M. N. Rosenbluth, H. V. Wong, and B. N. Moore, "Sideband instabilities in free electron lasers," *Phys. Fluids*, vol. B2, pp. 1635-1653, 1990; See also N. M. Kroll and M. N. Rosenbluth, in *Physics and Quantum Electronics* (Addison-Wesley, Reading, MA, 1980), Vol. 7, p. 147.
- [13] E. Jerby, G. Bekefi, and J. S. Wurtele, "Observations of periodic intensity bursts during the start-up phase of a free-electron laser oscillator," to be published in *Phys. Rev. Lett.*
- [14] H. A. Haus, "Noise in free-electron laser amplifier," *IEEE J. Quantum Electron.*, vol. 17, 1427-1431, 1981.
- [15] P. Sprangle, C. M. Tang, and I. Bernstein, "Evolution of spontaneous and coherent radiation in the free-electron laser oscillator," *Phys. Rev. A*, vol. 28, pp. 2300-2309, 1983.
- [16] K. J. Kim, "Three-dimensional analysis of coherent amplification and self-amplified spontaneous emission in free-electron lasers," *Phys. Rev. Lett.*, vol. 57, pp. 1871-1874, 1986.
- [17] I. Schnitzer and A. Gover, "Prebunched FEL in various operating gain regimes," *Nucl. Instr. and Meth.*, vol. A237, pp. 124-140, 1985.
- [18] J. S. Wurtele, G. Bekefi, R. Chu, and K. Xu, "Prebunching in a collective Raman free-electron laser amplifier," *Phys. Fluids*, vol. B2, pp. 401-406, 1990.
- [19] B. Bonifacio, B. W. J. McNeil, and P. Pierini, "Superradiance in the high-gain free-electron laser," *Phys. Rev. A*, vol. 40, pp. 4467-4475, 1989.
- [20] S. Y. Cai, J. Cao, and A. Bhattacharjee, "Linear theory of superradiance in a free-electron laser," *Phys. Rev. A*, vol. 42, pp. 4120-4126, 1990.
- [21] J. C. Gallardo, L. Elias, G. Datoli, and A. Renieri, "Instability in a multimode free electron laser: effects of electron energy drift," *Phys. Rev. A*, vol. 34, pp. 3088-3100, 1986.

- [22] T. M. Antonsen Jr., B. Levush, "Mode competition and control in free-electron laser oscillator," *Phys. Rev. Lett.*, vol. 62, pp. 1488-1491, 1989.
- [23] D. Oepfs and W. B. Colson, "Phase locking in an infrared short-pulse free-electron laser," *IEEE J. Quantum Electron.*, vol. QE-26, pp. 723-730, 1990.
- [24] J. Fajans, G. Bekefi, Y. Z. Yin, and B. Lax, "Spectral measurements from a tunable, Raman, free-electron laser," *Phys. Rev. Lett.*, vol. 53, pp. 246-249, 1984.
- [25] F. Hartemann, K. Xu, and G. Bekefi, "Generation of short pulses of coherent electromagnetic radiation in free electron laser amplifier," *IEEE J. Quantum Electronics*, vol. QE-24, pp.105-112, 1988.
- [26] K. Xu, G. Bekefi, and C. Leibovitch, "Observations of field profile modifications in Raman free-electron laser amplifier," *Phys. Fluids*, vol. B1, pp. 2066-2072, 1989.
- [27] A. Gover and P. Sprangle, "A unified theory of magnetic bremsstrahlung, electrostatic bremsstrahlung, Compton-Raman scattering, and Cerenkov-Smith-Purcell free-electron lasers," *IEEE J. Quantum Electron.*, vol. QE-17, pp. 1196-1215, 1981.
- [28] E. Jerby and A. Gover, "Investigation of the gain regimes and gain parameters of the free electron laser dispersion equation," *IEEE J. Quantum Electron.*, vol. QE-21, pp. 1041-1058, 1985.
- [29] E. Jerby, "Angular steering of the free-electron laser far-field radiation beam," *Phys. Rev. A*, vol. 41, pp. 3804-3812, 1990.
- [30] J. R. Pierce, *Traveling Wave Tubes*, Princeton, NJ: Van Nostrand, 1950.
- [31] C. Brau, *Free Electron Lasers*, (Academic Press, 1990), Chapter 3.
- [32] A. Gover, H. Freund, V. L. Granatstein, J. S. McAdoo and C. M. Tang, "Basic design considerations for FELs driven by electron beams from RF accelerators," *NRL Rep. 8747*, ; also in *Infrared and millimeter waves*, vol. 11, ch. 8, K. J. Button, Ed., New York: Academic, 1984.

Figure Caption

Fig. 1: The experimental set-up of the FEL oscillator.

Fig. 2: (a) The unfiltered RF bursts, and (b) the Marx accelerator RC voltage droop (on the same time-scale).

Fig. 3: Typical unfiltered RF bursts.

Fig. 4: RF bursts filtered by a band-pass filter, $f = 9.6 - 10.2$ GHz.

Fig. 5: Random spikes in the electron beam current.

Fig. 6: (a) The RF output bursts filtered by a high-pass filter, $f > 9.6$ GHz, and (b) the associated spikes of the electron beam current. Both signals were recorded simultaneously by a fast digital oscilloscope (LeCroy 7200).

Fig. 7: (a) The FEL gain curve $|T_E(f)|$, and (b) the prebunched FEL emission curve $|T_n(f)|$, computed from Eqs. (11a) and (11b), respectively, for our experimental parameters.

Fig. 8: The envelope of the FEL impulse response $h_n(t_2, t_1)$ computed from Eq. (13) for our experimental parameters, $t_1 = 6\mu s$ and $t = t_2 - t_1$.

Fig. 9: A physical model of the FEL oscillator consisting of a time-dependent FEL and a dispersive feedback loop.

Fig. 10: The waveguide dispersion curve $k_z = \sqrt{(\omega/c)^2 - (\pi/a)^2}$, and the FEL synchronism line $\bar{\theta} = (\omega/V_z - k_z - k_w)L_w = 0$. The intersection points A and B determine the

FEL resonance conditions. The slope of the FEL line decays due to the electron energy droop (1). Point C determines the lowest electron velocity for the FEL interaction. The horizontal dashed line shows the filter band above 9.6 GHz.

Fig. 11: The time dependence of (a) the FEL resonance frequency f_0 of point A (Fig. 10), (b) the 7.6 m cavity roundtrip time $t_d = L_c/V_g$ of the instantaneous resonance frequency f_0 , and, (c) the slippage time τ_s (17).

Fig. 12: The 'unfolded' model of the FEL oscillator used for computation of the impulse response.

Fig. 13: (a) The spectral evolution of the FEL oscillator impulse response with a high-pass filter ($f > 9.6$ GHz) in the frequency domain, as computed by Eq. (23) for $t_1 = 6\mu s$. (b) The center frequency at each roundtrip.

Fig. 14: The FEL impulse response intensity $|h_n(t_2, t_1)|^2$ in the time domain as computed from Eq. (24) for our experimental parameters ($t_1 = 6\mu s$).

Fig. 15: The pulsewidth of the computed micropulses in Fig. 14 and their pulsewidth in the same waveguide ring cavity, but without FEL gain ($T_E(\omega) = 0$).

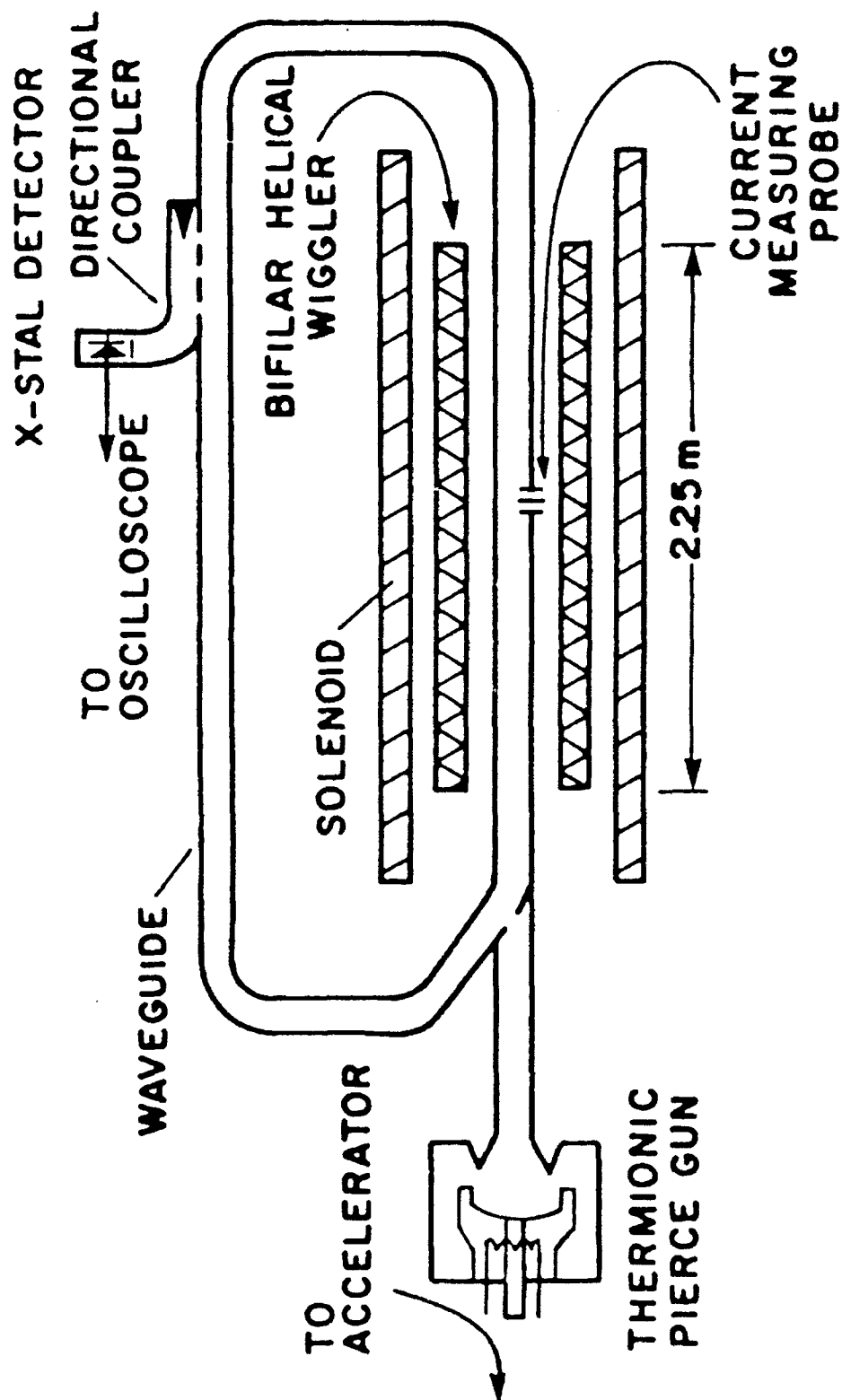
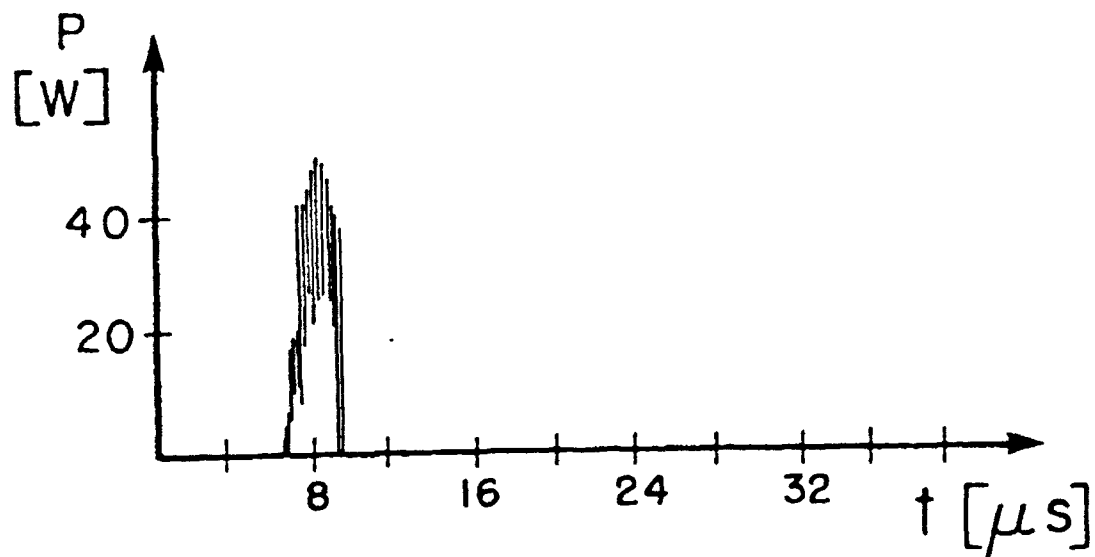
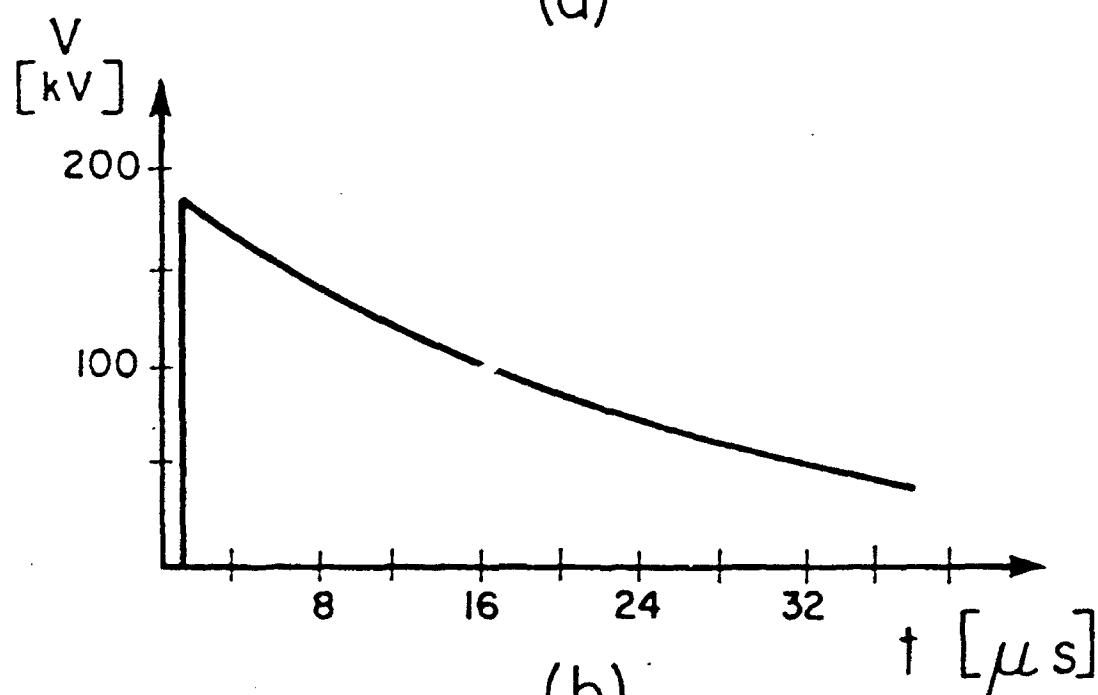


Fig.1 Jerby, bekefi, Wurtele



(a)



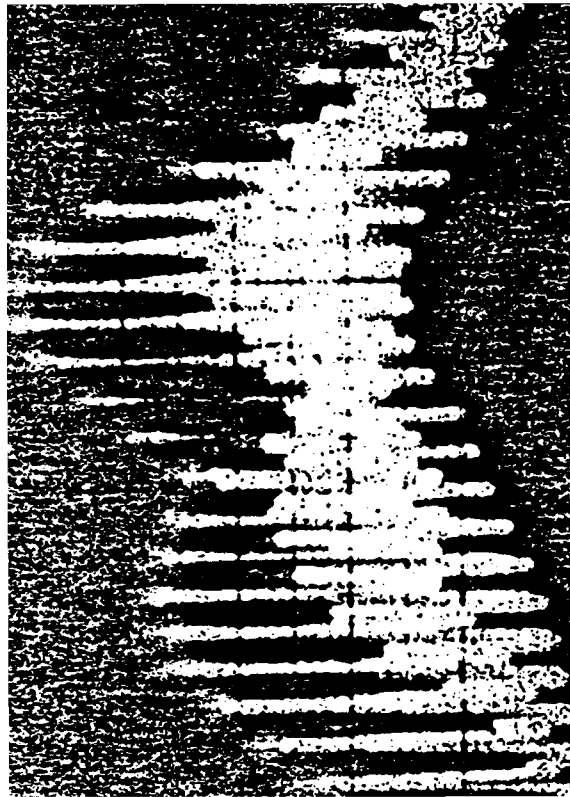
(b)

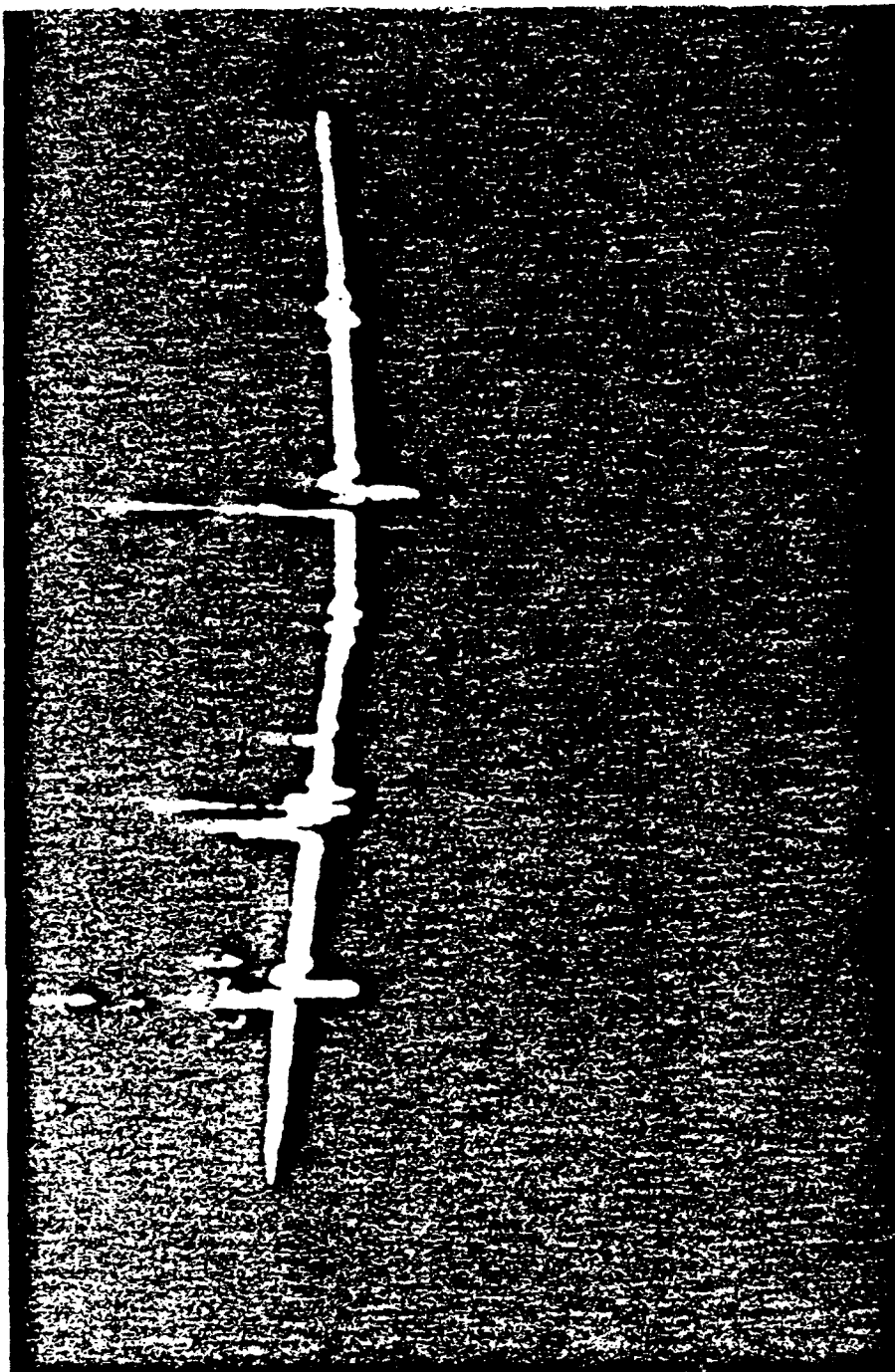
Fig.2 Jerby, Bekefi, Wurtele



intensity

Fig.3 Jerby,Bekefi,Wurtele





current

Fig. 5 Jerby, Bekefi, &

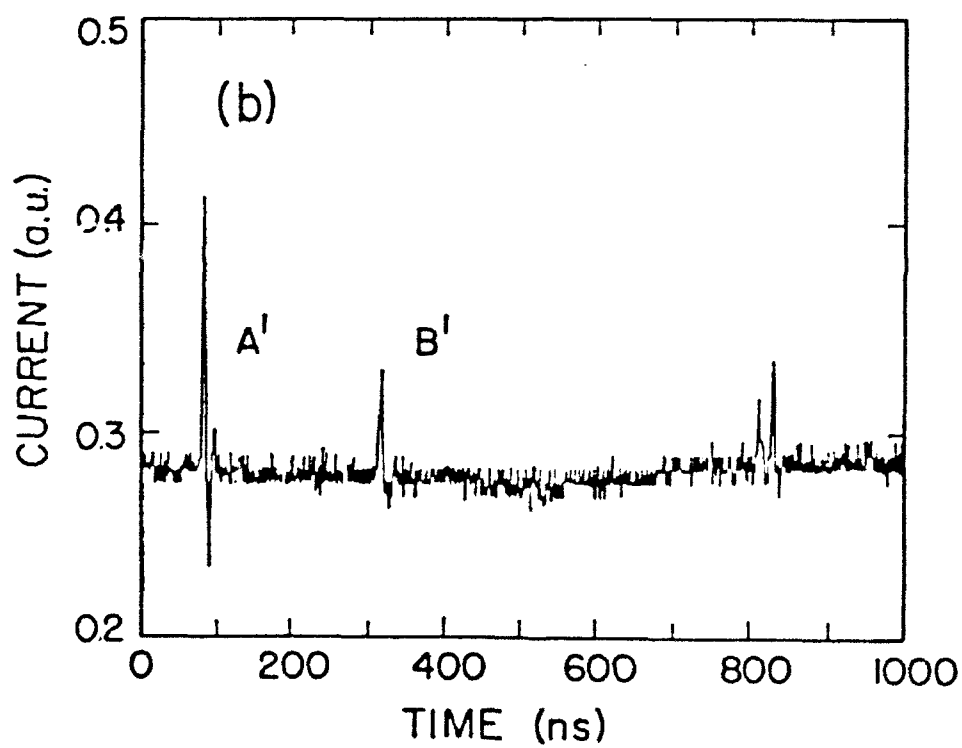
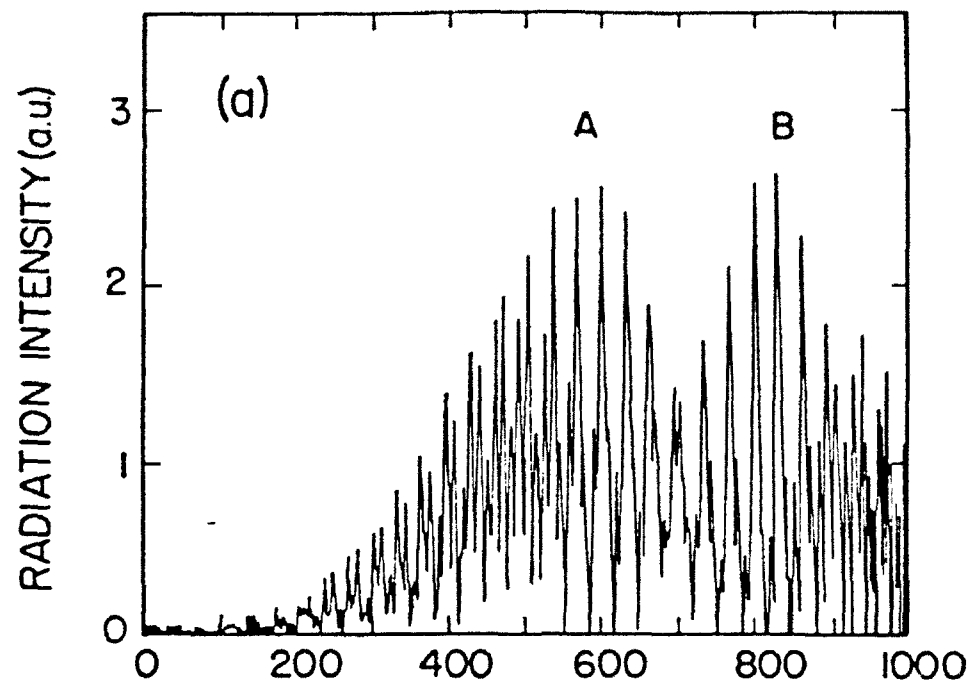


Fig.6 Jerby, Bekefi, Wurtele

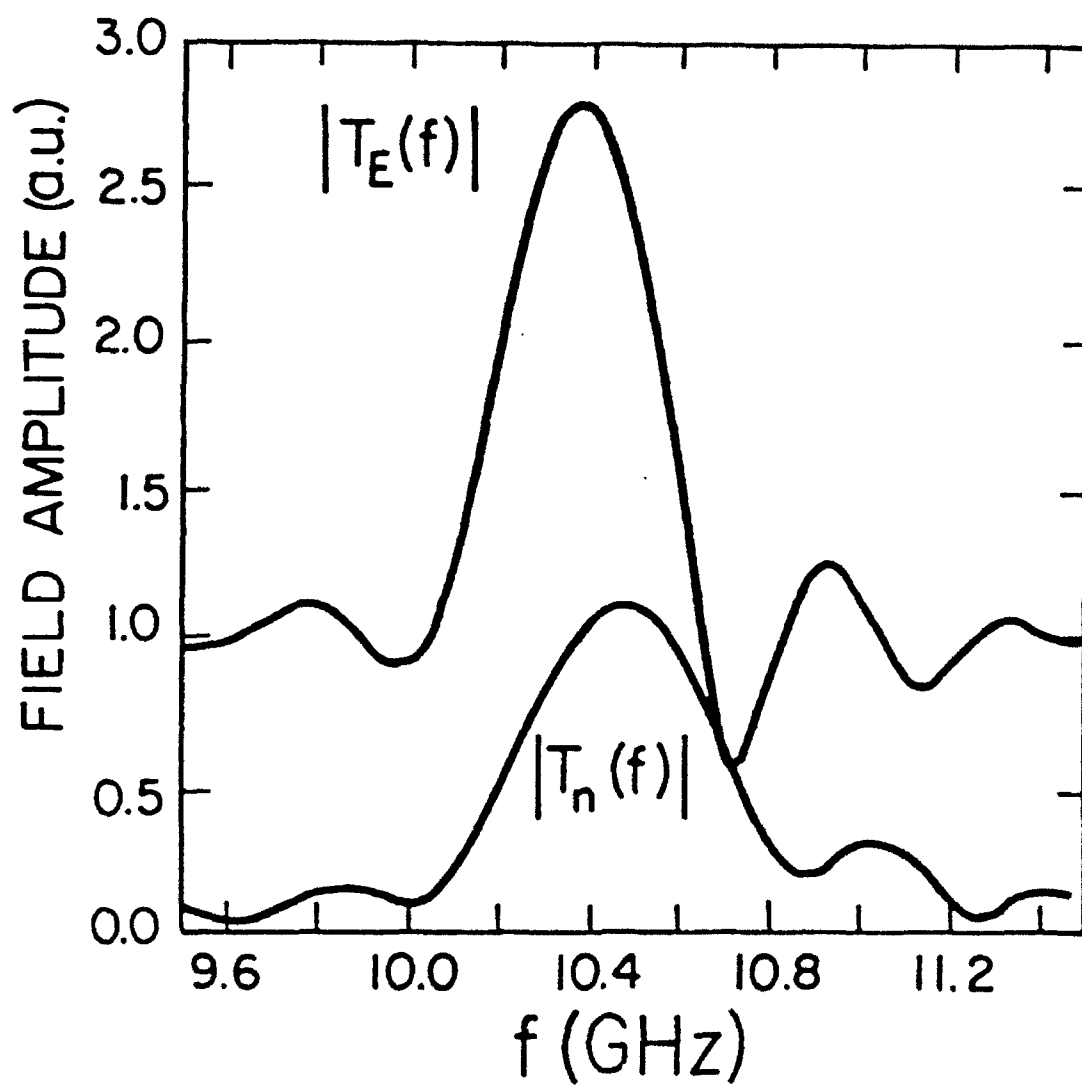


Fig.7 Jerby, Bekefi, Wurtele

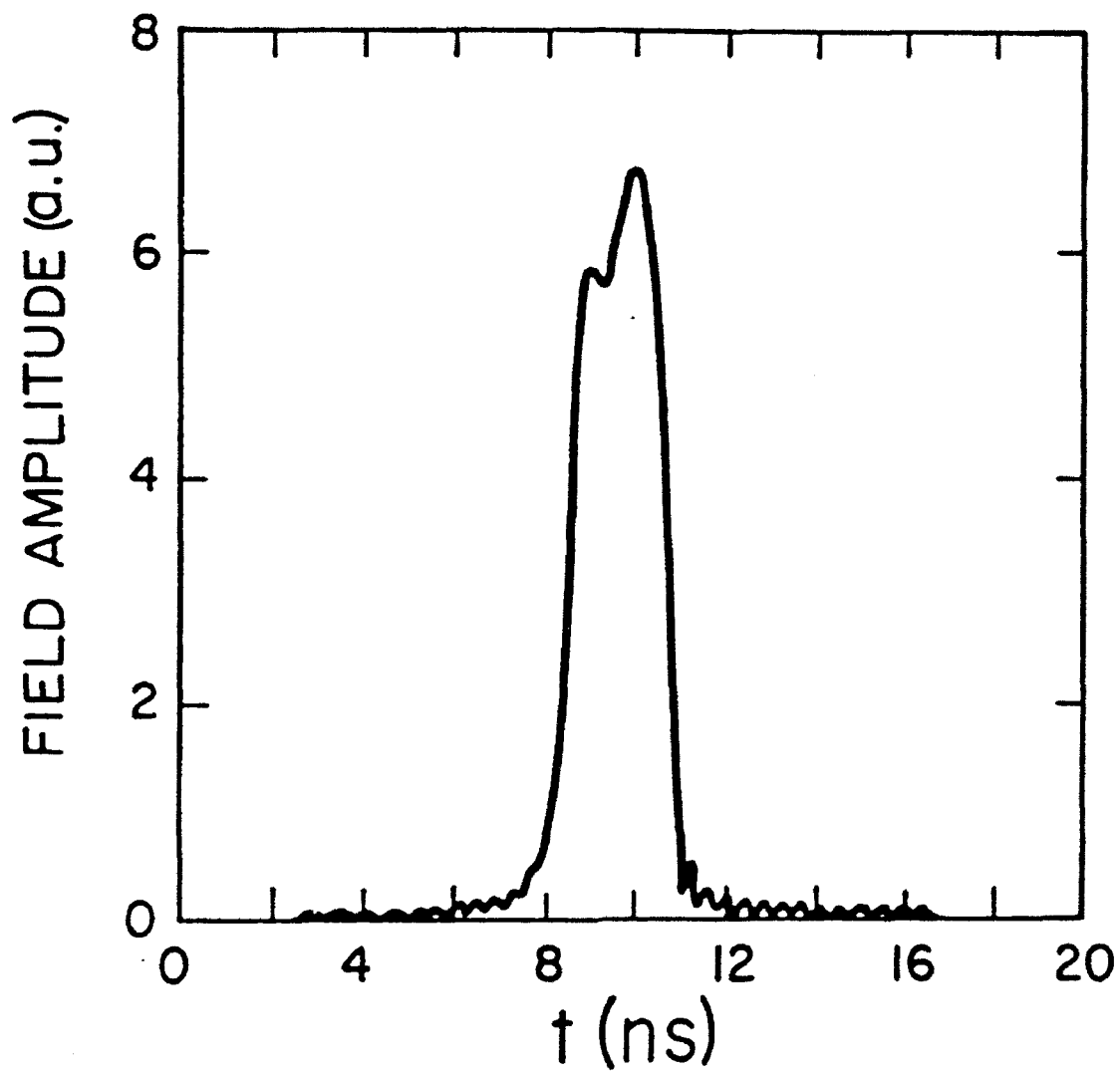


Fig.8 Jerby, Bekefi, Wurtele

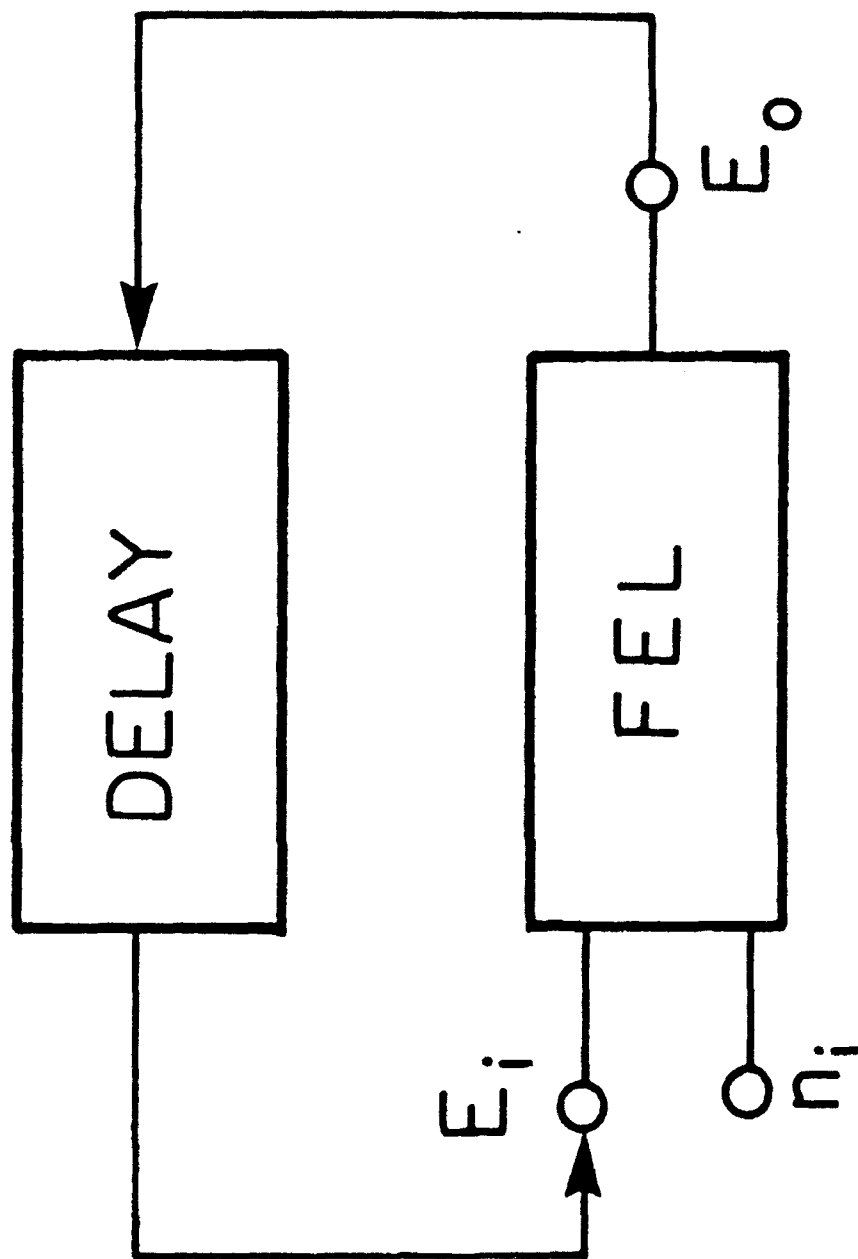


Fig.9 Jerby,Bekefi, γ

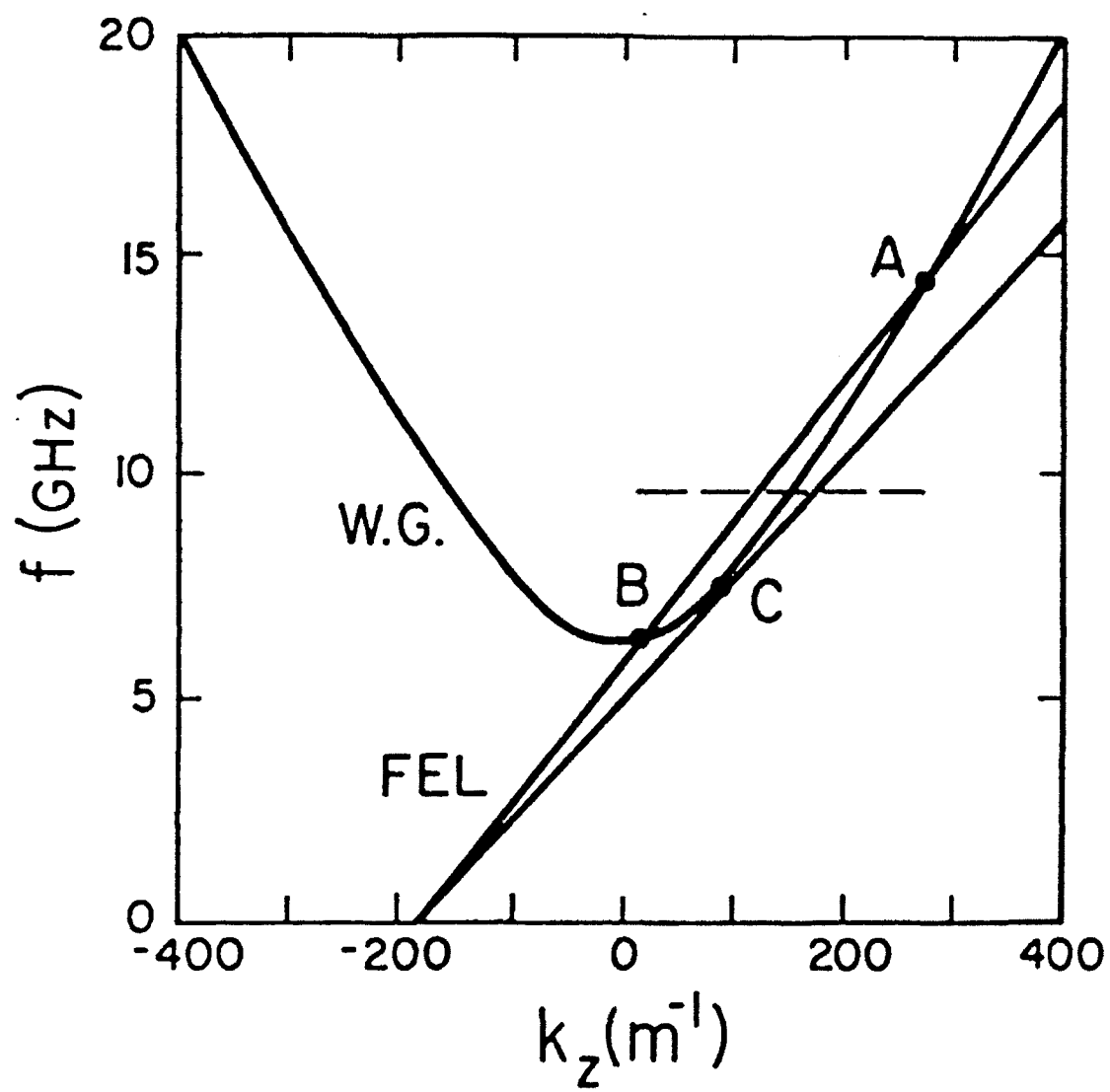


Fig.10 Jerby, Bekefi, Wurtele

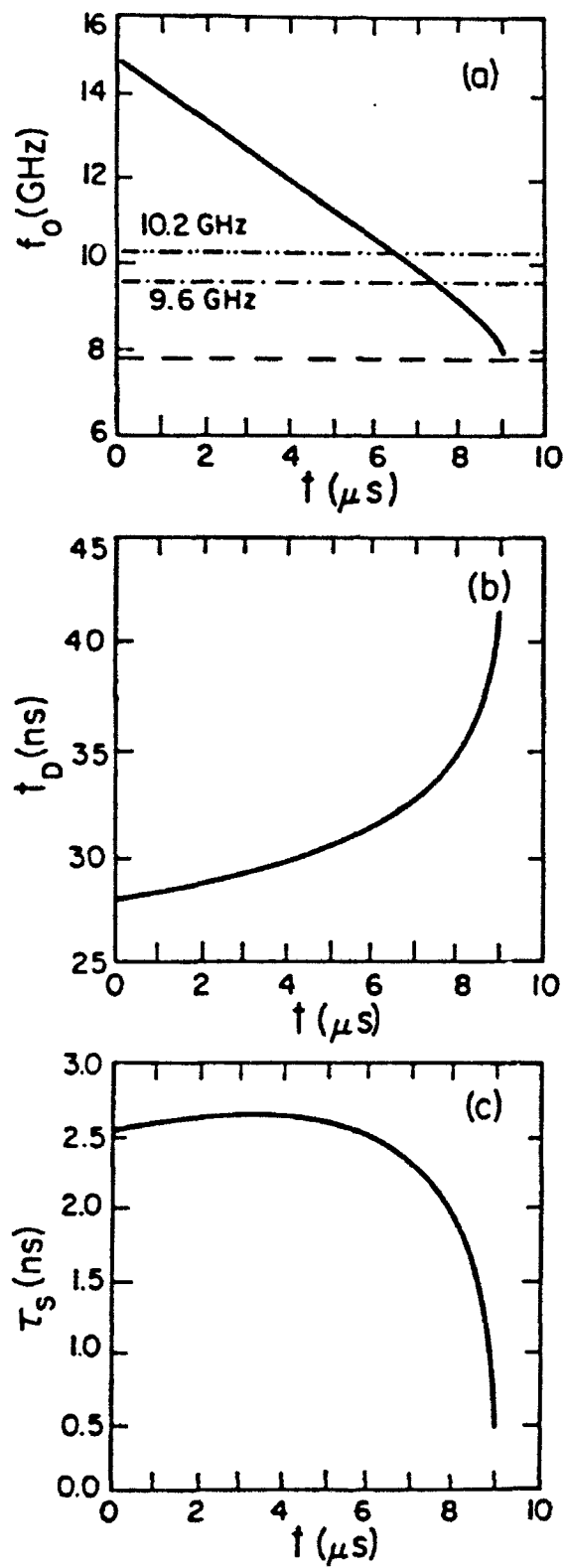


Fig.11 Jerby,Bekefi,Wurtele

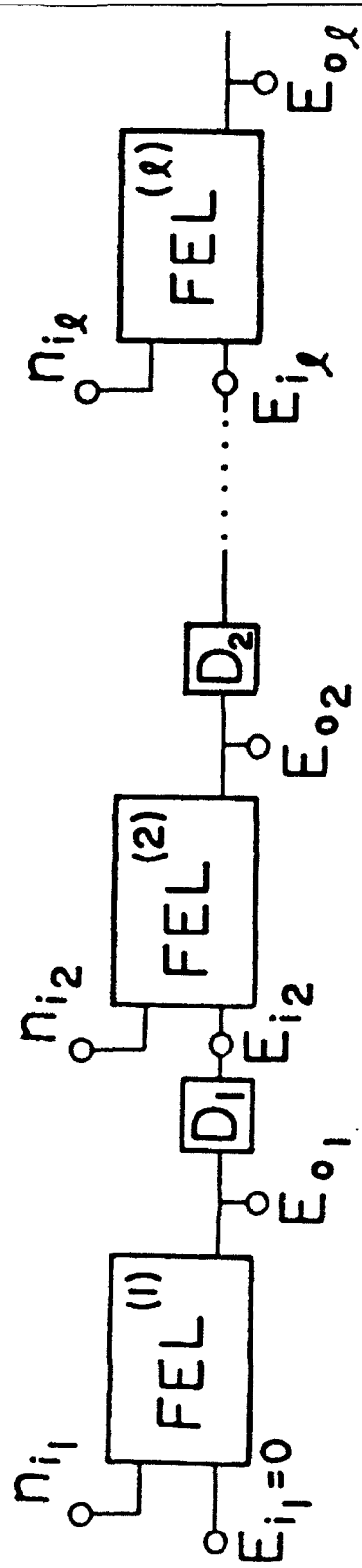


Fig.12 Jerby, Bekefi, Wurt

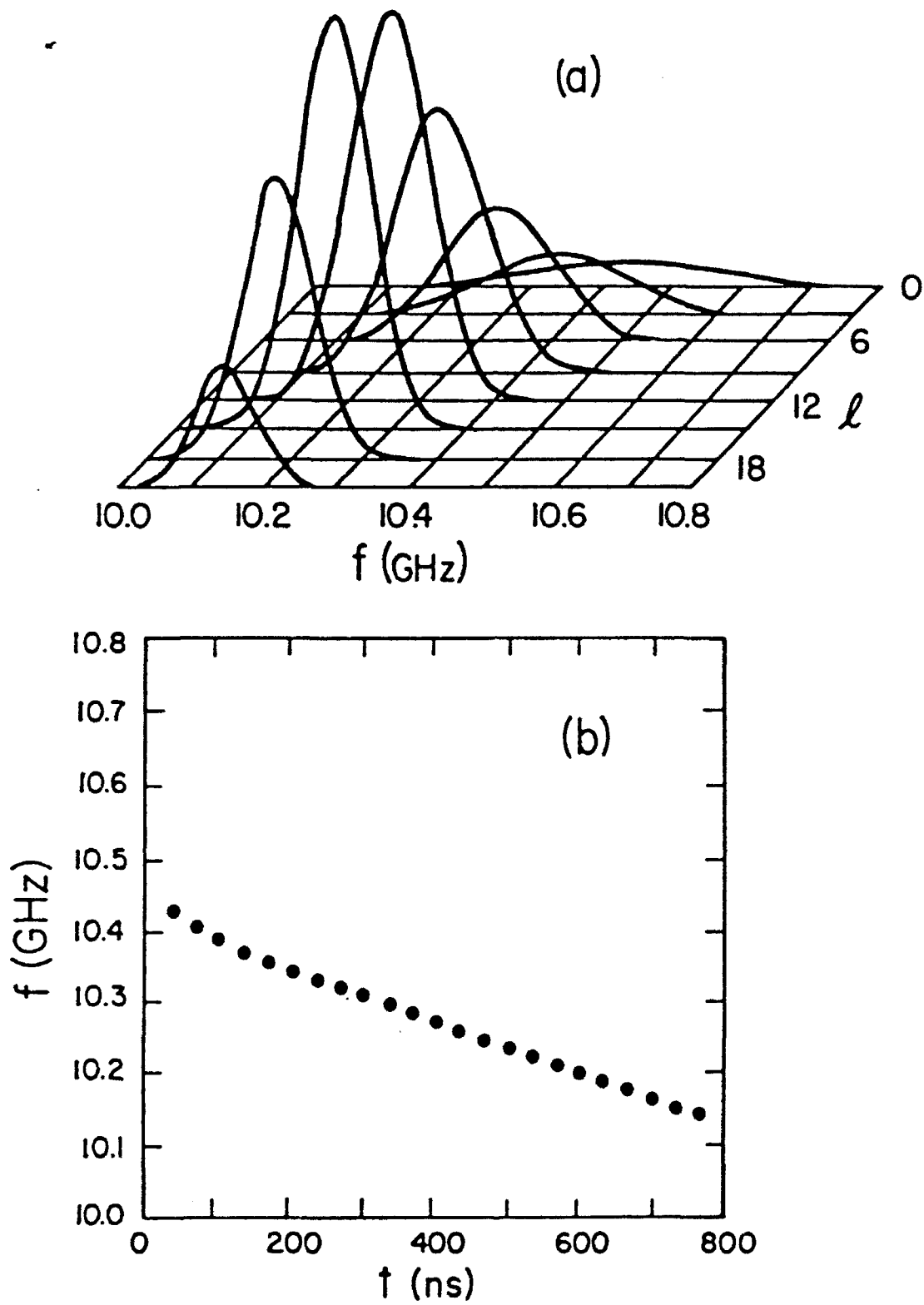


Fig.13 Jerby,Bekefi,Wurtele

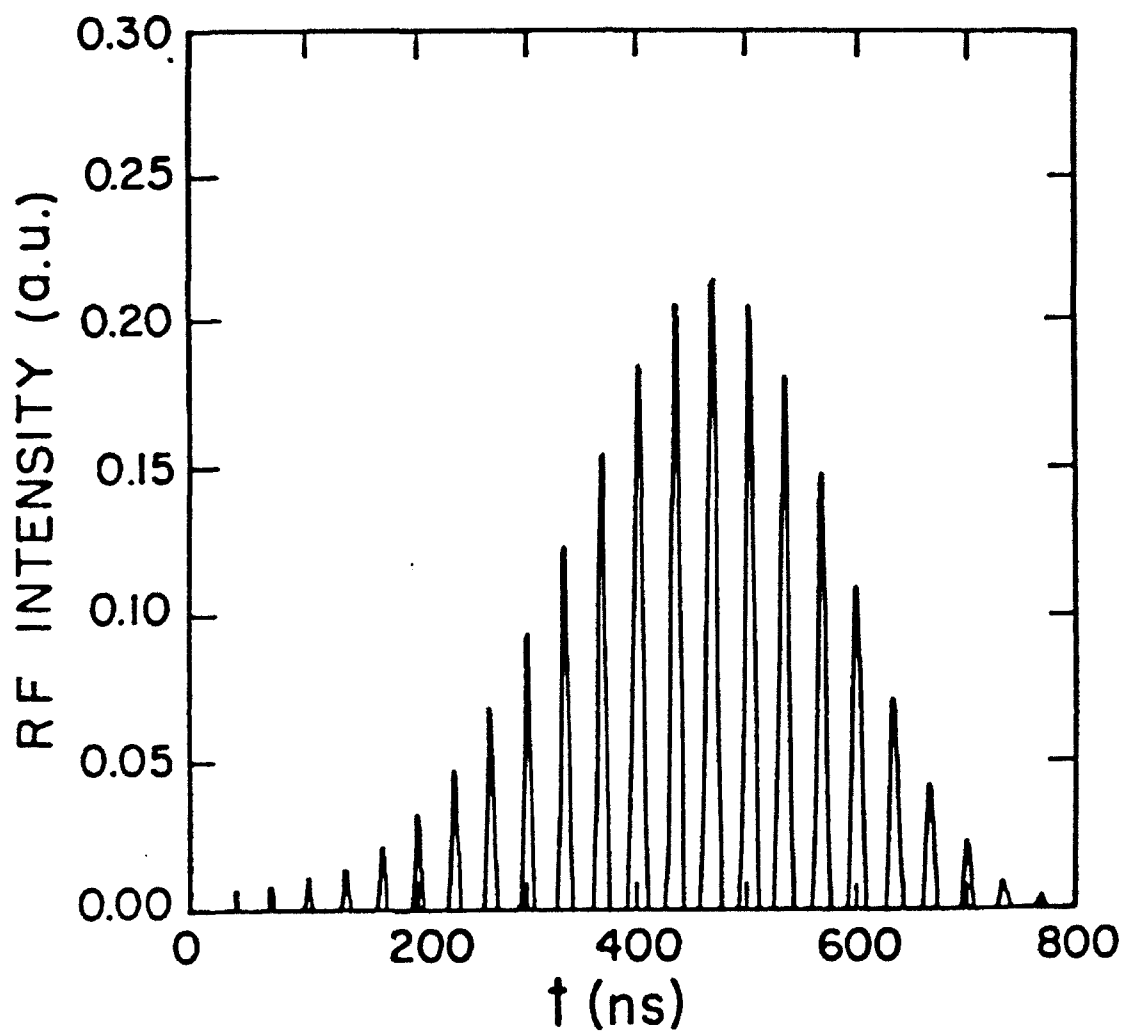


Fig.14 Jerby,Bekefi,Wurtele

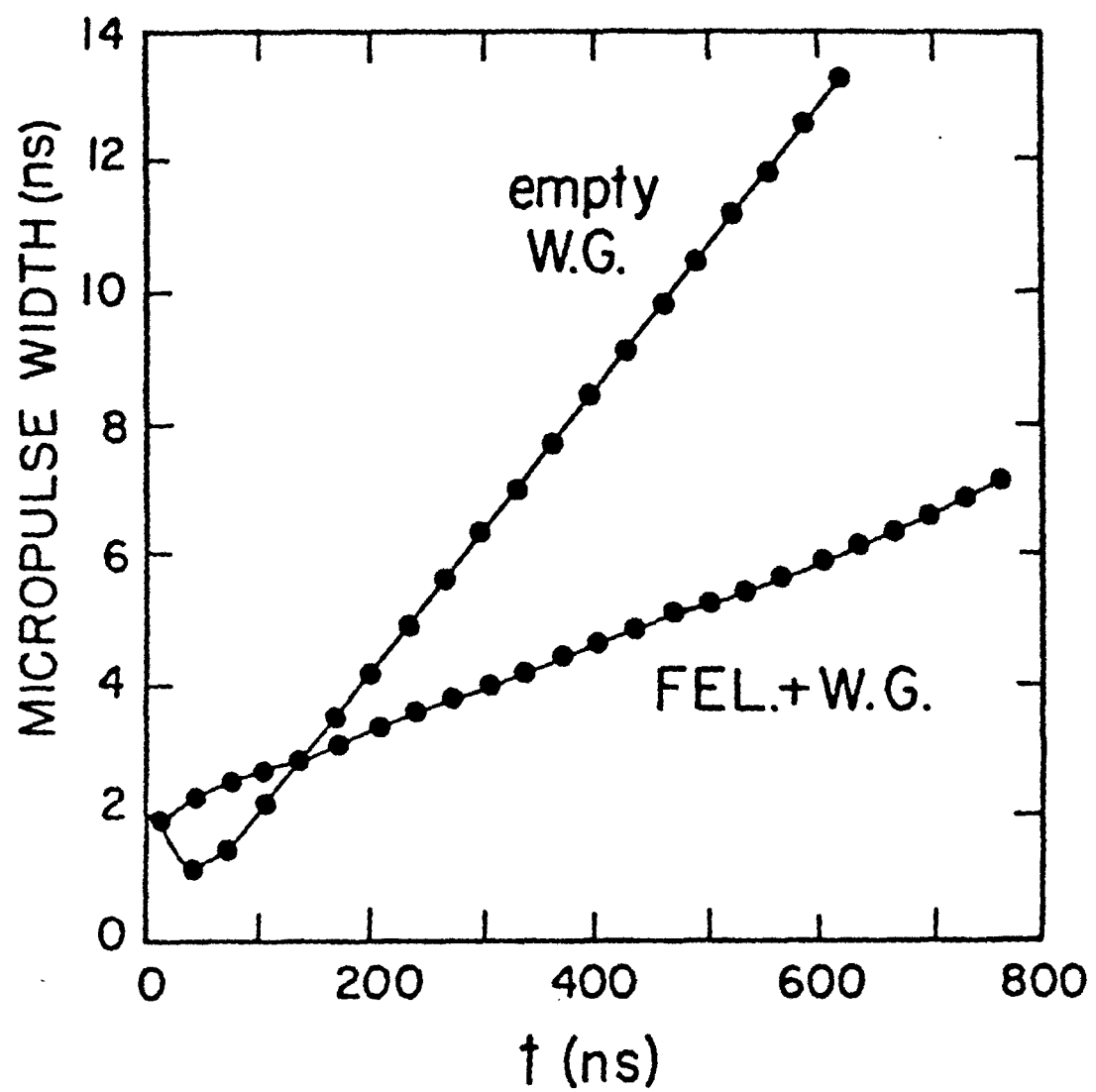


Fig.15 Jerby,Bekefi,Wurtele